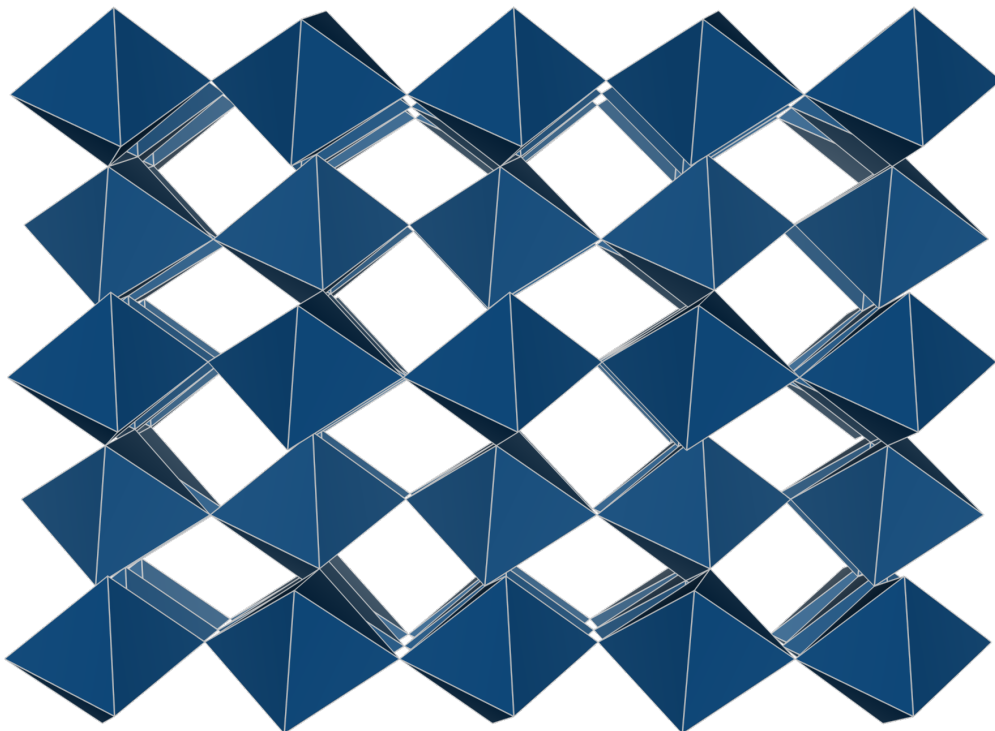


A thesis for the attainment of a Masters degree of Electrical engineering and Applied physics at Computational Chemical Physics group (CCP)

**A computational look at  $LaFeO_3$ ,  $LaCoO_3$  and  $LaNiO_3$ , or**

# **A DFT study of heterostructure-driven charge transfer in transition metal perovskites**



Vits Vidulejs \*

October 18, 2024

Chairperson and daily supervisor: prof.dr. Linn Leppert  
Committee member AP: dr. Christoph Bäumer MSc  
Committee member EE: dr.ir. Cora Salm  
Committee member EE: prof.dr. Peter Bobbert

\* Many thanks to the current and former members of the CCP group, especially Kostas Fykouras, for the help and ideas. And many thanks to Lisa Heymann and Ellen Kiens for fruitful discussions and experimental input.



# Contents

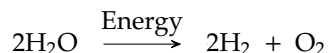
<b>Contents</b>	<b>iii</b>
<b>1 Introduction</b>	<b>1</b>
1.1 Motivation	1
1.2 Perovskites	1
1.3 Catalysts	2
1.3.1 OER	2
1.3.2 TM oxide perovskites as potential OER catalysts	3
1.4 Previous work	4
1.4.1 Superstructure charge transfer hypothesis	4
1.4.2 Experimental work done at UT	6
1.5 The Goals of this work	9
<b>2 Theory and Methods</b>	<b>11</b>
2.1 Theory	11
2.1.1 Schrödinger's problem	11
2.1.2 Hohenberg-Kohn-Sham answer	12
2.1.3 Exchange Correlation Approximation Functionals	15
2.2 Methods	19
2.2.1 Augmented plane waves and basis sets	19
2.2.2 Structure optimization	22
2.2.3 Charge analysis methods	23
<b>3 A reproduction and extension of the work of Zhong and Hansmann</b>	<b>27</b>
3.1 Methods and Reproduction	27
3.2 Critique and Explanation	29
<b>4 A closer look at the materials</b>	<b>33</b>
4.1 Structure and U parameter choice	33
4.1.1 $LaFeO_3$ Structure	34
4.1.2 $LaCoO_3$ Structure	36
4.1.3 $LaNiO_3$ Structure	38
4.2 Valence and Magnetism	40
4.2.1 $LaFeO_3$ Valence and magnetism	40
4.2.2 $LaCoO_3$ Valence and magnetism	42
4.2.3 $LaNiO_3$ Valence and magnetism	46
4.3 Density of states and comparison to PES	48
4.3.1 $LaFeO_3$ DoS and PES	49
4.3.2 $LaCoO_3$ DoS and PES	51
4.3.3 $LaNiO_3$ DoS and PES	55
4.4 Conclusions	57
<b>5 Bulk contact charge transfer investigation</b>	<b>59</b>
5.1 Structure and convergence	59
5.1.1 $LaNiO_3$ - $LaCoO_3$ structure convergence	60
5.1.2 $LaNiO_3$ - $LaFeO_3$ structure convergence	61

5.2	Relaxation and Charge results for the bulk contact structures . . . . .	64
5.2.1	Relaxation results . . . . .	64
5.2.2	Charge results . . . . .	66
5.3	Conclusion . . . . .	70
<b>6</b>	<b>Experimental structure charge transfer investigation</b>	<b>71</b>
6.1	Examining epitaxy on a bulk material . . . . .	71
6.1.1	STO - $SrTiO_3$ . . . . .	72
6.1.2	Impact of epitaxy on $LaNiO_3$ . . . . .	72
6.1.3	Impact of epitaxy on $LaFeO_3$ . . . . .	73
6.1.4	Impact of epitaxy on $LaCoO_3$ . . . . .	73
6.2	Slab convergence and relaxation . . . . .	74
6.2.1	Converging vacuum and slab thickness . . . . .	74
6.2.2	Slabs and relaxation . . . . .	75
6.3	Magnetic and Charge results . . . . .	79
6.3.1	$LaNiO_3$ - $LaCoO_3$ slab results . . . . .	79
6.3.2	$LaNiO_3$ - $LaFeO_3$ slab results . . . . .	83
6.4	Conclusions and orbital occupancy . . . . .	86
<b>7</b>	<b>Conclusions and outlook</b>	<b>87</b>
	<b>APPENDIX</b>	<b>89</b>
<b>A</b>	<b>Computational details and convergence tests.</b>	<b>91</b>
A.1	Chapter 3 . . . . .	91
A.2	Chapter 4 . . . . .	93
A.2.1	Magnetic ordering of $LaNiO_3$ . . . . .	94
A.3	Chapter 5 . . . . .	96
A.3.1	$LaNiO_3$ - $LaCoO_3$ interface vertical relaxation . . . . .	96
A.3.2	$LaNiO_3$ - $LaFeO_3$ interface vertical relaxation . . . . .	97
A.3.3	Magnetic ordering . . . . .	97
A.3.4	HSE06 results for $LaNiO_3$ - $LaCoO_3$ . . . . .	98
A.4	Chapter 6 . . . . .	100
A.4.1	Vertical relaxation of $LaNiO_3$ . . . . .	100
A.4.2	Vertical relaxation of $LaFeO_3$ . . . . .	100
A.4.3	Vertical relaxation of $LaCoO_3$ . . . . .	100
A.4.4	XRD result fitting . . . . .	101
A.4.5	Slab relaxation issues . . . . .	101
<b>B</b>	<b>Work functions and experiments</b>	<b>103</b>
	<b>Bibliography</b>	<b>107</b>



## 1.1 Motivation

Hydrogen is one of the candidates to replace hydrocarbons as a portable energy source, one of the most direct ways to make it is *water splitting*:



This reaction has a known thermodynamic energy cost, but due to reaction kinetics the energy needed is higher in practice. The difference is called *overpotential*, and its linearly related to the cost of producing hydrogen [1]. The reaction itself has two sides to it: hydrogen evolution reaction (*HER*) happening at the cathode and oxygen evolution reaction (*OER*) happening at the anode. In this work we are only considering the anode side - performing the OER reaction, an example of a voltammetry measurement can be seen in fig. 1.1.

There has been previous work done on this subject at the group of Inorganic Material Science (IMS) at this very university, which coupled with a theory paper forms the origin of this work. Within this work transition metal perovskites and their mixed superstructures are purported to improve the overpotential performance of the OER reaction.

## 1.2 Perovskites

The physical material this work is concerned with is the Perovskite. A perovskite is a mineral class named after a Russian mineralogist Lev Perovski, with a general chemical formula  $ABX_3$  with A and B being two cations of two different kinds, and X being a single species of anion.

Here only intrinsic<sup>1</sup> transition metal (TM) oxide perovskites of the form  $ABO_3$  are considered where the B site is a TM. The idealized cubic structure of such a perovskite can be seen as an inset in figure 1.1, A site (Yellow) is in the corners, the B site (Blue) is found in the centre octahedrally coordinated by the Oxygen anions (Red). In real life most perovskites are distorted from this structure as we will see later.

Despite the aforementioned distortion, the TM remains mostly octahedrally coordinated (six nearest neighbours of the same kind). This means that we can use Molecular orbit theory (MOT) and Ligand field theory (LFT) [3] (which is an evolution of crystal field theory [4] for transition metals [5]) to somewhat quickly establish some initial guesses about the electronic structure near the Fermi level.

In the fig. 1.2(b) one can see the one sided MOT diagram near the Fermi level for the prototypical  $ABO_3$  perovskite where the B site is a transition metal. One thing immediately noticeable is that in most cases the unoccupied states of the A ion are far above the rest, so it usually

- 1.1 Motivation . . . . . 1
- 1.2 Perovskites . . . . . 1
- 1.3 Catalysts . . . . . 2
  - 1.3.1 OER . . . . . 2
  - 1.3.2 TM oxide perovskites as potential OER catalysts . . 3
- 1.4 Previous work . . . . . 4
  - 1.4.1 Superstructure charge transfer hypothesis . . . . 4
  - 1.4.2 Experimental work done at UT . . . . . 6
- 1.5 The Goals of this work . . . 9

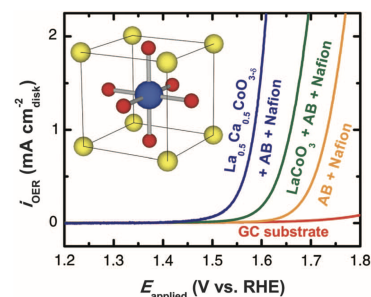


Figure 1.1: An example of a voltammetry measurement from [2], together with an illustration of a standard  $ABO_3$  perovskite.

1: Intrinsic is defined here as a perovskite without doping and only 3 species in the formula

[3]: Griffith et al. (1957), *Ligand-field theory*

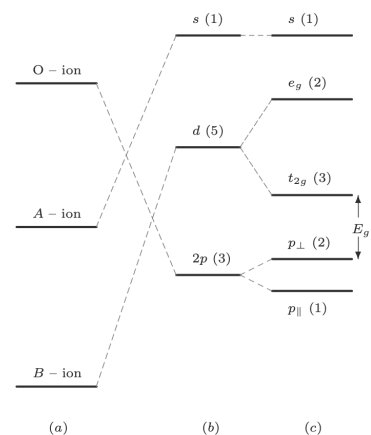
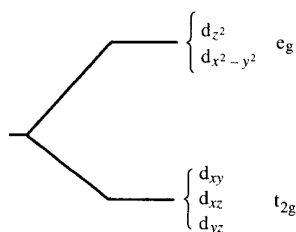


Figure 1.2: A diagram showing the arrangement of the electronic states according to progressive more detailed interaction considerations. a) Charge state b) Madelung potential b) Electrostatic interaction [6]



Differences between d orbital types that are directed straight at ligands and those that are directed between ligands.

**Figure 1.3:** The TM3d orbital arrangement in octahedral coordination showing the orbitals behind the symmetry classes [7].

2: The gap is often called  $10Dq$  for the octahedrally coordinated case, referring to crystal field calculations of the gap. The  $e_g$  states are  $+6Dq$  from  $E_f$  and  $t_{2g}$  are  $-4Dq$  from  $E_f$ . Hence the uneven height split in fig. 1.3

[8]: Cotton (1991), *Chemical applications of group theory*

[7]: Figgis et al. (2000), *Ligand Field Theory and Its Applications*

[9]: Goodenough (1971), *Metallic oxides*

[10]: Man et al. (2011), *Universality in Oxygen Evolution Electrocatalysis on Oxide Surfaces*

does not play an important role in determining the electronic properties. The A site does however influence the p-d valence and conduction bands energies via crystal field interaction. Its size also influences the stability and distortions of the perovskite. Nevertheless the A site can be omitted from the conversation, leaving the B and O sites and their interactions as the main cause of electronics properties of interest, greatly simplifying the conceptual understanding.

As in fig. 1.2 (c), as the states are filled the initial gap is between O2p and TM3d states, and as the 3d states start to fill, the gap is expected to happen between the 3d states only. This assumption holds if we exclude TM3d-O2p mixing and interaction, which is the level of approximation assumed for this work. With this assumption in mind we can further reduce our conceptual efforts by focusing on these states and their interaction.

Now if we zoom in further into the TM d states in image 1.3, one might notice that they are further split. The cause of this splitting is associated with electrostatic and covalent interactions between the TM and its ligands (the coordinating nearest neighbours, so the O site here) <sup>2</sup>. The names  $e_g$  and  $t_{2g}$  refer to the types of symmetries these orbitals belong to; it is by this understanding and the interaction of these symmetries that we can make these level splitting predictions. The details pertaining the process of obtaining the exact predictions of the orbital arrangement in energy are far beyond the scope of this thesis, let alone this chapter and can be found in many books [8] [7].

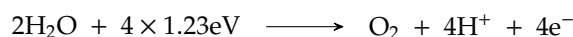
As we move from left to right in the TM part of the periodic table the TM have more electrons in these d states. The distribution of these electrons between these orbitals depends on the electrostatic and covalent interactions between the TM B site and the O site, i.e. low/intermediate/high spin arrangement. And it is this distribution and the level of covalency that largely influences properties such as magnetism, conduction behaviour and many more [9]. So most of the considerations of this thesis are related to these specific states.

## 1.3 Catalysts

As mentioned at the beginning, the goal would be to use these TM-O perovskites as catalysts for the OER part of water splitting. Making any predictions and conclusions on TM-O performance requires some knowledge about the reaction itself, and how the TM-O plays a role in this.

### 1.3.1 OER

The overarching goal as mentioned before is to reduce the over-potential for the OER reaction. We can examine an idealised reaction in acidic media for OER from [10]:



This form shows that there are in essence two reactions transporting four electrons. At the cathode you add 2 electrons per  $H_2$  molecule and you get hydrogen gas, this is the Hydrogen Evolution Reaction (HER), and it has no potential requirements here. At the anode you then subtract these 4 electrons per  $O_2$  molecule thus completing the electrical loop and generating oxygen gas (OER). One has to note that the exact reaction and overpotential requirements at both the anode and cathode differ per medium and pH [11].

Now if one wanted to measure the rate of this reaction you could look at the amount of product gained at each electrode, *or* you could just look at the current passing through. This is exactly what is done in the typical reaction measurement - cyclic voltammetry whose typical measurement result can be seen in fig. 1.1. The ideal catalyst would in this case behave like an ideal diode with its knee voltage being the ideal thermodynamic 1.23V needed for catalysis, with everything over this value called overpotential ( $\eta$ ). The fig. 1.1 also shows measurements of promising catalyst candidates, and the knee voltages are nowhere near the idealised value.

### 1.3.2 TM oxide perovskites as potential OER catalysts

There are volumes written examining TM oxides and TM-O perovskites as possible catalysts for the OER reaction. First unifying work on trying to understand catalysis done by oxides was done by [12], proposing a *volcano plot* based around the enthalpy change of the compound when the TM transitions to a higher oxidation state.

Volcano plots are rooted in the Sabatier's principle which states that there is a *golden mean of catalysis* where the interactions between the catalyst and the reactants is not "too" strong and not "too" weak. These volcano plots in practice display a variable describing the reaction rate on the Y axis and a variable believed to represent catalyst-reactant interaction on the X axis. They are the main tool to assess and predict possible reaction performance.

As one can imagine since then there are many candidate variables proposed for the X axis. The most notable examples compiled by Bockris et al. [13] are:

- ▶ TM-OH bond strength
- ▶ The specific TM d electron occupancy
- ▶ Effective magnetic moment

It has to be said that most of the models presented in that work are still in use to this day as evident by more recent overview papers such as the one by Hong et al. [14]. What is also notable is that these three parameters are not independent from one another as will be shown later and allude to a deeper variable not yet discovered.

For the interests of this thesis the specific TM d orbital occupancy is chosen as our guideline. The specific volcano plot pertaining to this can be seen in fig. 1.4. The volcano plot displays many TM-O compounds, and their TM  $d - e_g$  occupancy, which refers to the two higher energy TM d orbitals as can be seen in figure 1.3.

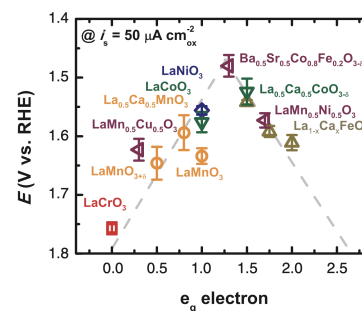


Figure 1.4: A volcano plot from [2]

[13]: Bockris et al. (1984), *The Electrocatalysis of Oxygen Evolution on Perovskites*

These orbitals -  $d_{z^2}$  and  $d_{x^2-y^2}$  can hold 4 electrons at full occupancy, yet the optimum is at 1.25 electrons. This suggests that magnetic behaviour and covalent bonding are intrinsic to a good catalyst for this reaction. Another suggestion made by this plot is that one could add or subtract  $d - e_g$  electrons in a known TM-O such that there is *on average* 1.25  $d - e_g$  electrons left at the TM site to obtain a *seemingly very good catalyst*. This notion will be used to predict if the TM-O super-structures examined in this thesis are better performers at OER than their counterparts.

## 1.4 Previous work

Here the previous work relevant to this thesis is discussed. There is both computational and experimental work done on TM-O perovskites as catalysts, with the practical work being done here at the University of Twente IMS group.

### 1.4.1 Superstructure charge transfer hypothesis

As discussed before one supposed way to influence the activity of a TM-O catalyst is to change the number of d-band electrons. One promising way to influence that is presented in a paper by Zhong and Hansmann [15].

In their work they argue that if you create a heterojunction of certain TM-O perovskites, then charge will move from one perovskite to the other. In their model charge transfer only takes place between the transition metal atoms of the constituent perovskites, thus you would change the charge state of TM atoms on both sides of the junction.

In the paper argues that when two oxide perovskites meet making a interface, they will always share an oxygen on the interface, and thus the electronic DoS pertaining to that oxygen will fixate all other bands in energy, as the oxygen is shared. This can be seen in the visualisation they provide in figure 1.5 (b). The mechanism of charge transfer is somewhat analogous to semiconductors as can be seen in fig. 1.5 (a). Instead of just having the electron affinity (or work function in case of metals), their model relies on a couple more numbers and their relationships. They argue that the filled O2p states below the Fermi level will align thus shifting the rest of the states up or down in energies. The charge transfer takes place between the two half filled TM 3d states which have the Fermi energy somewhere in the middle of them.

[15]: Zhong et al. (2017), *Band Alignment and Charge Transfer in Complex Oxide Interfaces*

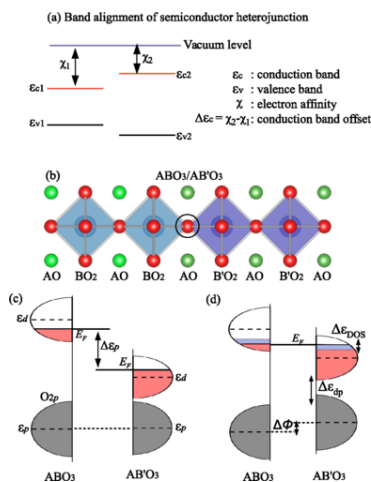


**Figure 1.5:** The visual explanation of the oxygen band alignment driven charge transfer from [15]. (a) shows the classic semiconductor band alignment. (b) Shows the interface between two perovskites and their shared Oxygen. In (c) the proposed band alignment of O2p states is shown. (d) Shows the  $E_f$  equalisation driven charge transfer.

Again referring to Figure 1.5 (c and d), after the alignment of the O2p states the Fermi level will equalize and the charge will flow from the perovskite with the largest O2p-TM distance to the one with a smaller O2p-TM difference. Thus boiling down charge transfer to two numbers - average energy of the first filled O2p state average with respect to the Fermi level, and the average energy of the first (half-filled) TM3d state average with respect to the Fermi level.

Just like with classic semiconductors, this formalism would allow us to simply obtain the DoS of the constituent individual perovskite structures, and simply perform the band alignment based on the first filled O2p band below the Fermi energy, and make predictions based on only this.

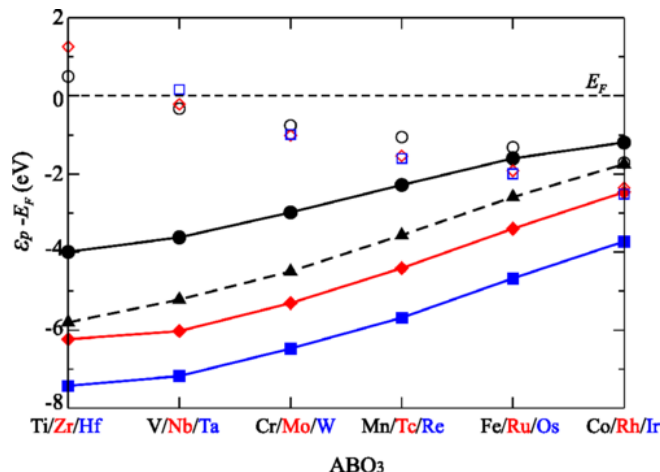


**Figure 1.6:** The simplified result from [15]. Filled symbols are  $e_p$  and empty symbols are  $e_d$ . 3d-black 4d-red 5d-blue for Sr compounds and the dashed line is for La 3d series

It is also noted within the paper that this notion stays intact even adding a buffer layer of a "neutral" perovskite. By neutral the authors mean a perovskite whose 3d energy level is between the two outer most ones, again pointing out to a classic semiconductor heterojunction like behaviour.

Since these two numbers are easily obtainable from simple bulk DFT calculations the authors present the data for select compounds in figure 1.6 taken from [15]. This data encompasses all Strontium compounds ( $Sr + TM + O_3$ ) for three rows of transition metals (3d, 4d and 5d) with depicted with the solid lines, and all Lanthanum compounds with the first (3d) row of transition metals ( $La + 3dTM + O_3$ ) depicted with the dashed line.

Now this goes hand in hand with the simple symmetry based level splitting we argued in the previous section and the purported 3d orbital occupancy relation to catalytic activity. If one looked at fig. 1.2 you could see that the band directly above or at the Fermi level is the TMD band. Ideally we would like to have semiconducting or metallic compounds because then the Fermi level would be located between the TM d states and one would then be able to influence the  $e_g$  electron amount in one of the perovskites by the use of this heterostructure formalism.

This simple scheme predicts that say a heterostructure of  $LaTiO_3$  and  $LaCoO_3$  would force cobalt into a lower oxidation state by the virtue of Ti donating electron(s) to the Co thus adding to its 3d electron occupancy. This would be very useful according to fig. 1.4, as this would most likely push  $LaCoO_3$  to the peak of the Sabatier's volcano.

To add some criticism to this paper I have to note that both  $LaTiO_3$  and  $LaCoO_3$  (Further as LTO and LCO) both are charge transfer insulators in real life [16, 17], which means they have no half filled d shells. Moreover they are also non cubic, unlike in the model presented here, which might have influence on the results, both experimental and theoretical.

This thesis focuses on La compounds so in ways the image 1.6 contains more info than we are interested in, and in other ways too little. Points of interest are the Lanthanum series compounds marked with the dotted line, but the authors chose not to include 4d and 5d metals for this line, moreover they stopped at Cobalt, whereas we are also interested in  $LaNiO_3$ .

[16]: Cwik et al. (2003), *Crystal and magnetic structure of  $LaTiO_3$ : evidence for non-degenerate  $t_{2g}$ -orbitals*

[17]: Rata et al. (2010), *Lattice structure and magnetization of  $LaCoO_3$  thin films*

[18]: Kleibeuker (2012), *Reconstructions at complex oxide interfaces*

[19]: Geessinck (2020), *Charge transfer at the interface between complex oxide thin films*

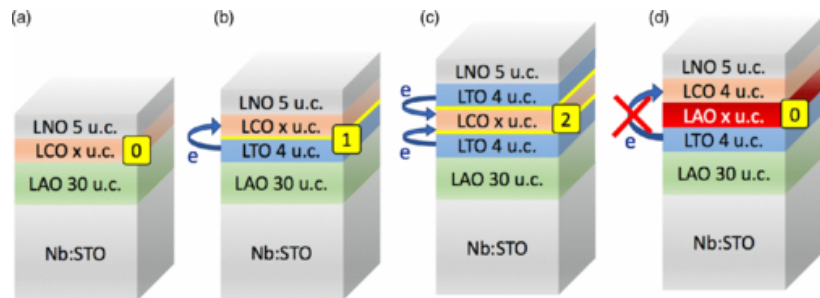
[20]: Arazi-Kanoutas et al. (2020), *Co valence transformation in isopolar  $\text{LaCoO}_3/\text{LaTiO}_3$  perovskite heterostructures via interfacial engineering*

**Figure 1.7:** The family of samples manufactured and tested within the scope of [20]. The number in yellow highlights the number of "active"  $\text{LaTiO}_3/\text{LaCoO}_3$  interfaces, with the last one having a  $\text{LaAlO}_3$  buffer layer which they predict will disable charge transport.

## 1.4.2 Experimental work done at UT

Based on the theoretical prediction experimental work was conceived here at the University of Twente. The first experimental observation of what might be interfacial charge transfer was noted in the PhD thesis of Josep Kleibeuker [18]. It was however Jaap Geessinck's PhD thesis which fully focused on this topic experimentally [19, 20]. In the latter work, Jaap focuses on the  $\text{LaTiO}_3 - \text{LaCoO}_3$  interface, which is predicted to cause electron donation from the Titanium to the Cobalt. Many variations are tested: no interface, one and two interface structures and finally a structure where a blocking buffer layer is inserted. These can be seen in fig.1.7.

In said paper and thesis they report successful generation of interfacial valence transformed divalent cobalt ions. They show that by altering the thickness of the  $\text{LaCoO}_3$  layer and the number of interfaces they can achieve a mix of -tri or -di valent cobalt, with up to 100% divalent cobalt. This change in charge is supposedly realized without a substantial change in structure or chemical doping.



To understand if the claims are true, we have to examine the evidence provided. The evidence they provide is in the form of many measurements. Here I will discuss these measurements as well as the arguments that accompany them.

### XAS - X-Ray absorption spectroscopy

XAS was done at the Co-L<sub>2,3</sub> and Ti-L<sub>2,3</sub> edges using soft X-rays. The figure 1.8 shows a schematic representation of these excitations.

This means that 2p band electrons are excited to the 3d band, according to Fermi's golden rule one then probes the joint densities of state of the 2p and 3d bands. The assumption made here is that the core 2p electrons are static and only provide spectroscopic selection rules, meaning that XAS largely probes the unoccupied 3d band states.

What one obtains is an approximation of the densities of state of the 3d-band. This proves to be very insightful due to the fact that the levels are not degenerate and hybridise differently due to different valence, and bonding environments. This XAS *fingerprint* is unique to a particular atom, its valence state and chemical environment. Meaning that there is a large amount of information to be extracted from such measurements. One general notable trend is that the higher the valence state of an atom is the higher energy edge it produces in XAS.[21, 22]

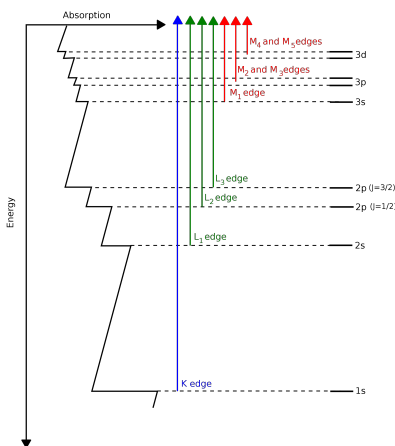


**Figure 1.8:** Transitions that contribute to XAS edges. One would excite the L<sub>2,3</sub> edges to see electrons getting excited to the d band. Thus obtaining information about the chemical environment of the ion.



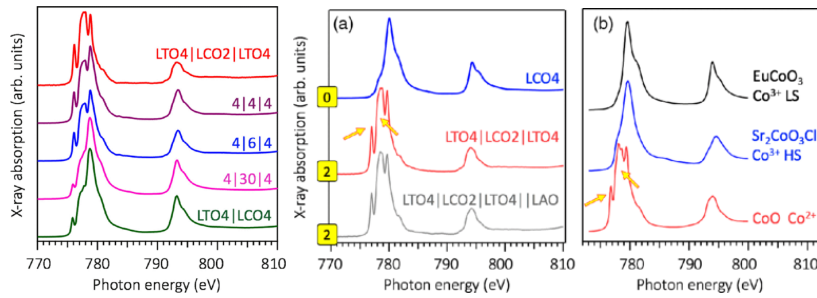


**Figure 1.9:** Here are the Valency fingerprint result from [20]. In the left two pictures the absorption spectra of different samples is shown and on the right the valency fingerprints of Co from known spin state samples is shown. [24]

The results of the various superstructures is shown in figure 1.9. Going from left to right - the first two graphs show the superstructure measurements and the third graph shows reference data obtained from [23]. These are known reference compounds showing both low and high spin variations of trivalent cobalt as well as a sample of divalent Cobalt.

As one can see in figure 1.9, there is no doubt that the valence state of cobalt has been changed, and the first graph on the left shows that valency changes are strongest in two interface systems extending to a "sandwich" of up to 30 UC of LCO.

Here the lowermost interface has been placed 15 nm below the film surface, and thus is essentially invisible in TEY-XAS<sup>3</sup> due to its limited probing depth [25]. This means that this trend of changed Co valency can still be there, it is just not probed.

More interestingly - the practical single interface system in the bottom of the leftmost graph in fig. 1.9 already exhibits 30% divalent Co and a slight shift downwards in energy.

Here the paper clearly mentions that the cause of this change in valency could indeed be the predicted charge transfer from the theory paper, or it could be oxygen non stoichiometry of the  $LaCoO_3$  layer.

This comes as they faced problems during manufacturing with the oxygen partial pressure. In order to grow  $LaTiO_3$  you need a low oxygen background pressure (below  $10^{-4}$  mbar), otherwise you risk growing  $La_2Ti_2O_7$  instead of  $LaTiO_3$ , or will just over oxidate the compound forcing Ti to a 4+ instead of 3+ charge state. On the other hand  $LaCoO_3$  prefers a more oxygen rich environment ( $10^{-2}$  mbar oxygen partial pressure) to avoid oxygen vacancies as shown in [26, 27].

This means that true high oxygen partial pressure growth of  $LaCoO_3$  would aggressively over-oxidise the underlying  $LaTiO_3$  layer. In order to avoid problems they grow both at the same oxygen partial pressure of  $2 \cdot 10^{-3}$  mbar so both layers stabilise. Similarly oxygen diffusion was also quoted in the thesis of Kleibeuker as the source of the valence change. However there is no attempt made at directly examining the stoichiometry of the layers here.

### STEM-Scanning transmission electron microscopy

At the end of the last subsection a question was raised about the layer quality, and possibility of over-oxidation. To answer this STEM (Scanning transmission electron microscopy) measurements were performed by the authors.

3: The authors employed two measurement methods - TEY (Total electron yield) and FY (Fluorescent yield). TEY measurements do not penetrate deep into the surface and FY measurement depth is material dependant due to the Beer-Lambert law.

[26]: Scheiderer et al. (2018), *Tailoring Materials for Mottronics: Excess Oxygen Doping of a Prototypical Mott Insulator*  
 [27]: Meng et al. (2018), *Strain-induced high-temperature perovskite ferromagnetic insulator*

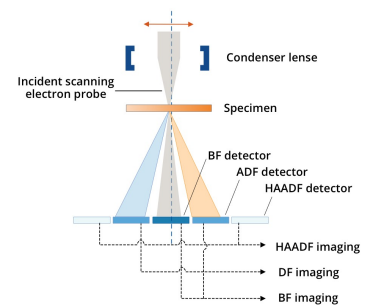


**Figure 1.10:** A schematic representation of the STEM setup. Bf stands for bright field, Df stands for dark field, and HAADF stands for high annular dark field. [28]

4: In terms of electron matter collisions there are backscatters which are the imaging form of SEM. Then there are three types of forward scatters - direct beam electrons (just passing through), elastically scattered electrons and inelastic scattered electrons. The first one is used in normal TEM imaging, the second one is HAADF-STEM and the latter

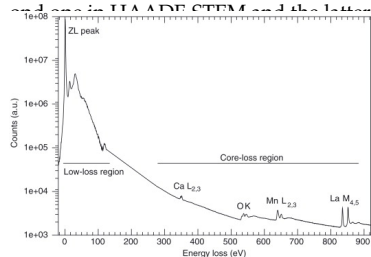
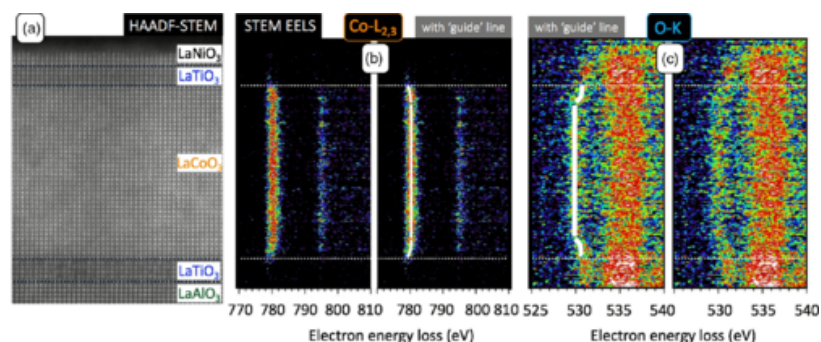


**Figure 1.11:** An example single scan EELS spectrum of  $La_{0.85}Ca_{0.15}MnO_3$  [29]. At set energies one can probe excitation edges similar to XAS. And just like with XAS the higher edge implies a higher valence state. To see these small changes, logarithmic axis is used.

**Figure 1.12:** The STEM results. On the left most image (a) the layer stack is imaged with the HAADF-STEM technique. (b) and (c) On the right hand side you have the core-loss probes of two edges of the structure imaged in (a). These results are rastered along the z axis.



The STEM results can be seen in fig. 1.12. Strain analysis in the thesis shows that the interfaces between  $LaCoO_3$  and  $LaTiO_3$  are under large strain, and in both an expansion of  $LaTiO_3$  out-of-plane lattice parameter is seen in sub figure (a). On the right two images show the STEM-EELS spectra.

In the subfigure (b) the Co specific edge can be seen. In the region near the interface the edge shifts towards lower energies indicating  $Co^{2+}$  presence. While in the rightmost image the O K-edge in subfigure (c) shifts towards higher energies indicating that the Oxygen also experiences change in valence and local chemical environment. This is quite interesting as that implies the Oxygen ions are also part of this transfer.

In the text they do explicitly say that when they do compare peak ratios more electrons are lost by Ti than gained by Co. Implying that there is some involvement of oxygen. But if oxygen migration/ overoxidation would be systematic we would see other structures in HAADF-STEM such as  $La_2Ti_2O_7$  or the Brownmillerite  $LaCoO_{2.5}$ .

In conclusion the experimental evidence show that there is a change in valency of the TM's in these superstructures. However one cannot say with full confidence that the sole responsible for this is the band alignment driven charge transfer.

STEM is a form of Transmission electron microscopy where you rasterize your image via scanning instead of obtaining an image at once with a large collimated beam. A set-up diagram can be seen in fig. 1.10. Two measurement methods of this set-up are used - HAADF-STEM (High-angle annular dark-field imaging) and STEM EELS (electron energy loss spectroscopy).<sup>4</sup>

HAADF-STEM measures at annular detectors as can be seen in 1.10. These detectors avoid the main beam, and in our case use a high angle with respect to the main beam. This allows one to catch Rutherford scattered electrons rather than Bragg scattered (diffraction) electrons. The scattering cross section in this mode is very Z dependant, and therefore the contrast increases quickly with Z (roughly  $Z^2$ ). This allows one to discern individual atomic sites, especially in such a matrix where heavy and light atoms are mixed.

STEM-EELS on the other hand uses the inelastic recoils from the sample. These inelastic recoils happen due to a multitude of reasons among which transitions, and the specific spectra (just as with XAS) is dependant on the local bonding environment and valence state among others. An example of a single location EELS measurement can be seen in fig. 1.11.



## 1.5 The Goals of this work

To summarize - catalytic activity is thought to be influenced by the electronic configuration of the transition metal. This configuration is in turn thought to be changeable by band alignment driven interfacial charge transfer.

The goal of this thesis is to test the *latter* prediction stemming from the work of Zhong and Hansmann. Their prediction is based upon certain assumptions whose validity has not been proven, and the experimental results seem to be inconclusive.

It is here that the goal of this thesis emerges - to test this charge transfer hypothesis and if possible to extend the predictions of the theory paper. This will be done by DFT calculations of the constituent materials and the actual superstructures.

The prediction of Zhong and Hansmann encompasses a large swath of materials. To focus the effort, the materials considered in this thesis are  $LaCoO_3$  and  $LaFeO_3$  epitaxied on  $LaNiO_3$ . Charge transfer is predicted to happen between all three of them, and both  $LaCoO_3$  and  $LaNiO_3$  are close to the optimum  $e_g$  occupancy for OER as per figure 1.4.

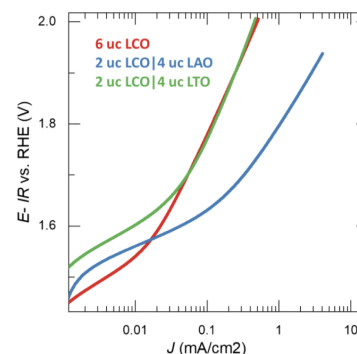


**Figure 1.13:** A preliminary OER measurement found at the very end of the PhD thesis of Jaap [19], indicating that superstructures have a markable influence on the OER activity (Note that the X axis is logarithmic).



As outlined previously we want to know more about the electronic configuration and electronic structure of our material stack, as that has been shown to be a predictor for OER. To do so we need to calculate those properties. To proceed with calculations, I first need to talk about the theory behind the methods and the methods themselves. The methods used pertain to the field of electronic structure theory. So naturally the related theory is quantum in nature. Most of the theory is well known and therefore copied almost verbatim from various books and articles on the topic. These include *Electronic Structure* by Richard M. Martin [30], *A bird's-eye view of density-functional theory* by Klaus Capelle [31], and *Theory and Practice of Density-Functional Theory* by Peter E. Blöchl [32].

## 2.1 Theory

In this section of the chapter I only discuss the theory regarding Density Functional Theory, the practical implementations and considerations are left for the second section titled Methods.

### 2.1.1 Schrödinger's problem

Since an electronic system is quantum mechanical in nature, the logical approach is to use the Schrödinger equation. Let's start by first rewriting the classic equation for our problem of electrons in a solid with atomic nuclei. Before proceeding we will make a simplification - we take upon the Born-Oppenheimer approximation that only the movement of electrons is of interest because the atomic cores are heavy and thus move very slowly in our time-scale of interest, and we will only solve for the electrons in the potential of the atomic nuclei. We are left with the many body Schrödinger equation for  $i$  ( $j$ ) electrons in a solid system with  $K$  ( $L$ ) nuclei:

$$\left[ \sum_i -\frac{\hbar^2}{2m_e} \nabla_i^2 + \sum_{iK} \frac{Z_K e}{|\mathbf{r}_i - \mathbf{R}_K|} + \frac{1}{2} \sum_{i \neq j} \frac{e^2}{|\mathbf{r}_i - \mathbf{r}_j|} + \frac{1}{2} \sum_{K \neq L} \frac{Z_K Z_L e^2}{|\mathbf{R}_K - \mathbf{R}_L|} \right] \Psi(\mathbf{r}_1, \mathbf{r}_2, \dots, \mathbf{r}_N) = E \Psi(\mathbf{r}_1, \mathbf{r}_2, \dots, \mathbf{r}_N) \quad (2.1)$$

Where the general form of the electronic structure Hamiltonian is this:

$$\hat{H} = \hat{T} + \hat{V}_{ext} + \hat{V}_{int} + E_{II} \quad (2.2)$$

The problem consists of four terms: the kinetic energy of the electrons, the electron-nuclei interaction, the electron-electron interaction and the

<b>2.1 Theory</b> . . . . .	<b>11</b>
2.1.1 Schrödinger's problem . . . . .	11
2.1.2 Hohenberg-Kohn-Sham answer . . . . .	12
2.1.3 Exchange Correlation Approximation Functionals . . . . .	15
<b>2.2 Methods</b> . . . . .	<b>19</b>
2.2.1 Augmented plane waves and basis sets . . . . .	19
2.2.2 Structure optimization . . . . .	22
2.2.3 Charge analysis methods . . . . .	23

[30]: Martin (2020), *Electronic Structure: Basic Theory and Practical Methods*

[31]: Capelle (2006), *A bird's-eye view of density-functional theory*

[32]: Blöchl (2011), *Theory and Practice of Density-Functional Theory*

In eq. 2.1:  $\hbar$  is the Planck constant divided by  $2\pi$ ,  $m_e$  is the mass of the electron,  $e$  is the elementary charge, and  $Z$  is the charge of the nuclei.

A system describing *only* electrons would only include terms 1-3, with  $\hat{V}_{ext}$  being left for external potential. It is only by our decision of adding nuclei-nuclei interaction and specifying that the external potential acting on electrons is of Coulomb type from the nuclei, that the Schrödinger equation is one of a solid. It encompasses our application of boundary conditions pertaining to a solid.

1: The wave function is a complex valued number sampled at each grid point so  $2 * 10^3 N = 2 * 10^{30}$  numbers need to be stored now we store it in single precision floats each being 32 bits or 4 bytes yielding  $6.4e+31$  bits of storage needed. Quickly checking that's about  $8.0E+9$  Zettabytes. A study has shown that humanity's storage capacity in 2010 was roughly 290 Exabytes [33], if we say that in 15 years it has quadrupled and we are at one Zettabyte we would still need a billion Earth's to simply store the first guess of the wave-function.

[34]: (1998), *Nobel Prize in Chemistry 1998*

[35]: Hohenberg et al. (1964), *Inhomogeneous Electron Gas*

nuclei-nuclei interaction, and is missing the kinetic energy of the nuclei because of the Born-Oppenheimer approximation.

Once one solves for the wave function then any observable can simply be obtained by applying an operator of choice on the wave function.

There is but one problem. Lets take an example of trying to solve for the wave function of 100 electrons (two tin atoms) in a lattice of 10 grid points in each direction. A quick calculation shows that to initialize the guess wave-function in memory you would need to store roughly  $8.0E+9$  Zettabytes.<sup>1</sup> Similar problems arise with any compute following the memory call. This type of problem is called an "intractable problem" in computational theory. These problems are technically solvable but require a nearly infinite amount of resources (time or computers in this case), and therefore they are considered unsolvable.

### 2.1.2 Hohenberg-Kohn-Sham answer

So if we want to do practical calculations on our perovskites, something better (read cheaper) is needed. The "cheaper" method used in this thesis is Density Functional theory, and its foundations are discussed in this section. This theory has been ground breaking and has revolutionised many fields, so there is no surprise that Walter Kohn got awarded a nobel prize for this work. [34]

#### Hohenberg-Kohn theorem

Previously it was stated that one can obtain any observables from the wave function simply by applying the required operator. One of these observables is particle density:

$$n(\mathbf{r}) = N \int d^3 r_2 \int d^3 r_3 \dots \int d^3 r_N \Psi^*(\mathbf{r}) \Psi(\mathbf{r}) \quad (2.3)$$

So one can logically reason that a ground state wave function will map to a ground state density. As it turns out this idea goes both ways as Hohenberg and Kohn have discovered [35].

The Hohenberg-Kohn theorems tell us that:

**Theorem 2.1.1** *The correlated many body wave-function can be replaced by the particle density, because the entire mapping is injective, thus meaning that the density determines the Hamiltonian and the wave-function, and any observable can be written as a functional of the density.*

**Theorem 2.1.2** *A universal functional for the energy  $E[n]$  in terms of the density  $n(\mathbf{n})$  can be defined, valid for any external potential  $V_{ext}(\mathbf{r})$ . For any particular  $V_{ext}(\mathbf{r})$ , the exact ground-state energy of the system is the global minimum value of this functional, and the density  $n(\mathbf{r})$  that minimizes the functional is the exact ground-state density  $n_0(\mathbf{r})$ .*

An addition to these two there are two corollaries to be had with them:

**Corollary 2.1.3** *The kinetic energy and interaction terms of the Hamiltonian eq. 2.1 are universal functionals of the density, but the  $V_{ext}$  is not and is unique to the system. But the density uniquely determines the external potential to within a constant.*

**Corollary 2.1.4** *The basic theory (there are extensions) is restricted to ground state densities  $n(\mathbf{r})$  with some external potential  $V_{ext}$ , such densities are called "V - representable". This defines the space of possible densities within which we can construct functionals of the density.*

Now we can take the theorems and corollaries, and thus specify a prototypical total energy functional from the terms in equation 2.1:

$$E_{HK} = T[n] + E_{int}[n] + \int d^3r V_{ext}(\mathbf{r})n(\mathbf{r}) + E_{II} \quad (2.4)$$

Here the square brackets denote that its a functional.  $T[n]$  is the kinetic energy term,  $E_{int}[n]$  is the electron electron interaction term, and  $E_{II}$  is the nuclei - nuclei interaction term encompassing the coulomb interaction of the nuclei.

The proof of these theorems can be easily found in the sources and therefore not discussed here.

Now if we want to discuss fermions, an extension to this theory is needed, as they have to abide by the Pauli principle - no two electrons can agree in all quantum numbers. Meaning that upon an exchange of two of the N-electron coordinated the wave functions will change sign. The spin interaction is captured within the  $V_{ext}$  as per usual but to include that explicit interaction the density<sup>2</sup> term has to be rewritten:

$$n(\mathbf{r}) = n(\mathbf{r}, \sigma = \uparrow) + n(\mathbf{r}, \sigma = \downarrow) \quad (2.5)$$

All in all this is a great results, but if we are interested in any observable, we would still need either the ground state density or the fully interacting many body wave function, and that gets us back at square one.

### Kohn-Sham method

To solve the issue of having to deal with the interacting many body wave function, Kohn and Sham in 1965 [36] decided to simply go around the whole problem by using rules previously set in place by the Hoheberg-Kohn theorem. Instead of solving the interacting problem, the proposal is to solve a system which has the same ground state density but the particles are non-interacting single particles, and the interaction is handled trough the "exchange-correlation functional of the density" acting on each of the particles through the added potential we have seen before. Large part of the interaction is handled by Hartree term, with the correlation being much smaller [30].

The Kohn-Sham construction of an auxiliary system rests upon two assumptions:

We can rewrite the first two terms in eq. 2.4 into a universal functional, as they are functionals *only* of the density:  $E_{HK} = F_{HK}[n] + \int d^3r V_{ext}(\mathbf{r})n(\mathbf{r}) + E_{II}$ . This functional  $F_{HK}$  is called the Hohenberg-Kohn functional.

2: Next to the charge density one also has to write a spin density  $s(\mathbf{r}) = n(\mathbf{r}, \sigma = \uparrow) - n(\mathbf{r}, \sigma = \downarrow)$  and also spin polarization density  $\zeta = \frac{s(\mathbf{r})}{n(\mathbf{r})}$  as  $E_{xc}$  functional tend to be expressed in these terms

[36]: Kohn et al. (1965), *Self-Consistent Equations Including Exchange and Correlation Effects*

3: The classic coulomb interaction term is the third term in equation 2.1. This is discreet sum over all electrons whilst excluding self interaction. Now when dealing with densities you are forced to adopt a different expression :  $E_{Hartree}[n] = \frac{1}{2} \int d^3r d^3r' \frac{n(\mathbf{r})n(\mathbf{r}')}{|\mathbf{r}-\mathbf{r}'|}$ . This integral expression allows for the electron to "interact" with itself as you are not excluding the count with itself as before. This leads to what is called "self interaction error".

### Self-consistent Kohn–Sham equations

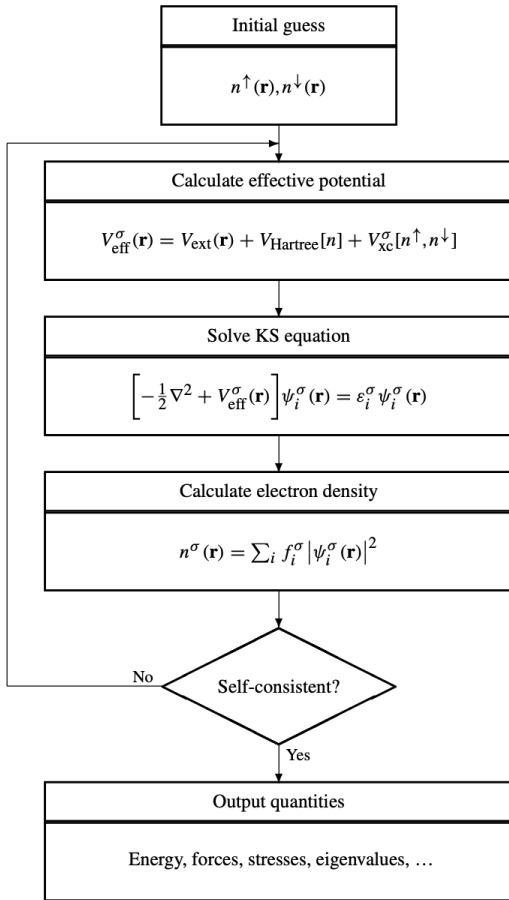


**Figure 2.1:** The Self-consistent Kohn–Sham cycle from Martin [37]. One note here - the electron density here is obtained by the sum of over the states and their occupation numbers  $f_i^\sigma$ . The equations use potentials rather than energies. The potentials (i.e.  $V_{xc}$ ) are obtained as functional derivatives with respect to the density at a point  $\mathbf{r}$ .

**Theorem 2.1.5** The exact ground-state density can be represented by the ground-state density of an auxiliary system of non-interacting particles. This is called “noninteracting- $V$ -representability”; although there are no rigorous proofs for real systems of interest, we will proceed assuming its validity. This leads to the relation of the actual and auxiliary systems shown in Fig. 7.1.

**Theorem 2.1.6** The auxiliary hamiltonian is chosen to have the usual kinetic operator and an effective local potential  $V_{eff}^\sigma(\mathbf{r})$  acting on an electron of spin  $\sigma$  at point  $\mathbf{r}$ . We assume that the external potential  $\hat{V}_{ext}$  is spin independent; nevertheless, except in cases that are spin symmetric, the auxiliary effective potential  $V_{eff}^\sigma(\mathbf{r})$  must depend on spin in order to give the correct density for each spin.

These two statements lead to a rewrite of equation 2.4:

$$E_{KS} = T_s[n(\mathbf{r}, \sigma)] + \int d\mathbf{r} V_{ext}(\mathbf{r})n(\mathbf{r}) + E_{Hartree}[n] + E_{II} + E_{xc}[n] \quad (2.6)$$

Here  $E_{Hartree}[n]$  takes over the coulomb interaction<sup>3</sup>. Here  $V_{ext}$ ,  $E_{Hartree}[n]$  and  $E_{II}$  form a well defined group, and  $T_s[n(\mathbf{r}, \sigma)]$  the single-electron kinetic energy, is in principle also a functional of the spin density.

And all many body effect of exchange-correlation are now grouped within the exchange-correlation energy  $E_{xc}[n]$ .

Now if we compare eq. 2.4 and eq. 2.6 we can rewrite  $E_{xc}$  into:

$$E_{xc} = \hat{T} - T_s[n(\mathbf{r}, \sigma)] + \hat{V}_{int} - E_{Hartree}[n(\mathbf{r}, \sigma)] \quad (2.7)$$

And now it becomes apparent that  $E_{xc}$  is the difference in kinetic and internal interaction energies between the true interacting many body-system and our fictitious independent-particle system.

### Achieving self-consistency

Now to obtain a useful solution of this auxiliary system we must minimise the problem with respect to either the density  $n(\mathbf{r}, \sigma)$ , or the effective potential  $V_{eff}^\sigma(\mathbf{r})$ , as can be seen in fig. 2.1.

Now to do this we have to vary the wave-functions and apply the chain rule to eq. 2.6, giving us a Schrödinger-like equation:

$$(H_{KS}^\sigma - \epsilon_i^\sigma)\psi_i^\sigma(\mathbf{r}) = 0$$

Where  $H_{KS}^\sigma(\mathbf{r}) = -\frac{1}{2}\nabla^2 + V_{KS}^\sigma(\mathbf{r})$

$$\text{With } V_{KS}^\sigma(\mathbf{r}) = V_{ext}(\mathbf{r}) + \frac{\delta E_{Hartree}}{\delta n(\mathbf{r}, \sigma)} + \frac{\delta E_{XC}}{\delta n(\mathbf{r}, \sigma)} \quad (2.8)$$

$$= V_{ext}(\mathbf{r}) + V_{Hartree}(\mathbf{r}) + V_{XC}^\sigma(\mathbf{r})$$

The equations labelled 2.8 are the actual Kohn-Sham equations. The equations are of single particle form and the potential and density must be found self consistently as per figure 2.1. The density is obtained by *summing over the occupied single-particle orbital densities*. Moreover due to the Hohenberg-Kohn the ground state density should uniquely determine the potential at the minimum.

The success of this formalism is that we now have now separated the large *intractable* problem into smaller independent and *tractable* problems where the interaction is handled by this exchange-correlation functional.

### 2.1.3 Exchange Correlation Approximation Functionals

As discussed previously, we now need to define an exchange-correlation functional. Now technically H-K would tell us that for a given system there is a unique functional that is exact, but in reality those do not exist and the available exchange-correlation functionals are all but approximations. To preface this discussion John P. Perdew and Karla Schmidt [38] have coined a term - the "Jacobs Ladder" of density functional approximations i.e. a sort of a ranking of accuracy and computational cost / complexity. I will only compare the functional I will use in ascending order of the Jacobs ladder, or ones that are fundamental and appear very often in the sources, this means that this is in no way an exhaustive or complete comparison.

#### Preface Hartree - Fock

While not an exchange correlation functional in the KS sense, its useful to understand this method to know the pitfalls and strong points of some of the available functionals. Long before the HK and KS theorems, the scientific community already saw the intractability of the problem described by eq. 2.1 and they were looking for solutions.

There were two popular approaches - solving a completely non-interacting electron problem called "Hartree method" [50 from Martin] (Yes the same guy as before)<sup>4</sup>, or one where the electrons only obey the Pauli exclusion principle - the "Hartree-Fock" method. The method is a modification to the former done in 1930 by Vladimir Aleksandrovich Fock. [Ref 53 in Martin]. Here the Antisymmetrization is done explicitly via the Slater Determinant:

$$\Phi = \frac{1}{\sqrt{N!}} \begin{vmatrix} \phi_1(\mathbf{r}_1, \sigma_1) & \phi_1(\mathbf{r}_2, \sigma_2) & \phi_1(\mathbf{r}_3, \sigma_3) & \dots \\ \phi_2(\mathbf{r}_1, \sigma_1) & \phi_2(\mathbf{r}_2, \sigma_2) & \phi_2(\mathbf{r}_3, \sigma_3) & \dots \\ \phi_3(\mathbf{r}_1, \sigma_1) & \phi_3(\mathbf{r}_2, \sigma_2) & \phi_3(\mathbf{r}_3, \sigma_3) & \dots \\ \vdots & \vdots & \vdots & \dots \\ \vdots & \vdots & \vdots & \dots \end{vmatrix} \quad (2.9)$$

This Slater determinant is the correct solution of the SEQ of N non-interacting electrons. It embodies the Pauli principle which is a consequence of the fact that fermions need to have antisymmetric wavefunctions.

Now if we take the Hamiltonian in eq. 2.2 and simplify it using the new wave-function :

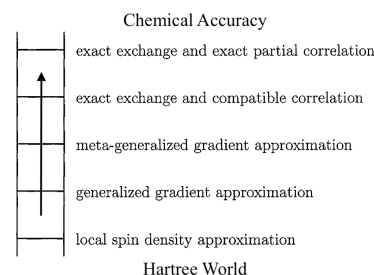


**Figure 2.2:** The "Jacobs Ladder" of density functional approximations, adapted from the publication of John P. Perdew and Karla Schmidt [38]. The accuracy of the computational results is said to increase as you approach the "top".

[38]: Perdew et al. (2001), *Jacob's ladder of density functional approximations for the exchange-correlation energy*

4: The Hartree method involves solving individual electron WF's in individual orbitals, and since each of these is a solution, then by proxy the product of these solutions should at least be an approximation to the many body solution. These electrons interacted with a central potential caused by all other electrons and the nuclei. Self interaction was remedied by subtracting an orbital dependant self-term. Since the development of "Hartree-Fock" the effective Hartree potential has been made orbital independent still with the self interaction problem.

The  $\phi(\mathbf{r}, \sigma)$  are the single particle "spin-orbitals", which have to be independent and are often chosen to be orthonormal for simplicity.  $\Phi$  here is the approximation to the many body wave-function.

$$\begin{aligned}
\langle \Phi | \hat{H} | \Phi \rangle &= \sum_{i,\sigma} \int d\mathbf{r} \psi_i^{\sigma*}(\mathbf{r}) \left[ -\frac{1}{2} \nabla^2 + V_{\text{ext}}(\mathbf{r}) \right] \psi_i^\sigma(\mathbf{r}) + E_{II} \\
&+ \frac{1}{2} \sum_{i,j,\sigma_i,\sigma_j} \int d\mathbf{r} d\mathbf{r}' \psi_i^{\sigma_i*}(\mathbf{r}) \psi_j^{\sigma_j*}(\mathbf{r}') \frac{1}{|\mathbf{r}-\mathbf{r}'|} \psi_i^{\sigma_i}(\mathbf{r}) \psi_j^{\sigma_j}(\mathbf{r}') \\
&- \frac{1}{2} \sum_{i,j,\sigma} \int d\mathbf{r} d\mathbf{r}' \psi_i^{\sigma*}(\mathbf{r}) \psi_j^{\sigma*}(\mathbf{r}') \frac{1}{|\mathbf{r}-\mathbf{r}'|} \psi_j^\sigma(\mathbf{r}) \psi_i^\sigma(\mathbf{r}')
\end{aligned} \tag{2.10}$$

Looking at eq. 2.10, the first line is quite familiar, the second line is the Hartree potential seen before, but the third line is the Fock exchange. The notable feature here is that, while the Hartree term has a self interaction error, this error is cancelled by the same counting error in the Fock exchange. This property is very useful to make the relation nr. 2.7 work. This cancellation will return and feature prominently when discussing Hybrid functionals later.

The HF equations are single-particle equations with no correlation, so there is no long-range screening of the Coulomb interaction by the dielectric constant of the material, and the thermochemical predicting power is bad. Hence they are not used in this thesis.

## LSDA

5: Local Spin Density Approximation and Local Density Approximation respectively

LSDA (which is the spin polarized version [39] of LDA)<sup>5</sup> is one of the simplest exchange correlation approximations. By observing at how the community has gone about constructing it (and its versions), we can learn a bit on how the community approaches understanding, building and using these exchange correlation functionals.

The basic idea behind this approximation is that you treat the electron density as uniform across your space, also known as a Homogeneous Electron Gas.

To begin we rewrite the energy term in an integral with the density, and also separating the exchange part and the correlation part:

$$\begin{aligned}
E_{xc}^{LSDA} [n(\mathbf{r}, \sigma)] &= \int d^3r n(\mathbf{r}) \epsilon_{xc}^{hom} [n(\mathbf{r}, \sigma)] \\
&= \int d^3r n(\mathbf{r}) [\epsilon_x^{hom} [n(\mathbf{r}, \sigma)] + \epsilon_c^{hom} [n(\mathbf{r}, \sigma)]]
\end{aligned} \tag{2.11}$$

6: For LDA its:

$$\epsilon_x^{hom} [n(\mathbf{r}, \sigma)] = -\frac{3}{4} \left( \frac{3}{\pi} \right)^{\frac{1}{3}} n^{\frac{4}{3}}$$

Now luckily the exact solution for the homogeneous electron gas is known exactly, and thus the for the spin polarized version<sup>6</sup> we write:

$$\epsilon_x^{hom} [n(\mathbf{r}, \sigma)] = -6 \left( \frac{3}{4\pi} \right)^{\frac{1}{3}} \frac{1}{n} \left( n^{\frac{4}{3}}(\sigma = \uparrow) + n^{\frac{4}{3}}(\sigma = \downarrow) \right) \tag{2.12}$$

Most of the correlation expressions are functions of  $r_s$  or the local Seitz radius, which is defined as a radius of a sphere containing on average one electron, this depends on the electron density of your system.

This comes from an exact solution from Dirac, its sometimes called Slater exchange, Hartree-Fock-Slater.



Now since HF is still an approximation, there were missing pieces to the puzzle, namely correlation. Correlation is simply the working name for "the rest" which makes the relation 2.7 work.

People have obtained an expressions for correlation of the homogeneous electron gas in many ways. It has been calculated to great accuracy using Monte Carlo methods [40] and there are attempts to obtain it via analytic methods [41]. However the most used ones in practice are the complicated fits and parametrizations of the former <sup>7</sup>. [42, 43]

Surprisingly LSDA works well, yielding lattice parameters a few percent off the experimental ones, and reaction energies not that far off. Besides the obvious issue of uniform electron density, there is another one. Since we are using the Hartree potential and therefore integrating over our electron distribution, our electrons suffer from self interaction error which leads to over de-localisation of our electrons as they over-interact. And most importantly for this project the bandgaps are always underestimated or not there when comparing to experiment. This however is a general problem of KS DFT with local potentials. [44]

### GGA - PBE - Perdew–Burke–Ernzerhof

After LSDA the next logical step would be to include the non-homogeneity of the electron density in our functional. The way it is done is by adding Taylor expansions of the density gradient ( $\nabla n(\mathbf{r}, \sigma)$ ) to the functional. [45] The gradient is added as as a functional in the following way:

$$E_{xc}^{GGA} = \int d^3r n(\mathbf{r}) \epsilon_{xc}^{hom} [n(\mathbf{r}, \sigma)] F_{xc} [n(\mathbf{r}, \sigma), \nabla n(\mathbf{r}, \sigma)] \quad (2.13)$$

Just as before the functional  $F_{xc} = F_x + F_c$  is mostly split into two, where each part is handled separately. For  $F_x$  a gradient dependant *enhancement factor* is added which simply scales the LSDA exchange. Correlation again is handled in evermore complicated ways.

The most known and used one is called PBE [46] with the name being an abbreviation of the authors surnames. In PBE the *enhancement factor* is:

$$F_x^{PBE} = 1 + \kappa - \frac{\kappa}{1 + \mu s / \kappa}, \text{ where } s = \frac{1}{2(3\pi^2)^{1/3}} \frac{|\nabla n(\mathbf{r})|}{n(\mathbf{r})^{4/3}} \quad (2.14)$$

And  $F_c$  in this case gets an added function which depends on  $s$ ,  $r_s$  and the spin polarization  $\zeta$ . As the correlation expression for LSDA was already too complicated to include, it is easy to understand that the one for PBE is even more complicated.

Compared to LSDA, PBE and most other GGA's under-bind molecules (LSDA over-binds), that is to say their SC lattice parameters are larger than experimental[47]. However GGA's do improve the description of structural properties, cohesive energies and magnetism, even when you exclude specialized GGA's. But most of our LSDA woes are still present - there is still the self interaction error. To add to this the problem, band gap reproduction problem is quite fundamental within DFT, <sup>8</sup> and it is not easy to solve.

7: An example that fits the margins is a part of the Perdew-Zunger one, for when  $r_s < 1$ :

$$\epsilon_c^{PZ}(r_s) = -0.0480 + 0.0311 \ln r_s \\ -0.0116 r_s + 0.0020 r_s \ln r_s$$

it is easy to see that these expressions tend to get *jazzy*.

[44]: Perdew et al. (2017), *Understanding band gaps of solids in generalized Kohn–Sham theory*

[46]: Perdew et al. (1996), *Generalized Gradient Approximation Made Simple*

$s$  is the scaled-dimensionless gradient defined in eq. 2.14

[47]: Filippi et al. (1994), *All-electron local-density and generalized-gradient calculations of the structural properties of semi-conductors*

8: The fundamental band gap is defined as the Ionisation potential - Electron affinity:

$$E_{gap} = IP(\mathbf{N}) - EA(\mathbf{N}) \\ \neq \epsilon_{LUMO}(\mathbf{N}) - \epsilon_{HOMO}(\mathbf{N})$$

, which is not the KS band gap. The difference is a derivative discontinuity that none of the local XC-functionals (LSDA, PBE) posses

Initially it would seem logical to only use Fock Exchange but as it turns out that is also not that optimal and the current fractional and range separated mixing methods have their merit. [48]

9: For example : PBE0 [51, 52]

$$E_{xc}^{PBE0} = \frac{1}{4}E_x^{HF} + \frac{3}{4}E_x^{PBE} + E_c^{PBE}$$

[53]: Heyd et al. (2003), *Hybrid functionals based on a screened Coulomb potential*

[54]: Paier et al. (2006), *Screened hybrid density functionals applied to solids*

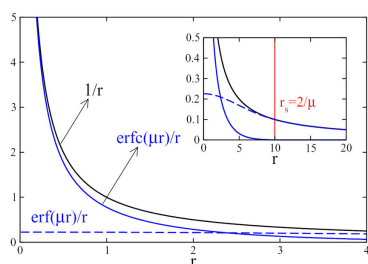


**Figure 2.3:** The HSE06 range-separated kernel compared to the classic Coulomb kernel.[55] The  $\frac{\text{erfc}(\mu r)}{r}$  follows  $\frac{1}{r}$  at the beginning but asymptotically goes to zero. While its long range counterpart  $\frac{\text{erf}(\mu r)}{r}$  starts at a set small value but eventually tends to the  $\frac{1}{r}$  in the long range.

HSE06 has two limiting cases; with  $\mu = 0$  you obtain PBE0 and with  $\mu \rightarrow \infty$  you obtain PBE

[57]: Hubbard (1965), *Electron correlations in narrow energy bands - iv. the atomic representation*

## Hybrid - HSE - Heyd–Scuseria–Ernzerhof

Now we step up the ladder again and arrive at Hybrid functionals. The idea of one is very simple, you mix an Exchange Correlation Approximation (LSDA, GGA or meta-GGA) functional with some exact Fock exchange. [49, 50] The reason for doing this this being the cancelling of the  $E_{Hartree}$  self interaction error. In the HF section it was shown that the double counting in both HF terms leads to cancellation of the self interaction error.

There are two types of implementations; Ones where the mixing is fractional everywhere <sup>9</sup>, and fractional-range-separated as in HSE [53]. In a range separated Hybrid functional the slowly decaying HF exchange is only mixed in the short range and in the long range the XC functional takes over.

Here I am going to discuss HSE06 [54], it mixes the HF exchange with PBE with a range separation parameter  $\mu = 0.2$  :

$$E_{xc}^{HSE} = \frac{1}{4}E_x^{HF,SR}(\mu) + \frac{3}{4}E_x^{PBE,SR}(\mu) + E_x^{PBE,LR}(\mu) + E_c^{PBE} \quad (2.15)$$

The  $\mu$  dependence here comes from a change in the Coulomb kernel:

$$\frac{1}{r} = SR_{\mu}(r) + LR_{\mu}(r) = \frac{\text{erfc}(\mu r)}{r} + \frac{\text{erf}(\mu r)}{r} \quad (2.16)$$

Both of the functions (erfc, erf) are essentially Gaussian softened step functions to reduce numeric problems. Since this is a soft drop off, the switch is very gradual, but the critical point is the screening radius  $r_s = \frac{2}{\mu}$  which is 10 Å for HSE06. At this point the short range part has decayed to zero and the long range part follows the Coulomb kernel  $\frac{1}{r}$ .

The advantages seem clear - Exact exchange for local part of the density and a "cheaper" long range part for faster computation. But again this is still a non-local operator, this means that the KS scheme is minimized with respect to the orbitals and not density. To evaluate the Fock exchange operator one has to work with orbitals instead of densities and perform a complex integral over all of real space. Both of these mean that you suffer a large computational penalty compared to density only functionals.

But at the end of the day the description is improved as minimize the self interaction error, but now we have another problem - in cases where one electron is present the correlation part of the admixture still can overcompensate for the SI correlation. This is largely why the HF exchange is only partially mixed. Moreover by including this exchange we now concede bond energy error [56] in favour of better localisation error, so at best its a trade-off.

## DFT+U - PBE+Dudarev's U

One of the original reasons people developed methods beyond GGA was to correct for the over-de-localisation. And as it turns out there is a *cheaper* way to do it: Hubbard-U [57].

This formalism adds two orbital dependant parameters: J - Local exchange strength and U - Coulomb repulsion. The J parameter enhances the strength of the exchange correlation hole, this favours single spin occupancy and de-localisation. The U parameter on the other hand encompasses the coulomb interaction between electrons and neighbouring atom electrons, it favours full occupancy and localisation. Since these are competing interactions the implementations often only consider an effective  $U_{eff}(= U - J)$  [58].

However there is a fundamental problem of orbital based treatments - there is no unique way to identify local orbitals in an extended system, and the treatments themselves are *somewhat empirical*<sup>10</sup> to put it so, with no real consensus on the right implementation [60].

There are a couple of different implementations of the U parameter, here I will be discussing a simplified rotationally invariant one from Dudarev et al [61] applied on top of PBE:

$$E_{PBE+U} = E_{PBE} + \frac{U_{eff}}{2} \sum_{\sigma} \left[ \left( \sum_{m_1} \hat{n}_{m_1, m_1}^{\sigma} \right) - \left( \sum_{m_1, m_2} \hat{n}_{m_1, m_2}^{\sigma} \hat{n}_{m_2, m_1}^{\sigma} \right) \right] \quad (2.17)$$

Where  $\hat{n}_{m_1, m_2}^{\sigma}$  are the site occupancy matrices of magnetic quantum number  $m$ . The added term goes to zero if matrices are idempotent<sup>11</sup>, which only happens if levels are fully occupied or fully unoccupied, i.e. you introduce a penalty for non integer occupancy.

We know that GGA's over de-localise, so the U is exactly what we need. This helps with the localisation of the complicated Transition metal (TM) oxide open shell electrons [62], as his method quite literally adds a penalty for over-de-localisation. And since you only do a simple projection on top of a KS calculation there is almost no computational penalty. Studies also show that the use of U parameter can lead to a better de-localisation error compared to hybrid functionals [56]. The only caveat is that U parameters are system specific, and there is no one single U parameter for a system that will allow you to correctly describe all the properties of the system, so one must choose wisely and substantiate their choice.

## 2.2 Methods

Here the more practical implementation as found in VASP is going to be detailed, together with my choices when doing computation. The implementation within VASP also dictates the methods I can use and thus also the choices I can make.

### 2.2.1 Augmented plane waves and basis sets

There are some inherent issues with solving the KS equations in a real numeric setting; Near the atoms themselves the kinetic energy of the electrons is very large, resulting in rapid oscillations in the wave function and thus requiring fine grids to capture this, however the large kinetic energy term means that the environment itself has little influence on the

Hartree used to subtract the self interaction per orbital in his method, this is another method where you subtract some orbital dependant energy, so in essence we are back where we started

10: Attempts at grounding the U parameter try to connect it to more complicated theories [59].

[61]: Dudarev et al. (1998), *Electron-energy-loss spectra and the structural stability of nickel oxide: An LSDA+U study*

11: Idempotency mathematically means  $\hat{n}^{\sigma} = \hat{n}^{\sigma} \hat{n}^{\sigma}$  which only happens if the eigenvalues are 1 or 0. If this is the case then the two sums in eq. 2.17 are the same and there is no penalty.

wave function, so you don't need a big basis set, just fine grids. On the other hand, between the atoms in the *bonding region* the kinetic energy is small and the WF is smooth, yet quickly changing and sensitive to the environment. Meaning that a good description here requires a large basis set. Its easy to recognise that they are competing issues, and sating them both is very costly, thus there must come some solution. There are three satisfying solutions available:

1. Basis functions that resemble atomic orbitals. The atomic region only needs a few, and bonding is described by the overlapping tails of these functions.
2. Pseudopotentials, which regard an atom as a perturbation of the free electron gas. For this problem the natural basis functions are plane waves. Plane wave basis sets are complete and good for smooth wave functions. Their problem arises with their simplicity, where you need an exceedingly large amount of them to describe fluctuations of the WF near he nucleus. Moreover all the information on the charge density and WF near the core is lost.
3. Augmented-wave methods which could be considered as a combination of the former. One uses atom-like wavefunctions near the nuclei and a specific set of functions - *envelope functions* for the bonding in between. Thus the space is divided into atom centred spheres separating the *atomic regions* and the *interstitial region*. The partial solutions are matched by equating their derivatives at the the boundary of the spheres.

It is useful to highlight why Plane waves are a logical choice when dealing with solids. Solids exhibit a periodic nuclei structure whose periodicity (and symmetry) in 3D space is characterised by its Bravais lattice. It is by this fact that electrons within a solid experience a periodic potential landscape, with the relationship between the electronic eigenstates and this periodicity being the subject of Bloch's theorem which states:

**Theorem 2.2.1** *The eigenstates  $\psi$  of the one-electron Hamiltonian in periodic potential  $U(\mathbf{r} + \mathbf{R}) = U(\mathbf{r})$  for all  $\mathbf{R}$  of the Bravais lattice, can be chosen to have the form of a plane wave times a function with the periodicity of the Bravais lattice:*

$$\psi_{n\mathbf{k}}(\mathbf{r}) = e^{i\mathbf{k}\cdot\mathbf{r}}u_{n\mathbf{k}}(\mathbf{r}), \quad (2.18)$$

where

$$u_{n\mathbf{k}}(\mathbf{r} + \mathbf{R}) = u_{n\mathbf{k}}(\mathbf{r}) \quad (2.19)$$

for all  $\mathbf{R}$  in the Bravais lattice.<sup>12</sup>

Combining the two relations in the Theorem gives:

$$\psi_{n\mathbf{k}}(\mathbf{r} + \mathbf{R}) = e^{i\mathbf{k}\cdot\mathbf{R}}\psi_{n\mathbf{k}}(\mathbf{r}) \quad (2.20)$$

From which the alternate formulation follows - The eigenstates of the Hamiltonian can be chosen so that associated with each  $\psi$  is a wave vector  $\mathbf{k}$  such that eq. 2.20 is fulfilled for every  $\mathbf{R}$  in the Bravais lattice.

<sup>13</sup>

Thus one can see that plane waves and their associated wave vectors naturally describe problems of motion in periodic potentials.

12: The index n is known as the band index, as for a given  $\mathbf{k}$  there are many independent eigenstates.

13:  $\mathbf{R}$  is a general Bravais lattice vector given by  $\mathbf{R} = n_1\mathbf{a}_1 + n_2\mathbf{a}_2 + n_3\mathbf{a}_3$  and  $\mathbf{k}$  is the corresponding reciprocal space vector  $\mathbf{k} = x_1\mathbf{b}_1 + x_2\mathbf{b}_2 + x_3\mathbf{b}_3$  such that  $\mathbf{b}_i \cdot \mathbf{a}_j = 2\pi\delta_{ij}$

Thankfully there has been a lot of work done on this complicated subject of basis sets, and the most frequently used implementation for solids is the Projector augmented-wave formalism. Projector augmented-waves (PAW) as introduced by Peter E. Blöchl [63], is an energy and potential independent version of the Augmented-wave method. It must be noted that the implementation within VASP by Kresse and Joubert [64] is slightly different than the original version by Blöchl. We still feature augmentation spheres. Meaning the problem is still subdivided into two by the radii  $r_{c,R}$  centered around the atomic site at  $\vec{R}_R$ . These radii are sometimes chosen to be the ionic radii, but within VASP they are also often chosen to be half the nearest neighbour distance. The inside and outside of these spheres are handled differently, with the derivatives at the edge matched.

The main idea of this method is to map the physical one-particle WF's  $|\psi_n\rangle$  to some auxiliary  $|\tilde{\psi}_n\rangle$  which is smooth and numerically convenient using a transformation operator:

$$|\psi_n\rangle = \hat{\mathcal{T}} |\tilde{\psi}_n\rangle \quad (2.21)$$

The auxiliary WF's are simply the plane wave parts of the full WF's, which translate into the WF's of the pseudopotential approach.

Further we know that the full WF is more complete thus we can write the transformation as an identity and the sum of atomic contributions  $\hat{\mathcal{S}}_R$

$$\hat{\mathcal{T}} = \hat{1} + \sum_R \hat{\mathcal{S}}_R \quad (2.22)$$

Since  $\hat{\mathcal{S}}_R$  is each atoms local contribution it is defined in terms of all electron (AE) partial waves  $|\phi_i\rangle$  which are the solutions of the Schrödinger equation for the isolated atoms at a specific energy  $\epsilon_i$  and for a specific angular momentum  $l_i$ .

$$\psi(\vec{r}) = \sum_{i \in R} \phi_i(\vec{r}) c_i \quad \text{for} \quad \left| \vec{r} - \vec{R}_R \right| < r_{c,R} \quad (2.23)$$

Since the frozen core approximation is being used, the density and energy of the core electrons of isolated atoms. And the transformation  $\hat{\mathcal{T}}$  only produces WF's that are orthogonal to the core electrons, while the core electrons are treated separately. Meaning that these atomic partial waves only include valence states that are orthogonal to the core WF of the atom. And for these partial waves  $|\phi_i\rangle$  we also choose auxiliary waves  $|\tilde{\phi}_i\rangle$  such that:

$$\begin{aligned} |\phi_i\rangle &= \left( \hat{1} + \hat{\mathcal{S}}_R \right) |\tilde{\phi}_i\rangle \quad \text{for} \quad i \in R \\ \hat{\mathcal{S}}_R |\tilde{\phi}_i\rangle &= |\phi_i\rangle - |\tilde{\phi}_i\rangle \end{aligned} \quad (2.24)$$

The pseudo partial waves  $|\tilde{\phi}_i\rangle$  are equivalent to the AE partial waves outside a core radius  $r_{c,R}$  and match continuously onto  $|\phi_i\rangle$  inside the core radius:

[63]: Blöchl (1994), *Projector augmented-wave method*

[64]: Kresse et al. (1999), *From ultrasoft pseudopotentials to the projector augmented-wave method*

The partial waves are not bound states so they are not normalizable unless you truncate them beyond  $r_{c,R}$ .

$$\phi_i(\vec{r}) = \tilde{\phi}_i(\vec{r}) \quad \text{for } i \in R \quad \text{and} \quad \left| \vec{r} - \vec{R}_R \right| > r_{c,R} \quad (2.25)$$

Now to be able to work the transformation operator on an arbitrary auxiliary wavefunction we need to define it into the auxiliary partial waves:

$$\tilde{\psi}(\vec{r}) = \sum_{i \in R} \tilde{\phi}_i c_i = \sum_{i \in R} \tilde{\phi}_i(\vec{r}) \langle \tilde{p}_i | \tilde{\psi} \rangle \quad \text{for} \quad \left| \vec{r} - \vec{R}_R \right| > r_{c,R} \quad (2.26)$$

This is done with the help of the projector functions  $|\tilde{p}_i\rangle$ . Now one can apply  $\hat{S}_R$  to the the previous expression to obtain the true wave function:

$$|\psi_{n\mathbf{k}}\rangle = |\tilde{\psi}_{n\mathbf{k}}\rangle + \sum_i (|\phi_i\rangle - |\tilde{\phi}_i\rangle) \langle \tilde{p}_i | \tilde{\psi}_{n\mathbf{k}} \rangle \quad (2.27)$$

With the auxilarry wavefunction and the auxillary partial wave being expressed in term of a plane wave sum:

$$\langle \mathbf{r} | \tilde{\psi}_{n\mathbf{k}} \rangle = \frac{1}{\Omega^{1/2}} \sum_{\mathbf{G}} C_{n\mathbf{k}\mathbf{G}} e^{i(\mathbf{G}+\mathbf{k})\cdot\mathbf{r}} \quad (2.28)$$

Here  $\Omega$  is the volume of the Wigner - Seitz cell, and  $\mathbf{G}$  is the wave vector in question. These wave vectors go to up to  $\mathbf{G}_{max}$  which in VASP is defined by the plane wave cut-off energy:

$$E_{PW} = \frac{\hbar^2 \mathbf{G}_{max}^2}{2m_e} \quad (2.29)$$

The energy here is given in Rydberg units of energy [Ry]. There are more considerations to be made when calculation the electron density using this plane wave representation shown here, but they are not discussed here.

## 2.2.2 Structure optimization

As part of this research the structures are optimized. While the reasons why one might want to do it are obvious, the methods are not, this chapter is dedicated to how.

As we saw in eq. 2.1 part of the total energy of our system comes from nuclei - nuclei interaction of nuclei located at  $\mathbf{R}_1, \mathbf{R}_2 \dots \mathbf{R}_M$ . Thus our potential energy of this interaction is a function of these locations. And there is an *equilibrium* structure, for which the potential energy is minimum:

$$U(\mathbf{R}_1^{eq}, \mathbf{R}_2^{eq} \dots \mathbf{R}_K^{eq}) = \min U(\mathbf{R}_1, \mathbf{R}_2 \dots \mathbf{R}_K) \quad (2.30)$$

While this is a useful relation it is not particularly helpful. If you start with locations  $\mathbf{R}_1, \mathbf{R}_2 \dots \mathbf{R}_M$  you do not a priori know *where to go* in this three dimensional potential landscape. You could try and move in a

random direction and see if it helps, but this is very time consuming, and you will spend time calculating steps that do not contribute to lowering of the energy in any way. Lucky there is a better way, you could move in the direction of the forces <sup>14</sup>:

$$\mathbf{F}_I = -\nabla_I U(\mathbf{R}_1, \mathbf{R}_2 \dots \mathbf{R}_K); \quad I = 1, 2 \dots K. \quad (2.31)$$

Where the  $\nabla_I$  denotes the gradient with respect to the ionic position  $\mathbf{R}_I$ . Now we just need to know how to calculate the forces. This is where we can use the *Hellman-Feynman* [65] theorem.

**Theorem 2.2.2** *The Hellmann-Feynman theorem states that given the solutions to the Schrödinger equation  $\hat{H}_\lambda \psi_\lambda = E_\lambda \psi_\lambda$ , where the Hamiltonian  $\hat{H}_\lambda$  depends on a parameter  $\lambda$ , and  $\psi_\lambda$  is a normalized function,  $\langle \psi_\lambda | \psi_\lambda \rangle = 1$ , the following relation holds:*

$$\frac{dE_\lambda}{d\lambda} = \langle \psi_\lambda | \frac{d\hat{H}_\lambda}{d\lambda} | \psi_\lambda \rangle \quad (2.32)$$

Now within DFT we do not have this classic potential energy expression, but we do have the Hamiltonian which depends on the ionic positions  $\mathbf{R}_I$ , so we can express the force in this way:

$$\mathbf{F}_I = -\nabla_I E_0 = \langle \psi_0(\mathbf{R}) | \nabla_I \hat{H}[\mathbf{R}] | \psi_0(\mathbf{R}) \rangle \quad (2.33)$$

Which in this case comes down to the difference in nuclei-nuclei and electron-nuclei interactions, and these depend on your ground state density, which again depends on  $E_{xc}$ . The way you approach this self consistently is that you converge a KS calculation, then from the GS density you calculate the forces. Then you move the nuclei and begin again.

### 2.2.3 Charge analysis methods

The main goal of this thesis is evaluating possible charge transfer. To do this we need to define what we consider charge belonging to an atomic site. There are 2 (4) I will discuss here. These two ways we can divide into two groups:

1. Charge density based methods - Bader charge analysis (Density integration)
2. Wave function based methods - Löwdin (Mulliken) population analysis

#### Bader charge analysis

Since we are explicitly dealing with charge densities, the simplest way to find out how much charge is at some location  $\mathbf{R}$  is to *simply integrate the charge*. Now, for this integral, how do you define where one atom ends and another one starts?

14: Writing the force as the negative gradient of the potential energy arises from solving the Lagrangian of the second kind with the Lagrangian of the N particle system  $L = \sum_{i=1}^N m_i \mathbf{v}_i^2 - V(\mathbf{r}_i)$

[65]: Feynman (1939), *Forces in Molecules*



15: This is the same  $r_s$  as discussed in the LSDA section.

So if we wanted to know *say* the WZ radius of Iron, we could take one mol of solid Fe and measure its volume, then divide this volume by the Avogadro number and obtain the volume of the sphere whose radius is the WZ radius.

[66]: Bader (1985), *Atoms in molecules*

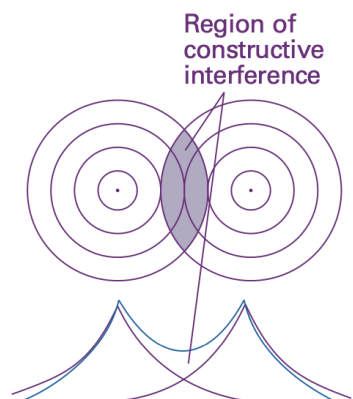


**Figure 2.4:** A representation of hydrogen bonding with the resultant molecular orbital being the blue line, taken from [67].

[68]: Tang et al. (2009), *A grid-based Bader analysis algorithm without lattice bias*

If we view atoms as *spheres* held together by bonding *sticks*, then the logical way is to integrate all the charge density in this sphere. This is still done very often, and was also used as proof in the computational paper by Zhong and Hansmann. The radius often chosen is the Wigner–Seitz radius  $r_s$ <sup>15</sup>. This radius is defined as the radius of a sphere which has the average volume of an atom in the bulk solid of said material.

As one might imagine a value extrapolated from a bulk of a monolithic material does not always work in complex materials, especially when the material exhibits covalent bonding. Nevertheless I will provide this value for the bulk materials as a reference point.

Another way to define where one atom ends and the other begins is to look at the charge density. If we think of atoms as these *blobs* of electronic densities as it is often depicted in chemistry books when talking about bonding, then we can just find the place where the density is at the minimum and cut the atom off there.

A visual example seen in figure 2.4, it is easy to see where one would "cut" to obtain the densities belonging to each of the atoms.

This approach was defined by Richard F.W. Bader [66], the exact way of "cutting" the density in 3D is mathematically involved and further discussed in his publications, hence it will not be discussed here.

The exact code used to compute the Bader charges is described in [68], and was written for VASP by members of the Henkelman Group.

The only gripe with this method is that in cases where covalent or metallic bonding takes place, it can locally over-predict the actual charge at a site as this technique does not bode well with "shared" electrons. Thus making covalent bonding look more ionic.

### Löwdin (Mulliken) charge analysis

The Löwdin (and Mulliken) way of approaching charges is based on wavefunctions and their interactions. This method is rooted in the idea of Linear Combination of Atomic Orbitals - **LCAO**, where we can express the Molecular orbital  $\phi$  as a sum of Atomic orbitals  $\chi$ :

$$\phi_i = c_{ij}\chi_j + c_{ik}\chi_k$$

A visual representation of this can be seen in figure 2.4 again, here the two purple atomic orbitals form the blue molecular orbital. The middle part where they intersect is the *overlap population* between two orbitals.

When all the overlaps for an orbital are calculated, they are subtracted from the initial orbital giving *net population*. Now the *gross population* of an orbital  $\mu$  overlapping with other orbitals  $\nu$  is:

$$\mathbf{GP}_\mu = \mathbf{NP}_\mu + \frac{1}{2} \sum_\nu \mathbf{OP}_{\mu\nu} \quad (2.34)$$

After that one just adds up the orbital gross populations of the occupied orbitals, giving you the *Mulliken charge* of an atom.



To obtain Löwdin charges, the same method is used but the atomic basis functions are orthogonalized via application of Löwdin's symmetric orthogonalization (LSO) [69]. This supposedly improves the description in crystalline solids. Because of this Löwdin population will be used, in case there is a large discrepancy Mulliken populations will also be disclosed. (In most cases the difference is not very large)

These methods are heavily influenced by what you consider to be the *atomic orbital*. In non plane-wave basis set methods the results are heavily basis set dependant, in plane wave methods the results depend on your choice of projections. The exact method used in this work is described in [70]. This method is part of the LOBSTER package and uses a robust projection method originally described in [71]. The exact implementation of this projection somewhat deviates from the original and is described in [72].

[69]: Löwdin (1950), *On the Non-Orthogonality Problem Connected with the Use of Atomic Wave Functions in the Theory of Molecules and Crystals*

[70]: Ertural et al. (2019), *Development of a robust tool to extract Mulliken and Löwdin charges from plane waves and its application to solid-state materials*

[71]: Sanchez-Portal et al. (1995), *Projection of plane-wave calculations into atomic orbitals*



# A reproduction and extension of the work of Zhong and Hansmann

# 3

With the theoretical basis in place, a good starting place would be where Zhong and Hansmann left off. In this chapter I will attempt to reproduce the results of the computational paper and also add  $LaNiO_3$  to these results, as it was not included in the original paper. Furthermore I will discuss the implications of their assumptions that lead to their prediction.

## 3.1 Methods and Reproduction

The paper [15] does not go into very much detail about the calculations themselves, so I contacted the main author of the paper - Zhicheng Zhong for more details. This allowed me to perform the same calculations as in the paper. The methods used were as follows:

1. The calculations were done on PBE relaxed cubic unit cells
2. The modified Becke-Johnson exchange correlation functional [73] was used to calculate the DoS<sup>1</sup>
3. The calculations were not run in a spin-polarized fashion
4. Wannierization<sup>2</sup> was performed to obtain the orbital character of the states
5. The numbers presented as the band averages are the first moments of the O2p states right below  $E_f$  and the TM3d states near  $E_f$

When reproducing the results, I used VASP's in-built orbital projection scheme, in which Kohn-Sham states are projected onto spherical harmonics, to obtain the O 2p and TM 3d density of states. Even though, this procedure differs from the Wannierization used in [15], the results are in good agreement, indicating that the details of the orbital projection scheme and exact definition of the O 2p and TM 3d states is not relevant.

To obtain the first moments of the O2p states the first fully occupied state below the Fermi Energy was used, here arises the first problem encountered. The exact definition of these states is a bit arbitrary as DOS do not fully go to zero in-between the more pronounced structures, so at some points one has to make a choice on what to call the *state*. Here the *state* is chosen as the first set of continuous states that span more than one eV, and whose total state count is similar in number to the ones of a given TM or La above  $E_f$ . This meant excluding small sets of states such as the ones seen in figure 3.2 for  $LaCoO_3$ .

In fig. 3.1 I show my reproduction of the results. Here added results of a hybrid functional are seen, this choice will be explained later. Interestingly enough, or rather unexpectedly  $LaNiO_3$  does not follow the trend of the previous materials of an ever rising O2p level average.

3.1 Methods and Reproduction 27

3.2 Critique and Explanation . 29

[15]: Zhong et al. (2017), *Band Alignment and Charge Transfer in Complex Oxide Interfaces*

[73]: Tran et al. (2009), *Accurate Band Gaps of Semiconductors and Insulators with a Semilocal Exchange-Correlation Potential*

1: The mBJ functional is a potential only meta-GGA functional meaning that it has no definition of  $E_{xc}$

2: Wannier functions are an alternative state representation of periodic systems, the functions themselves can be considered *molecular orbitals* thus giving way to projections. The process to obtain them is somewhat involved, and beyond the scope of this thesis [74].

**Figure 3.1:** Partial remake of the results found in the fig. 1.6. With  $\text{LaNiO}_3$  added in the same computational fashion, all results are extended with the results obtained with a spin-polarized HSE06 calculation. Only the O2p states are plotted, as in the original paper, it is theorised that only the O2p location with respect to the Fermi level matters.

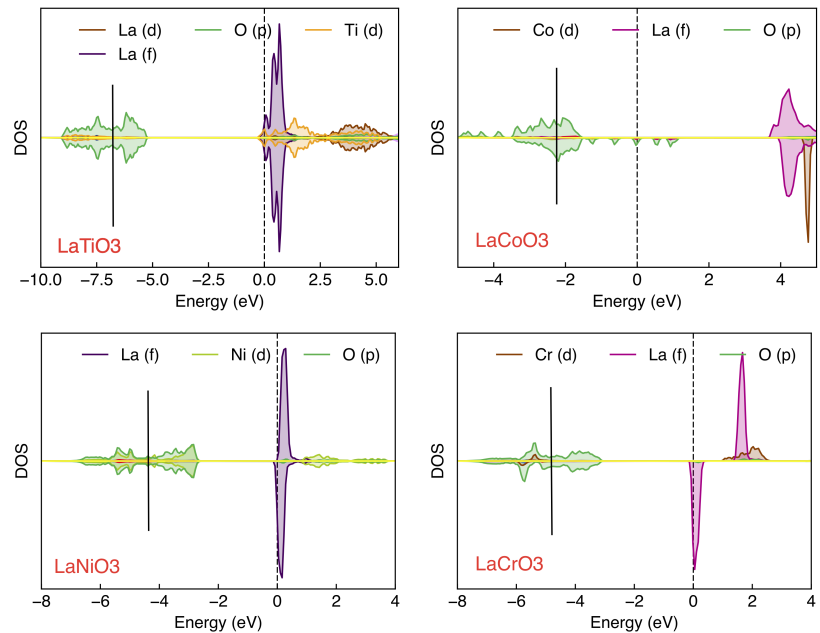
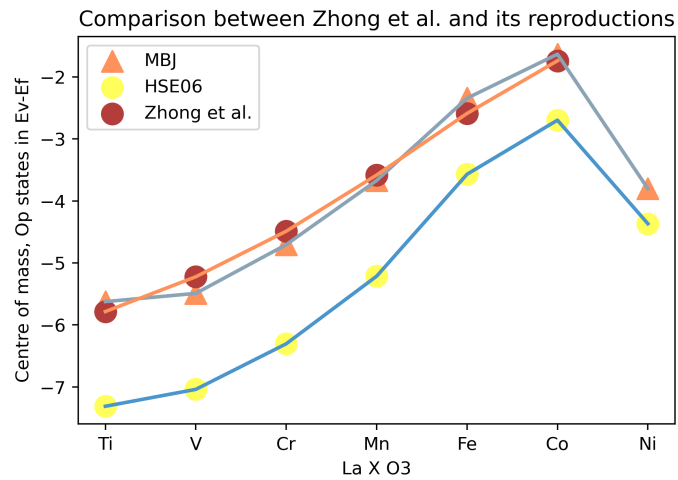


**Figure 3.2:** The DoS plots of select compounds found in the paper. Here the mBJ functional is also used, however here the calculation is done in a spin polarized way. The VASP local projection labels are added to the legend.

In fig. 3.2 I have plotted select DoS plots calculated the same way as the paper suggests with the averages of the O2p levels marked with black. These results were produced with a spin-polarized calculation meaning that the electron density is separated into up and down populations as discussed in the theory section. The non-spin polarized results are qualitatively similar.

Many DoS in fig. 3.2 have La-f states crossing the Fermi level, indicating that the perovskites are metallic in nature. Firstly from figure 1.2 it is expected that the A site states should be far from the Fermi level, meaning that this representation is somewhat un-physical. Secondly many of these perovskites are not metals, but this will be discussed later.

## 3.2 Critique and Explanation

In the light of these results, it is worth pondering upon their validity. Thankfully as part of the thesis of Kleibeuker there is a handy diagram highlighting the main electronic properties of the La-TM oxides:

LaMO <sub>3</sub>	3d <sup>x</sup>	electronic behavior	U(e V)	Δ(e V)	magnetic behavior
LaTiO <sub>3</sub>	3d <sup>1</sup>	MH	0.1	4.5	antiferromagnetic
LaVO <sub>3</sub>	3d <sup>2</sup>	MH	1.1	4.0	antiferromagnetic
LaCrO <sub>3</sub>	3d <sup>3</sup>	CT	-	3.4	antiferromagnetic
LaMnO <sub>3</sub>	3d <sup>4</sup>	CT	-	1.1	antiferromagnetic
LaFeO <sub>3</sub>	3d <sup>5</sup>	CT	-	2.2	antiferromagnetic
LaCoO <sub>3</sub>	3d <sup>6</sup>	CT	-	0.6	paramagnetic
LaNiO <sub>3</sub>	3d <sup>7</sup>	metallic	-	0	paramagnetic
LaCuO <sub>3</sub>	3d <sup>8</sup>	metallic	-	0	paramagnetic

**Table 3.1:** Physical properties of *LaMO<sub>3</sub>* at low temperatures. An overview from the PhD thesis of Josee E. Kleibeuker [18]

The table 3.1 contains a lot of information. The second column displays the number of electrons in the 3d band for each material. The third, fourth and fifth columns contain information pertaining to the type of electronic behaviour, a small explanation of their meaning is provided in the inset figure 3.3.

When comparing the DoS from figure 3.2 to the information found in table 3.1 one can observe that *LaTiO<sub>3</sub>* is not a Mott-Hubbard insulator, *LaCoO<sub>3</sub>* is also not a Charge-Transfer insulator. *LaCrO<sub>3</sub>* might be considered one if the La-f states are excluded, and *LaNiO<sub>3</sub>* appears to be metallic as intended although the states crossing  $E_f$  are again La-f.

So what is the cause of this *misrepresentation*? Apparently this phenomenon is a known issue when DFT is used to calculate properties of materials in a way where the real structure or symmetry breaking properties such as magnetic ordering are not considered. In many places, and even in the experimental paper [20] discussed previously, this difference in behaviour is attributed to the failures of DFT to fully describe correlated materials. This is not the case as illustrated in a landmark paper by Malyi and Zunger [76]. In this paper they highlight that more often than not it is ones choice of computational simplification that leads to an incorrect electronic description.

Different causes of incorrect electronic description can be found in fig. 3.4. There are many of them and sadly one cannot be sure which one is the one needed until it is tried. One thing that we can improve very quickly is the choice of functional. As described in the theory section HSE06 is better at describing complicated materials. So the structures were re-calculated using HSE06. The initial qualitative agreement of HSE06 results with the results found in the original work of Zhong and Hansmann can be seen in fig. 3.1.

These calculations can be seen in fig. 3.5. Now if we compare the results then *LaTiO<sub>3</sub>* is still a metal however the La-f states have been pushed up in energy, *LaCoO<sub>3</sub>* has become an insulator, although it is still arguable whether or not it is of the Charge-Transfer type. *LaNiO<sub>3</sub>* is a proper metal with TM states crossing the Fermi level continuously. *LaCrO<sub>3</sub>*, just like *LaTiO<sub>3</sub>* is still a metal, and just like with *LaTiO<sub>3</sub>* if one would consider the sub-gap as the actual gap then it would be a Charge-Transfer insulator.

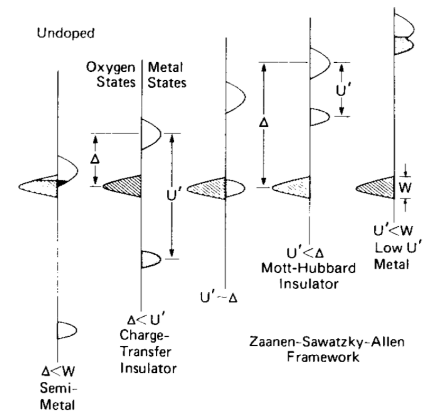


**Figure 3.3:** A visual explanation of correlated oxide insulator and metal types according to their electronic structures [75].

[76]: (2020), *False metals, real insulators, and degenerate gapped metals*

Cause of False Metal		Cause of gapping false metal	Example
Computational	Insufficient constraints on XC functional	XC distinguishing occupied from unoccupied states	All systems
		XC which reduces self interaction error	
	Restricting unit cell disallowing symmetry breaking	Flexible representation for the unit cell	
Symmetry breaking motifs	Ignoring local magnetic motifs	Magnetic order	CuBi <sub>2</sub> O <sub>7</sub> , NiO, all magnets below
		Different local spin environments	PM LaTiO <sub>3</sub> , PM YTiO <sub>3</sub> , PM NiO, PM YNiO <sub>3</sub>
	Ignoring local structural/orbital motifs	Octahedral tilting	SrBiO <sub>3</sub> , BaBiO <sub>3</sub> , Li(TiO <sub>2</sub> ) <sub>16</sub>
		Atomic displacement	
		Disproportionation	YNiO <sub>3</sub> , SmNiO <sub>3</sub> *
		$Q_2^+$ distortion	Cubic LaMnO <sub>3</sub> *
	Ignoring defect induced symmetry breaking	Defect formation	Ba <sub>x</sub> As <sub>3-x</sub> , Ag <sub>3</sub> Al <sub>22</sub> O <sub>34</sub>
Ignoring spin-orbit coupling	Allowing spin-orbit coupling	CaIrO <sub>3</sub> , Sr <sub>2</sub> IrO <sub>4</sub>	

**Figure 3.4:** A table from [76] listing the most common causes of unexpected electronic behaviour.

Even though this is not perfect the results seem to be more in line with experimental observations, and pen-and-paper predictions. In light of this improvement we can reproduce a version of fig. 1.6 with HSE06, this reproduction is displayed in fig. 3.6.

In this reproduction it can be seen that the trend still continues if the data is extracted and processed the same way it was done in the Zhong paper, with  $LaNiO_3$  still being an outlier. Nevertheless, the new-found idea, or rather a *glaring problem* of correct material representation leads to a rethinking of the validity of the theoretical predictions of Zhong and Hansmann.

If we take our DoS and try to visualize the kind of band alignment driven charge transfer between two of these materials, one quickly comes across a conceptual problem. Such a plot can be seen in fig. 3.7. In this plot the DoS of the two perovskites are aligned according to the averages of the O2p states under  $E_f$ , just as suggested by Zhong and Hansmann in fig. 1.5 (c). The black lines are their individual constituent Fermi levels, and the red line would then be the new Fermi level once the two materials make contact. Here we see a conceptual problem - if we correctly predict experimental like insulating behaviour in these materials then the materials would not have free states to receive electrons at, so this theory would work if these were metals.

Overall this does not paint a good picture for this band alignment theory. However we still have to see if the theory actually fails if we actually put the two materials together and calculate the superstructure.

Fina

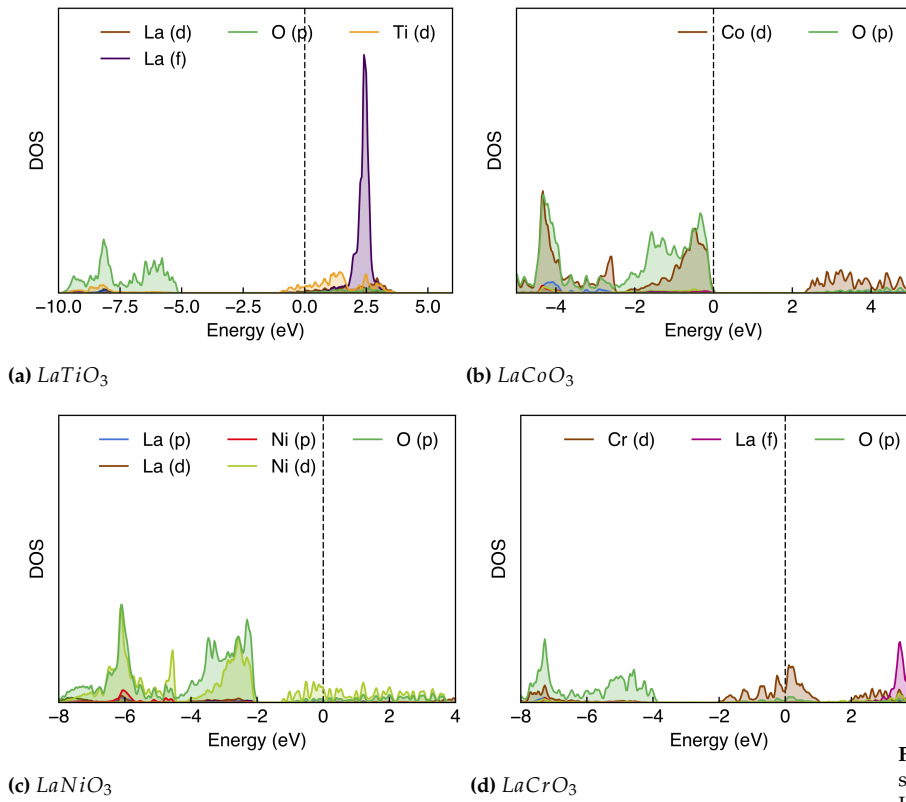


Figure 3.5: The DoS plots of the same structures as before, but now done with HSE06.

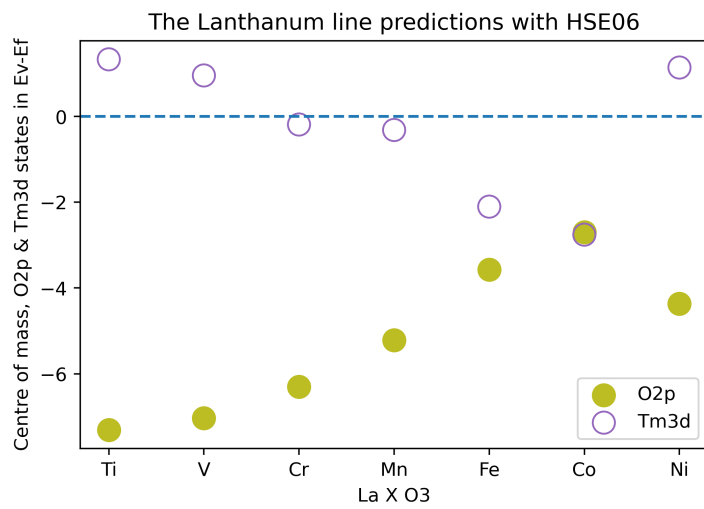
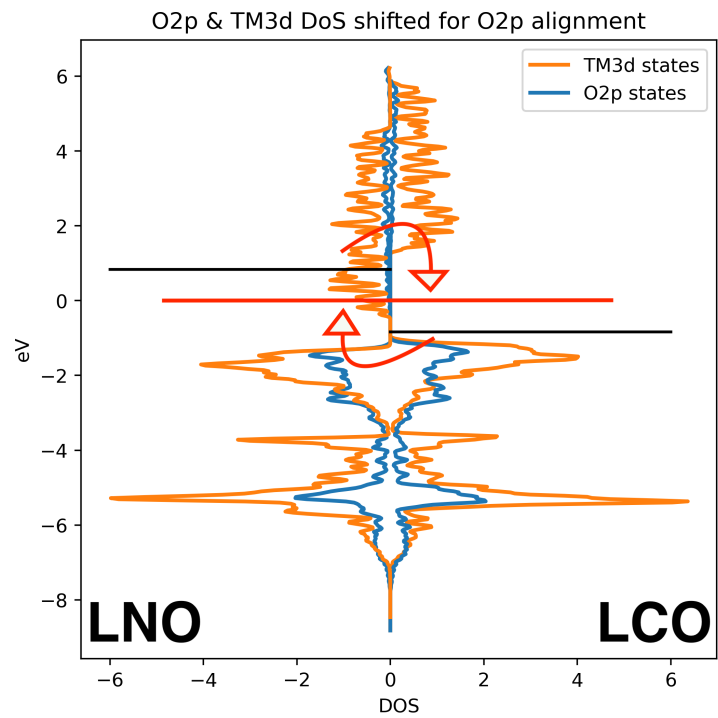


Figure 3.6: A full remake of the  $LaTMO_3$  series from fig. 1.6 using HSE06 and including the TM3d averages



**Figure 3.7:** A side-by-side plot of two DoS around  $E_f$  with the DoS aligned according to their O2p bands as suggested by Zhong and Hansmann.



# A closer look at the materials

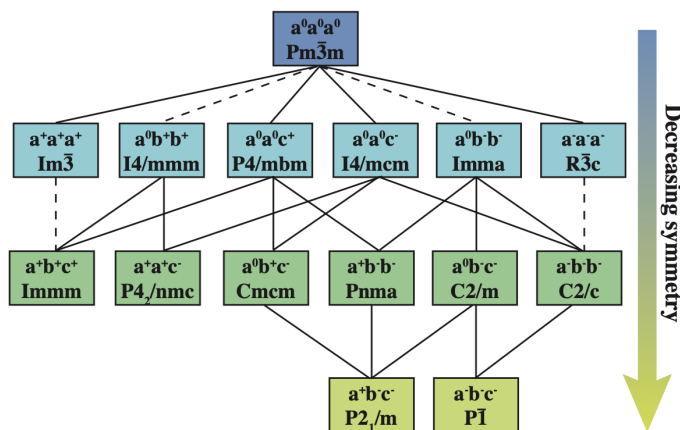
In the light of the Malý and Zunger paper, it is apparent that modelling these materials is challenging due to the intricate coupling of structure, electronic structure, and magnetic properties. In this chapter, I will validate my computational choices by comparing DFT results for the relevant bulk TM oxides with experiment. And establish reference values to be used for examining later calculations.

## 4.1 Structure and U parameter choice

Structure is one of the main input files in VASP, without it one cannot do any calculations so it makes sense start here.

When it comes to structure, it is often reported in Hermann–Mauguin notation, whereas chemists more often refer it in the Glazer notation [77]. The glazer notation describes the structures in terms of the tilting of the octahedra rather than symmetry operations.

There are far more space groups than glazer tilt systems and the mapping of tilt systems onto space groups is not unique, but to give the reader a good understanding of the structural distortions a mapping can be found in figure 4.2.



In this chapter the both the *experimental* structures with distortions as well as the simple cubic ( $Pm\bar{3}m$ ) versions will be explored and their differences highlighted. These structures are relaxed and their properties are calculated with PBE+U as well as HSE06. The U parameter is obtained from literature.

Thankfully the physical structures of these compounds have been well researched in the past. With large scale studies on the physical properties such as the one from Koehler and Wollan [81] being commonplace.

<b>4.1 Structure and U parameter choice</b>	<b>33</b>
4.1.1 <i>LaFeO<sub>3</sub></i> Structure	34
4.1.2 <i>LaCoO<sub>3</sub></i> Structure	36
4.1.3 <i>LaNiO<sub>3</sub></i> Structure	38
<b>4.2 Valence and Magnetism</b>	<b>40</b>
4.2.1 <i>LaFeO<sub>3</sub></i> Valence and magnetism	40
4.2.2 <i>LaCoO<sub>3</sub></i> Valence and magnetism	42
4.2.3 <i>LaNiO<sub>3</sub></i> Valence and magnetism	46
<b>4.3 Density of states and comparison to PES</b>	<b>48</b>
4.3.1 <i>LaFeO<sub>3</sub></i> DoS and PES	49
4.3.2 <i>LaCoO<sub>3</sub></i> DoS and PES	51
4.3.3 <i>LaNiO<sub>3</sub></i> DoS and PES	55
<b>4.4 Conclusions</b>	<b>57</b>

[77]: Glazer (1975), *Simple ways of determining perovskite structures*

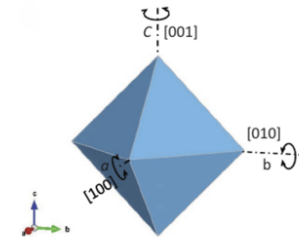


**Figure 4.1:** The Glazer notation uses letters abc to represent tilts along the axes. The use of the same letter twice or more implies same tilting amplitude. The superscripts +, -, 0 describe in phase, out of phase and zero tilt systems. Image from [78].

**Figure 4.2:** The dotted lines represent Landauer phase transitions of the first kind (they have to be discontinuous). Adapted from [79], color version from [80].

[81]: Koehler et al. (1957), *Neutron-diffraction study of the magnetic properties of perovskite-like compounds LaBO<sub>3</sub>*

### 4.1.1 $LaFeO_3$ Structure

There have been neutron diffraction [81] and powder XRD [82–88] studies on the  $LaFeO_3$  structure. All of them found the structure to be orthorhombic in the  $Pnma$ (#62) space group with substantial deviations from the cubic structure,  $a^+b^-b^-$  in glazer notation. Nevertheless some still report the pseudo cubic lattice parameters [81, 84]. At a temperature of around 1228 K ( $\approx 955^\circ\text{C}$ ) the material exhibits a phase transition and turns to  $R\bar{3}c$  [89], but since this temperature is very high we can ignore this phase.

Next are the chosen structures which will represent the material, which can be seen in figures 4.3 and 4.4.

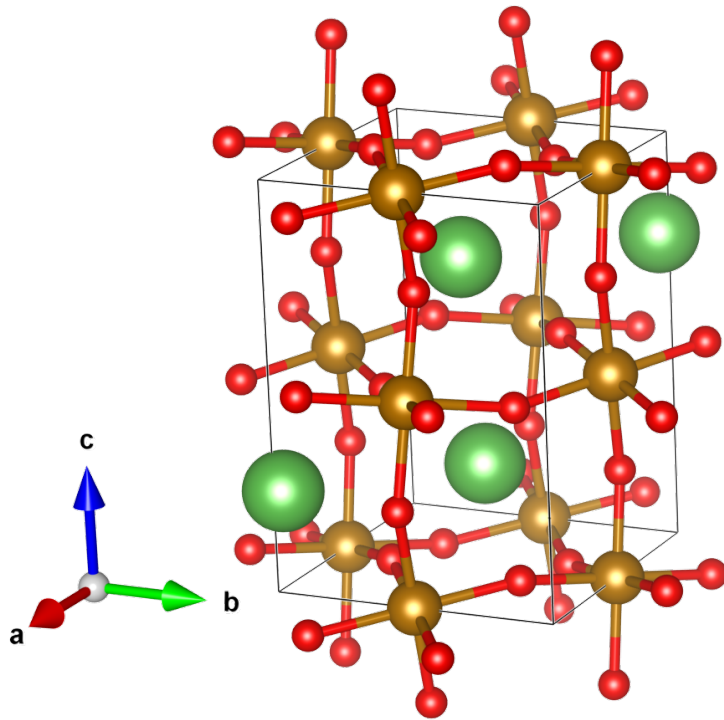


**Figure 4.3:** The  $LaFeO_3$   $Pnma$ (#62) unit cell. The image shows connected bonds and atoms just outside the unit cell, but the actual cell has four formula units  $4LaFeO_3$ .

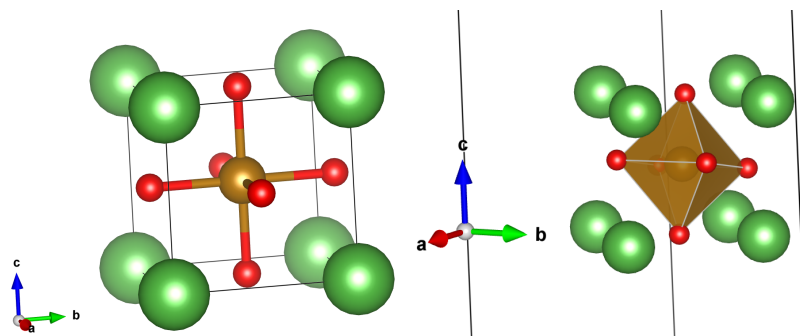


**Figure 4.4:** On the right is the  $LaFeO_3$  simple cubic cell. On the left you can find the pseudocubic cell of the  $Pnma$  structure with its  $a^+b^-b^-$  distortions as an illustrative example.

Previous literature has studied the material with the use of GGA and LDA functionals [90, 91], and it was found that this formalism was not sufficient to obtain good lattice parameters, bandgaps or magnetic moments, especially so for the cubic model which is predicted to be metallic by these functionals. Many authors [91–94] have used a Hubbard

U parameter to compensate for the problems of (semi)local functionals, as discussed in Chapter 2.1.3.

And when it comes to the U parameter it seems that GGA+U is better than LSDA+U at reproducing more of the desired parameters at the same time, both for the cubic and orthorhombic cases [90, 91, 93].

The limiting range for a U parameter to be used with PBE was set by Davis George Daniel [87] to be between 4-6 eV. And indeed a choice of U in that range shows a good match with most observables [91]. A fairly recent in depth analysis of the experimental bandgap, coupled with a newer study this was revised to 4.64 eV [95], as a better fit for the bandgap. Thus PBE+4.64U is used for the remainder of this work for  $LaFeO_3$ .

The relaxed lattice parameters of both  $LaFeO_3$  structures can be seen in table 4.1.

Orthorhombic lattice par. Å	a	b	c	Cubic lattice par. Å	a
Experimental [82-88]	$5.553 \pm 0.005$	$5.565 \pm 0.003$	$7.856 \pm 0.006$	Experimental [81, 84]	3.927
PBE+U ( $U = 4.64$ )	5.503	5.509	7.765		3.941
Error %	-0.9%	-1%	-1.2%		+0.4%

[87]: Daniel (2014), *The Electronic and Thermodynamic Properties of Ca doped  $LaFeO_3$  – A First Principles Study Using Density Functional Theory*

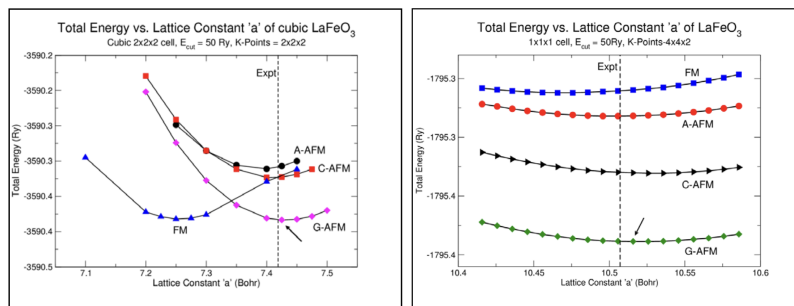
**Table 4.1:** The calculated lattice parameters of  $LaFeO_3$  compared to the experimental ones.

The  $Pnma$  structure did exhibit slight Jahn-Teller distortions during relaxation. The glazer tilts were found to be  $a = 1.25^\circ$  and  $b = 8.33^\circ$ , no experimental values were found for comparison.

It is quite surprising that the lattice parameters are erred on the negative side for the Orthorhombic structure. This is much unexpected, largely due to the fact that one expects GGA functionals to overestimate the lattice parameters, and also because computational literature also report overestimation.

There is an explanation to this result. In fig. 4.5b one can see that if the cell is initialised in a ferromagnetic ground state, the lowest energy lattice parameters are lower than the experimental ones. On the other hand the results for the cubic lattice seem fine and in line with expectations, contrary to what fig. 4.5b might suggest. This probably is caused by the fact that in [87], the calculations are performed for  $2 \times 2 \times 2$  cubic cells, as other sources confirm FM like behaviour for larger cubic supercells [94].

As this difference is not drastic in this case and the error is in range of standard GGA over prediction error it is decided to continue with this structure.



**(a)** The magnetic ordering relation to the cubic unit cell size shows that one can enter a "false ground state". **(b)** Unlike for the cubic case, the G type anti-ferromagnetic structure, is always lowest in energy for the Orthorhombic cell.

**Figure 4.5:** Size and magnetism ordering relation in  $LaFeO_3$  in two different structures from [87]. The calculations were done with PBE.

### 4.1.2 $\text{LaCoO}_3$ Structure

[96]: Rondinelli et al. (2009), *Structural effects on the spin-state transition in epitaxially strained  $\text{LaCoO}_3$  films*

[97]: Ritzmann et al. (2014), *Ab initio DFT+U analysis of oxygen transport in  $\text{LaCoO}_3$ : the effect of  $\text{Co}^{3+}$  magnetic states*

[104]: Raccah et al. (1967), *First-Order Localized-Electron  $\leftrightarrow$  Collective-Electron Transition in  $\text{LaCoO}_3$*

[105]: Maris et al. (2003), *Evidence for orbital ordering in  $\text{LaCoO}_3$*

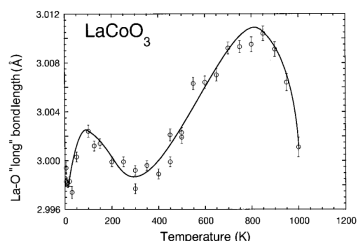


**Figure 4.6:** Anomalous temperature dependent behaviour of the La-O distance. [103]

[109]: Buckeridge et al. (2016), *Efficient and accurate approach to modeling the microstructure and defect properties of  $\text{LaCoO}_3$*

$\text{LaCoO}_3$  is a bit more complicated in terms of computational modelling, as it has a very tight relationship between the physical and electronic/magnetic structure with one giving positive feedback to the other and vice versa; and computational choices such as the choice of a particular functional also influence this [96, 97].

Early papers measuring the structure of  $\text{LaCoO}_3$  mention it as *distorted - pseudocubic* [98] [99], they report pseudo cubic lattice constants and rhombohedral angles. Onwards the material is generally reported as rhombohedral in the  $R\bar{3}c$  (#167) space group [100–103][104]. Some more recent work [105] using high-resolution x-ray diffraction measurements at 60 K ( $\approx -213^\circ\text{C}$ ) concluded that it is the  $C2/c$  (#15) space group.  $R\bar{3}c$  is a subgroup of  $C2/c$  with the difference being the latter allows for Jahn-Teller distortions. It is assumed that these are small, and will arise from the  $R\bar{3}c$  ( $a^-a^-a^-$  in glazer) structure if relaxed, so  $R\bar{3}c$  is used.

This reduced symmetry however explains the anomalous behaviour of lattice parameters seen in fig. 4.6, which would coincide with a phase transition from  $C2/c$  to  $R\bar{3}c$  as predicted in fig. 4.2. So the difference between the two structures is not nil and leads to measurable differences [106].

The anomalous lattice behaviour is attributed to the emergence of two differently sized Co-O octahedra. This splitting is not only thought to be temperature dependent, but also influenced by other factors as will be discussed in later sections. The presence of two distinct Co-O distances can be explained by the fact that high spin  $\text{Co}^{3+}$  has a larger ionic radius 0.61 Å compared to the low spin counterpart  $\text{Co}^{\text{III}+}$  with 0.545 Å [107]. This alludes to spin ordering, and shows that distortions and spin go hand in hand in this material.

As for computational choices James M. Rondinelli and Nicola A. Spaldin [96] showed in their work that LSDA is already quite good at reproducing properties of this material, and they established a reasonable upper bound on the U parameter of 4 eV for LSDA+U. This comes in sharp contrast to optimal U parameters obtained self-consistently, reported to be double that [108]. This choice of U parameter was confirmed for PBE by a large study by J. Buckeridge [109] showing good bandgaps and valence band DoS closely matching with experiment when using PBE+4U. As he concludes that a U parameter of 4 eV is *about as universal as you can get*, it will be used for the remainder of this work.

The structures used here are found in figures 4.7 and 4.8, with their relaxed lattice parameters found in tables 4.2 and 4.3.

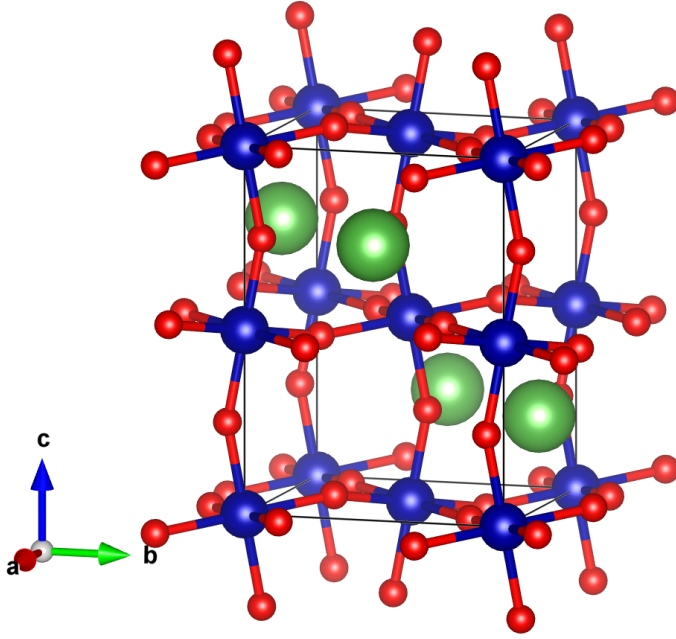


**Figure 4.7:** The  $LaCoO_3$   $R\bar{3}c$  (#167) rhombohedral unit cell in its hexagonal representation. The extra oxygens bonding outside the cell bounds are for illustrative purposes to make the octahedra more discernible. The actual cell has four formula units of  $4LaCoO_3$ .

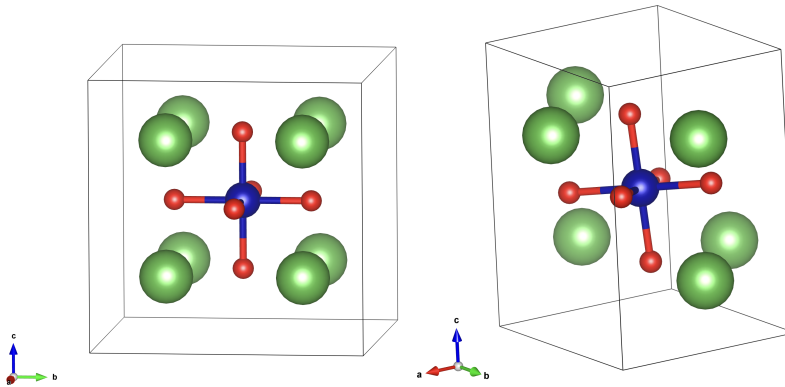


**Figure 4.8:** On the right is the  $LaCoO_3$  simple cubic cell. On the left you can find the  $R\bar{3}c$  pseudocubic cell with its  $a^- a^- a^-$  distortions as an illustrative example.

Hexagonal lattice parameters Å	a	c	Cubic lattice parameter Å	a
Experimental [81, 98–103, 110]	$5.436 \pm 0.01$	$13.107 \pm 0.03$	Experimental [98, 99, 111]	3.82
PBE+U ( $U = 4eV$ ) results	5.544	13.251		3.81
Error %	+2.0%	+1%		+0.2%

**Table 4.2:** The calculated lattice parameters of  $R\bar{3}c$  and simple cubic  $LaCoO_3$  compared to the experimental ones.

Surprisingly the  $R\bar{3}c$  cell did indeed relax into  $C2/c$  as reported in table 4.3, the normal parameters are also reported in table 4.2.

Monoclinic lattice parameters Å	a	b	c	$\beta$ (deg)	Co-O1	Co-O2
Maris et al. [105]	5.37	5.433	7.64	90.99	1.874	1.993
PBE+U ( $U = 4eV$ ) results	5.442	5.58	7.626	89.2	1.928	2.103
Error %	0.013 %	0.027 %	-0.001 %	-0.02 %	0.03 %	0.055 %

**Table 4.3:** The calculated lattice parameters of  $C2/c$  compared to the experimental ones. In this structure the two Co-O distances are discerned.

The substantially better match with  $C2/c$ , the space group which discerns two separate Co-O distances is a very interesting result. As the low temperature ground state should be  $R\bar{3}c$  with this Co-O distance separation only appearing near room temperature. The tilts found here were slightly different along each axis but the average was found to be  $8.58^\circ$  which is in agreement with the experimentally determined  $8.29^\circ$  by Vogt et al. [112].

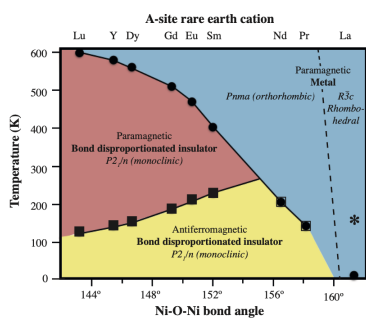


**Figure 4.9:** Phase diagram of RNiO<sub>3</sub> oxides from [113], colour version from [80].

[120]: Gou et al. (2011), *Lattice normal modes and electronic properties of the correlated metal LaNiO<sub>3</sub>*

[122]: Baeumer et al. (2021), *Tuning electrochemically driven surface transformation in atomically flat LaNiO<sub>3</sub> thin films for enhanced water electrolysis*

### 4.1.3 LaNiO<sub>3</sub> Structure

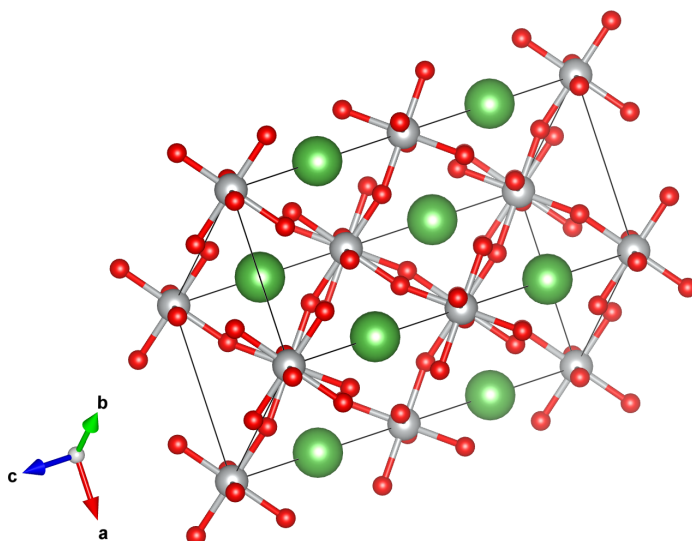
There are quite some studies detailing the physical structure of LaNiO<sub>3</sub>. Besides the aforementioned Neutron diffraction study [81], there is another large one [114] and some more XRD studies [115, 116].

In the natural unconstrained ground state LaNiO<sub>3</sub> appears to be Rhombohedral in the  $R\bar{3}c$  symmetry group and thus has the corresponding glazer notation of  $a^- a^- a^-$ . There is a phase transition from  $R\bar{3}c$  to  $Pm\bar{3}m$  (simple cubic), which was predicted [117] and observed [118]. It happens above  $T=1000\text{k}$  ( $\approx 727\text{C}$ ), so its safe to say that this phase is not observed anywhere near room temperature as one can see from the phase diagram in 4.9, and therefore it is not considered here.

In general the Rhombohedral phase is not something one would expect here knowing that this material is  $3d^7$  from table 3.1, and that it is low spin. With one  $e_g$  atom, normally this would lead to Jahn-Teller distortions, but here it does not. The origin of this unexpected phase is explained by the complex bonding environment [119].

As for the computational details, Gou et al [120] did a large computational study on the ground state properties of LaNiO<sub>3</sub> using many functionals. They find a self consistent U parameter of 5.74 eV, and highlight a good match with a U parameter found (5.7 eV) when fitting results of a many body approach (GWA) [121]. These results however were not very promising. Luckily there is a paper of a very similar system to what we want to look at - a many unit cell LaNiO<sub>3</sub> system - from Baeumer et al. [122]. Here they saw a good correspondence with UPS spectra and a match in out of plane lattice parameter with PBE+U (U = 2eV), and their other functional results were similar to the ones produced by Gou [120], meaning that we can directly compare the two results and conclude that a U parameter of 2eV is a substantially better choice for this problem compared to the higher self-consistently obtained values. The U parameter of 2 eV will be used for the remainder of this work.

**Figure 4.10:** The LaNiO<sub>3</sub>  $R\bar{3}c$  unit cell in question. It is the hexagonal representation of the cell, and the cell is displayed in a way where we are aligned with one of the pseudocubic axis, allowing one to see the octahedral distortions.





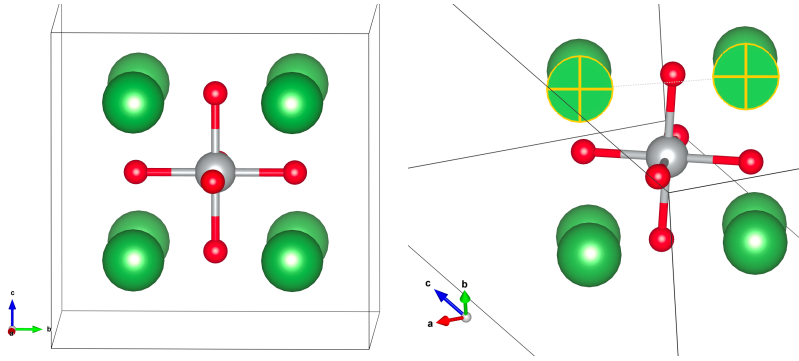


**Figure 4.11:** On the right is the simple cubic  $LaNiO_3$  cell. On the left you can find the  $R\bar{3}c$  pseudocubic cell with its  $a^-a^-a^-$  distortions as an illustrative example.

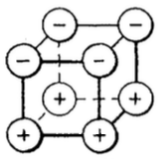
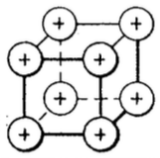
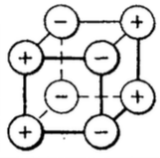
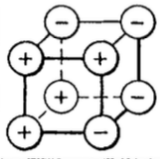
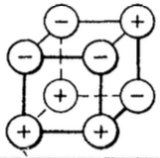
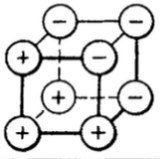
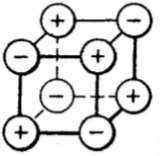
Hexagonal constants $\text{\AA}$	a	c	Ni-O-Ni dist.	Ni-O-Ni angle	Tilt angle
Experimental [81, 114–116, 123]	$5.456 \pm 0.004$	$13.147 \pm 0.027$	1.933	164.8	6.2 [124]
PBE+2U ( $U = 2eV$ )	5.517	13.111	1.96	160.3	6.93
Error %	+0.011%	-0.003%	+0.014 %	-0.027 %	+0.12 %

**Table 4.4:** The  $R\bar{3}c$  results compared to experimental results.

Cubic lattice parameter $\text{\AA}$	a
Experimental [81, 115]	3.838
PBE+2U ( $U = 2eV$ )	3.84
Error %	+0.001 %

**Table 4.5:** The cubic results compared to experimental results. The experimental results are the pseudocubic parameters given in early papers.

The results of the relaxed structures can be seen in tables 4.4 and 4.5. The results are as expected with most parameters being overestimated, except for the long hexagonal parameter.

LABEL	ONE OCTANT OF MAGNETIC UNIT CELL
A	
B	
C	
D	
E	
F	
G	

**Figure 4.12:** The original designation of possible magnetic orderings of a magnetic cubic lattice from [125] used to this day. This is an exhaustive list of possible co-linear magnetic orderings within a cubic lattice.

[125]: Wollan et al. (1955), *Neutron Diffraction Study of the Magnetic Properties of the Series of Perovskite-Type Compounds*  $[(1-x)\text{La}, x\text{Ca}]\text{MnO}_3$

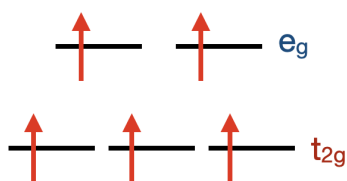


**Figure 4.13:** A schematic representation of the expected Fe high spin state in  $\text{LaFeO}_3$  from measurements and electron occupancy from table 3.1.

## 4.2 Valence and Magnetism

This section serves not only as a way to see if the materials are represented correctly but also as a tool to judge the larger set of results. By comparing the valence states and local magnetic moments of those results to these bulk calculations we can see what changes at the interface between two materials

Although these perovskites have a very complicated structure, it is mostly the TM atoms that contribute to magnetism. And thankfully the TM sublattice is cubic, meaning that we only have to consider the magnetic ordering of a cubic lattice. All possible orderings of such a lattice are found in figure 4.12.

Here both PBE+U and HSE06 will be used to evaluate both types of structures for each perovskite. Here the distorted structures calculated with the hybrid functional and experiment will be seen as a benchmark for the simplified systems evaluating their performance. This is done with the eventual goal in mind to use a "cheap" method later for larger structures.

### 4.2.1 $\text{LaFeO}_3$ Valence and magnetism

Low temperature coherent magnetic reflection experiments have shown an effective magnetic moment of  $4.6 \pm 0.2\mu_B$  at low temperatures [81], and a neutron diffraction measurement placed the local Fe magnetic moment at  $3.77\mu_B$  [86]. It is confirmed as a G-type anti-ferromagnet [81]. The anti ferromagnetic behaviour is also confirmed by the very low measured effective magnetisation [88, 126, 127]. And a Neel temp of  $\approx 730\text{ K} - 750\text{ K}$  ( $457^\circ\text{C} - 477^\circ\text{C}$ ) has been measured using a plethora of methods [86, 128, 129], meaning that the ground state of  $\text{LaFeO}_3$  is anti-ferromagnet for our purposes.

It is notable that below the Neel temperature AFM interaction is driven by super exchange through the oxygen ligands. This leads to  $\text{LaFeO}_3$  having some magneto-elastic coupling between the physical and electronic structure [86, 89]. Linked to this it seems that the octahedral distortions exhibit their maximum at the Neel temperature [89].

But unlike other TM-perovskites it seems that this coupling is not that strong, as pressure induced spin state changes are predicted to happen far out of reach of normal epitaxial pressures [93, 130], moreover it seems that uni axial compression in the range of epitaxial strain does little to the magnetic and structure parameters of the material [131], so we can expect this material to not have a complex spin-structure relationship.

There is a small caveat that has to be considered, this was already shown in figure 4.5a. It appears that the energy minimum for the FM and AFM-G structure is the same separated only by the difference in lattice parameters. Moreover [94] shows that large cubic structures tend to go into a false FM ground state.

To benchmark the performance of our functional and structure choices, we can first look at partial charge analysis data in table 4.6.



Cubic structure oxidation state overview				Pnma AFM-G oxidation state overview		
PBE+U						
Atom	Wigner-Seitz int.	Bader	Löwdin	Wigner-Seitz int.	Bader	Löwdin
La	2.66	2.12	1.37	2.75	2.07	1.26
Fe	1.05	1.77	1.71	1.12	1.94	1.66
O	0.97	-1.3	-1.03	0.94	-1.34	-0.98
HSE06						
La	2.75	2.22	1.44	2.54	2.19	1.34
Fe	1.12	1.92	1.77	1.14	2.05	1.73
O	0.94	-1.38	-1.07	0.92	-1.41	-1.03

An interesting conclusion arises - as you break symmetries by going to a more distorted structure (Pnma) and improve the functional description (HSE06) not only do the overall oxidation states increase but so does the difference between Löwdin and Bader oxidation states. The Wigner-Seitz integral provides a fairly un-physical answer for all situations. This can be explained by the very covalent nature of TM oxides as many electrons are shared in the interstitial space and are involved in covalent bonding.

Magnetisation $\mu_B$			
Cubic	Total	Fe - W-Z	Fe - Löwdin
PBE+U	5	4.41	4.22
HSE06	5	4.27	4.25
Pnma AFM-G			
PBE+U	0	4.2	4.12
HSE06	0	4.1	4.17

The local magnetic moment of Fe can be seen in table 4.8, surprisingly the local magnetic moment of Fe is not impacted by structure or functional choice. The cubic structure was tested with a single unit cell and is thus ferromagnetic. A similar conclusion can be made if one looks at the orbital projected occupancies of the Fe atom in figure 4.14. They are qualitatively similar, with *Pnma* favouring a different occupancy ordering for the minority spin channel.

Cubic			Pnma		
1   0.25	1   0.25		1   0.1	1   0.25	
$x^2-y^2$	$z^2$		$x^2-y^2$	$z^2$	
1   0.1	1   0.1	1   0.1	1   0.26	1   0.1	1   0.12
xy	yz	xz	xy	yz	xz

In figure 4.14 the orbital projected occupancies are shown. The ordering of the cubic result is quite unexplainable as there are no symmetries broken. Thus the expected  $O_h$  orbital ordering should hold, yet according to the occupancies it is flipped. The orthorhombic result however shows the symmetry breaking that accompanies the slight Jahn-Teller distortions mentioned previously, as these distortions are known to lower  $e_g z^2$  orbital energy [7].

On the basis of these results it is clear that PBE+U and the simple cubic representation does a good job at reproducing the experimental magnetic properties, but fails in regards to orbital occupancy.

**Table 4.6:** Atomic oxidation states obtained with a simple radius integral, a charge density based method (Bader) and a WF method (Löwdin). The nominal oxidation states of La and Fe are 3+ and -2 for Oxygen in  $LaFeO_3$ .

**Table 4.7:** The ground state magnetic ordering appears to be AFM-G. Computed with PBE+U, energy is given as difference to ground state in eV per formula unit.

Mag. Type	$\Delta$ [eV per f.u.]
FM	0.20
AFM-A	0.13
AFM-C	0.06
AFM-G	0

**Table 4.8:** The local magnetic moments of Fe. The total magnetisation is the difference between all the up and down spin densities. The other columns list the local magnetic moments, obtained as the difference between up and down densities locally on the Fe atomic site.

**Figure 4.14:** PBE+U resultant projected Löwdin orbital occupancies of the Fe 3d states. HSE06 delivered results that are qualitatively equal. The red is the spin up channel, while the blue is the spin down channel. Results are colour coded according to value.

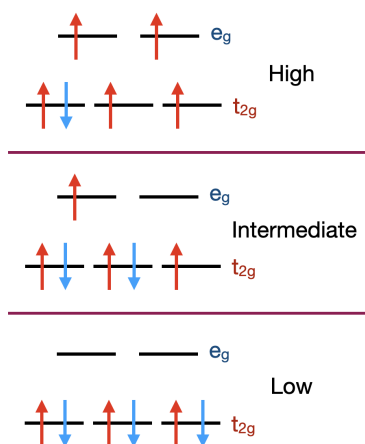


**Figure 4.15:** A schematic representation of the possible spin states of the Co ion in  $LaCoO_3$  according to the nominal  $3d^6$  occupancy found in table 3.1.

1: Early version of this model involved the idea of charge disproportionation with  $Co^{2+}$  and  $Co^{4+}$  ordering, however this has been debunked and the accompanying anomalous measurements have been attributed to non-stoichiometric and otherwise impure compounds [133–135].

**Table 4.9:** The ground state magnetic ordering appears to be AFM-G. Computed with PBE+U, energy is given as difference to ground state in eV per formula unit. Only four orderings were tested as the larger cell only has four Co atoms.

Mag. Type	$\Delta$ [eV per f.u.]
FM	0.033
AFM-A	0.172
AFM-C	0.101
AFM-G	0

**Table 4.10:** Oxidation states of cubic  $LaCoO_3$ . The nominal oxidation states of La and Co are 3+ and -2 for Oxygen in  $LaCoO_3$ .

	$d^6$	$d^7L$	$d^8L^2$
LS	29 %	53 %	17 %
IS	35 %	53 %	12 %
HS	49 %	44 %	7 %

**Figure 4.16:** Cluster model calculations of Saitoh [145], indicating the ligand-hole like behaviour of the Co ion in  $LaCoO_3$ .

## 4.2.2 $LaCoO_3$ Valence and magnetism

It has to be said that the exact magnetic, valence and spin properties of the Co ion in  $LaCoO_3$  are still under much debate with a plethora of conflicting publications and opinions. Adding to this lack of consensus, it appears that these properties are heavily influenced by physical distortions (e.g. epitaxy, pressure) and temperature. This chapter will attempt to place results in context of research that has come before.

The classical explanation to this behaviour introduced by Goodenough and revisited by Raccah and Rodriguez [104, 132, 133], relies on the struggle between exchange splitting  $E_{ex}$  and crystal field splitting  $\Delta$ .<sup>1</sup>

For  $LaCoO_3$   $E_{ex}$  and  $\Delta$  are roughly the same [136], and thus giving way to easily provokable transitions. Most sources agree that at very low temperatures the low spin phase is stabilized by  $\approx 0.02 - 0.08 eV$  (20 – 80 meV) per formula unit [119, 137, 138]. It is also agreed that at very high temperatures the compound is found mostly in the high spin phase. In the intermediary region - magnetic ordering, spin, phase, insulator to metal transitions take place, and it is somewhat agreed that they influence each other.

At the ground state the low spin  $LaCoO_3$  is a diamagnetic insulator. With an asymptotic Curie temperature of -200 K and a Neel temperature of 80 K ( $\approx -193^\circ C$ ) [139]. So a intermediate/high spin  $LaCoO_3$  would have an AFM ground state. This is confirmed with a PBE+U calculation as can be seen in table 4.9. This is contrary to computational literature which implies that FM is the ground state magnetic ordering [96, 109]. Magnetic states are investigated as within the collinear spin model VASP offers it is not possible to do paramagnetic materials. The FM spin structure was also converged as there is mounting evidence that  $LaCoO_3$  thin films, especially those deposited by PLD exhibit FM spin ordering below the critical temperature of  $\approx 80 K$  [140–143]. Which have been attributed to oxygen vacancy induced excess charge in Co cations [144].

The Co ion in  $LaCoO_3$  is nominally found in 3+ state with  $3d^6$  occupancy according to table 3.1. From here on out 3 possible spin states can be constructed as can be seen in figure 4.15. However cluster interaction calculations and XAS fits show that the Co ion experiences a ligand-hole behaviour. A table 4.16 from Saitoh et al. [145]. The table highlights that lower spin states have more ligand-hole like behaviour and also ligand-hole behaviour of higher order. The final ground state mixture given is 30%  $d^6$ , 50%  $3d^7 + \underline{L}$  and 20%  $3d^8 + \underline{L}^2$ . A similar result is presented by [146], thus it is safe to say that this material is very covalent in its ground state, and somewhat more ionic in its higher spin / excited state.

**Cubic structure oxidation state overview**

Atom	PBE+U			HSE06		
	Wigner-Seitz int.	Bader	Löwdin	Wigner-Seitz int.	Bader	Löwdin
La	2.56	2.15	1.31	2.65	2.25	1.36
Co	0.65	1.47	1.25	0.73	1.57	1.37
O	0.98	-1.21	-0.85	0.94	-1.27	-0.91

The oxidation states of cubic  $LaCoO_3$  can be found in 4.10. They show quite some variance between Bader and Löwdin analysis methods, with

$R\bar{3}c$ FM oxidation state overview				$R\bar{3}c$ AFM-G oxidation state overview		
PBE+U						
Atom	Wigner-Seitz int.	Bader	Löwdin	Wigner-Seitz int.	Bader	Löwdin
La	2.48	2.08	1.3	2.48	2.08	1.29
Co	0.83/0.9/0.95	1.47/1.60	1.33/1.55	0.92/1.01	1.63/1.66	1.51/1.53
O	0.99	-1.21	-0.9	0.74	-1.26	-0.94
HSE06						
La	2.65	2.19	1.37	2.58	2.15	1.35
Co	0.85/1.02	1.62/1.66	1.35/1.47	1/1.1	1.74/1.76	1.64/1.66
O	0.94	-1.28	-0.93	0.93	-1.29	-1

**Table 4.11:** The oxidation state results for  $R\bar{3}c$  for two magnetic orderings. For Co the results are partitioned, as for all methods (except the WZ integral method) charge ordering was exhibited.

the latter implying more covalency. For the cubic case the result is non-magnetic with no local spin moment, it was impossible to converge any other spin state for the cubic structure. The projected orbital occupancies are shown in figure 4.17, with the nonzero  $e_g$  occupancy signifying a covalent ligand-hole like state with 1.3 electrons more than the nominal occupancy.

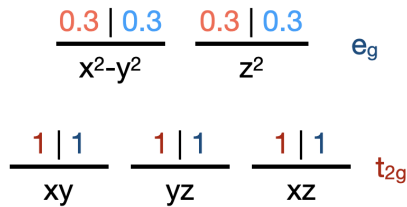


**Figure 4.17:** The projected Löwdin 3d orbital occupancies of the Co in the cubic structure. The PBE+U and HSE06 results are the same.

In contrast to the cubic structure the  $R\bar{3}c$  appears to be magnetic in all situations, and it is not possible to converge a non magnetic solution. The  $R\bar{3}c$  structure was converged with FM and AFM-G magnetic orderings.

In table 4.11 the oxidation states of the  $R\bar{3}c$   $LaCoO_3$  ions can be seen. What is notable here is the charge ordering among Co, next to that, the oxidation states on the Co in the  $R\bar{3}c$  structure seem to be higher than for the cubic case. The charge ordering is significantly more pronounced in the FM case. This is somewhat contrary to experimental literature, where, as mentioned before, the idea of charge disproportionation in  $LaCoO_3$  is considered false.

$R\bar{3}c$ Magnetisation $\mu_B$			
Ferromagnetic	Total	Co - W-Z	Co - Löwdin
PBE+U	2.47	2.1 / 2.3 / 3	2 / 2.2 / 2.9
HSE06	1	0.1/1.9	0.1/2.0
AFM-G			
PBE+U	0.0	2.97	2.93
HSE06	0.0	3	3.1

**Table 4.12:** The local Co magnetisation results for  $R\bar{3}c$  for two magnetic orderings. The total magnetisation is given per formula unit.

In table 4.12 the magnetisation for the two spin orderings can be seen. In a way it mirrors the oxidation states in ordering, where the FM state sees a significant ordering and in this case the AFM-G case sees no ordering. In the FM case the higher local magnetic moment is correlated with higher oxidation state of Co as expected from figure 4.16 pointing to higher spin states being less covalent.

What is more interesting is that the FM solutions seems to point to a mix of intermediate and high spin Co solution for the PBE+U case and a mix

of intermediate and low spin solution for the FM case. While the AFM-G always points to a high spin Co solution.

In both cases the high magnetisation is near  $3 \mu_B$  which is not something we expect from the nominal  $3d^6$  occupancy spin states found in figure 4.15, but it matches the values reported in DFT literature [96, 97, 109]. The reason for this abnormal magnetism is the ligand-hole like behaviour discussed previously. To compare the "high" and "Low" spins select orbital projected occupancies are plotted in figure 4.18.

**Figure 4.18:** The resultant projected Löwdin occupancies of the Co 3d band for  $R\bar{3}c$  structure calculated with PBE+U. Left is the "higer" spin result from the AFM-G ordered structure and on the right is the "lower" spin result from the FM ordered structure. The HSE06 data for Co magnetisation of 2 and  $3 \mu_B$  is similar, the non magnetic Co orbital occupancies are similar to the cubic structure.

AFM-G			FM - Low		
$1 \mid 0.8$	$1 \mid 0.4$		$1 \mid 0.9$	$0.9 \mid 0.3$	
$x^2-y^2$	$z^2$		$x^2-y^2$	$z^2$	
$1 \mid 0.3$	$1 \mid 0.2$	$1 \mid 0.3$	$0.8 \mid 0.3$	$1 \mid 0.2$	$1 \mid 1$
xy	yz	xz	xy	yz	xz

The figure 4.18 shows the effect of symmetry breaking. The Jahn-Teller distortions have lowered the  $x^2 - y^2$  orbital in energy for the compressed octahedra and in the same vain the stretched Co-O octahedra has a lower energy  $z^2$  orbital. It has to be noted that due to the Jahn-Teller distortions the point group symmetry of Co is no longer the octahedral  $O_h$  but rather the tetragonal  $D_{4h}$ . The  $x^2 - y^2$  and  $z^2$  still should be higher than the other 3d orbitals, but the degeneracies are lifted [147].

[147]: Wang et al. (2019), *Low-energy orbital excitations in strained LaCoO<sub>3</sub> films*

The observation from figure 4.18 is that in all cases the Co spin ordering is high spin, the difference between low and high magnetic moment of Co depends on the covalency (ligand hole like behaviour), with higher magnetisation solutions having a larger magnetic moment simply because they are more covalent and have more electrons, thus less unpaired spins. The only real low spin solution is for the non-magnetic Co atoms in the HSE06 FM solution whose orbital occupancy is similar to that of the Cubic solution.

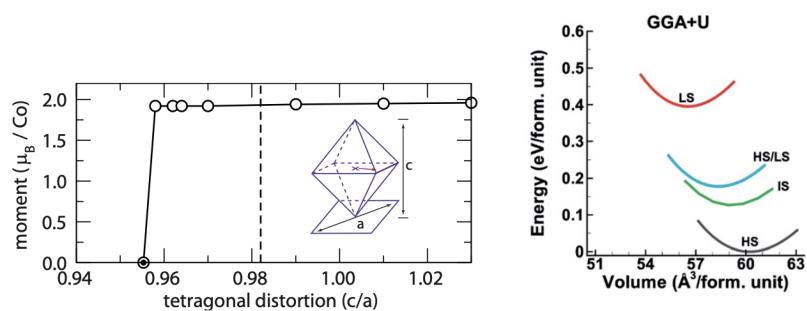
In both cases the oxidation state, spin state, magnetic moment and octahedra size are related. As mentioned before the found structure of  $LaCoO_3$  exhibits ordering in octahedra size characterised by small and large Co-O distance. In this case it is observed that larger octahedra have less charge (larger oxidation state) and therefore have a larger magnetic moment. This is seen in figure 4.18 as the lower magnetisation solution has 0.4 electrons more compared to the high spin solution.

### Some remarks on the spin state representation of $LaCoO_3$

These results complicate the situation quite a lot - between two structures and two magnetic orderings we have obtained very different results

On a computational level these results agree with the the literature out there. Besides the distortion + ligand hole argument Rondinelli proposes exotic vibrational mode exchange as a reason for why the AFM-G results show lower magnetisation than a completely high spin predicted solution [96].

And there are more computational details to discuss:



(a) Rondinelli et al. highlights that even a slight tetragonal distortion leads to a substantial increase in magnetic moment. [96]

(b) Ritzmann et al. shows that if a GGA+U formalism is used then the spin state one obtains is very volume dependent. [97]

**Figure 4.19:** Some computational considerations regarding representation from computational literature.

There are also two other things to talk about displayed in figure 4.19, it appears that the magnetic moments are very much influenced by structure and volume, and this is reflected in our results. The simple cubic cell has no tetragonal distortion and has a volume of  $55.5 \text{ \AA}^3$  per f.u., and the larger  $R\bar{3}c$  cell has tetragonal distortions and an approximate volume of  $61.3 \text{ \AA}^3$  per formula unit. So it is hard to say what is the exact ground state in this case.

On the experimental side similar discourse arises. Jonker and van Santen [111] have measured  $\text{LaCoO}_3$  to largely only have a spin contribution to the magnetic moments, and the reported magnetic moment is at least 70 % spin only moment. Similar (even smaller) orbital contribution has been measured by [138] [81]. This means that Spin is predominantly responsible for magnetism. Thus the spin and the resultant magnetisation obtained here should be representative of the measured one.

There are many papers which disprove the idea that an Intermediate spin phase exists at large [110, 138, 148, 149], highlighting that its existence is simply a product of averaging and its state evolves in a non unitary fashion. [150]

On the other hand Thornton [102], [106] and [151] imply IS spin state due to the ligand hole nature of Co here. Moreover newer results from Kobayashi et al. [152] and Klie et al. [153] see mostly a Low-Intermediate spin transition at intermediary temperatures.

So to conclude this, it seems that this material is very complicated in nature, however DFT does not fully fail here. On the contrary even simple U corrected GGA functional appears to reproduce the very covalent nature of this material, provided that you indeed take into account the symmetry breaking features as discussed in Chapter 3.

[150]: K řápek et al. (2012), *Spin state transition and covalent bonding in  $\text{LaCoO}_3$*

[151]: Medarde et al. (2006), *Low-temperature spin-state transition in  $\text{LaCoO}_3$  investigated using resonant x-ray absorption at the Co K edge*

[152]: Kobayashi et al. (2005), *Inelastic neutron scattering study of phonons and magnetic excitations in  $\text{LaCoO}_3$*

[153]: Klie et al. (2007), *Direct Measurement of the Low-Temperature Spin-State Transition in  $\text{LaCoO}_3$*

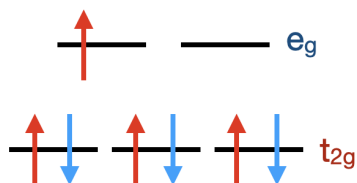


**Figure 4.20:** A schematic representation of the expected Ni low spin state in  $LaNiO_3$  from measurements and electron occupancy from table 3.1.

**Table 4.13:** The ground state magnetic ordering appears to be FM. Computed with PBE+U for  $R\bar{3}c$ , energy is given as difference to ground state in meV per formula unit. The same calculation for the cubic structure can be found in the appendix.

Mag. Type	$\Delta$ [meV per f.u.]
FM	0
Ferrimagnetic	24

**Table 4.14:** The oxidation states of the constituent ions of  $LaNiO_3$ .

### 4.2.3 $LaNiO_3$ Valence and magnetism

$LaNiO_3$  is a metallic compound exhibiting Pauli paramagnetism down to the lowest temperature it has been measured [116], there are reports of an AFM ordering and a Neel transition at  $\approx 157K$  [80, 118], but since this not widely reported and thought to come from oxygen vacancies and their ordering the AFM state is not investigated separately and the calculations are run in a FM manner.

FM is confirmed as the lowest energy magnetic ordering for the  $R\bar{3}c$  structure of  $LaNiO_3$ , all the other initiated orderings converged to Ferrimagnetic ones. The data is displayed in table 4.13. It has to be noted that the Ferrimagnetic ordering is very close in energy to the FM ordering, when compared to the energy distance between the lowest and next lowest orderings for  $LaFeO_3$  and  $LaCoO_3$ . It is also expected that this metallic material, with states crossing the Fermi level, would fulfil the stoner criterion ( $UD(\epsilon_F) > 1$ ), and thus be Ferromagnetic in out case.

The Ni ion in  $LaNiO_3$  is nominally found in the  $3+ (3d^7)$  state, despite this many XAS fittings [154, 155] report  $3d^8 + \underline{L}$  like behaviour, with weights 70%  $3d^7$  and 30%  $3d^8 + \underline{L}$  suggested by [156].

In spite of these fittings indirect measurements of the Ni-O complex report a magnetic moment of  $0.91 \mu_B$  [117] and neutron diffraction experiments report a magnetic moment of  $1 \mu_B$  [156]. These reported local magnetic moments are in line with a predictable low-spin state with  $3d^7$  occupancy as seen in figure. 4.20

The oxidation states of all the ions in  $LaNiO_3$  can be found in table 4.14. The HSE06 oxidation states higher both structures and all atoms. For both functionals the  $R\bar{3}c$  structure Co has a higher Bader oxidation state and a lower Löwdin oxidation state when compared to the Cubic structure. This is a sign that in this distorted  $R\bar{3}c$  structure the bonding is more ionic when compared to the cubic structure.

Cubic structure oxidation state overview				$R\bar{3}c$ oxidation state overview		
PBE+U						
Atom	Wigner-Seitz int.	Bader	Löwdin	Wigner-Seitz int.	Bader	Löwdin
La	2.59	2.15	1.24	2.49	2.10	1.3
Ni	0.65	1.4	1.33	0.78	1.44	1.26
O	1.01	-1.19	-0.86	1.01	-1.18	-0.85
HSE06						
La	2.68	2.26	1.4	2.57	2.2	1.37
Ni	0.72	1.47	1.41	0.86	1.57	1.39
O	0.96	-1.24	-0.93	0.97	-1.26	-0.92

The local magnetic moments for Ni in the various structures can be found in 4.15. It is clear to see that HSE06 calculations provide a more  $3d^8 + L$  like magnetic moment irrespective of structure. One thing to note here is that the structure was converged in an FM state, as evident by the total magnetisation.

Magnetisation $\mu_B$			
Cubic	Total	Ni - W-Z	Ni - Löwdin
PBE+U	0.96	0.98	0.95
HSE06	1.00	1.21	1.23
$R\bar{3}c$			
PBE+U	Total	Ni - W-Z	Ni - Löwdin
PBE+U	1	0.98	0.96
HSE06	1.00	1.23	1.25

**Table 4.15:** The total and Ni local magnetic moments of  $LaNiO_3$ , for all the functional and structure permutations. Total magnetisation is given per formula unit.

Another view on the covalency is the Ni 3d spin ordering from the orbital projections, as can be seen in 4.21.

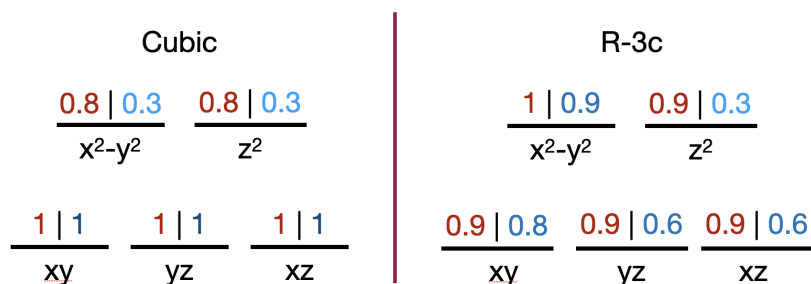


**Figure 4.21:** PBE+U resultant projected Löwdin orbital occupancies of the Ni 3d states. HSE06 delivered results that are qualitatively equal, only showing a lower order of covalency as expected per oxidation states.

In figure 4.21 the cubic result is as one would expect from a covalent low spin configuration. The orthorhombic result however shows the symmetry breaking that accompanies the distortions lowering the  $e_g x^2 - y^2$  down in energy.

Combining the results seen in tables 4.14 4.15 and figure 4.21, it is easy to say that the cubic structure calculated with PBE+U here provides a better representation of the covalent nature of the material and provides magnetisation that matches the experimental one.



### 4.3 Density of states and comparison to PES

Here we will examine the DoS near  $E_f$  and compare it to PES results, as it is known that the KS eigenvalues can be interpreted as approximate Ionisation potentials [157].

[157]: Chong et al. (2002), *Interpretation of the Kohn-Sham orbital energies as approximate vertical ionization potentials*

This will allow us to further evaluate our computational results, especially when looking the state structure near  $E_f$ . Even though it is not completely proven that the results obtained with local functionals are always interpretable as having physical relevance, it is proven that in cases where the the systems do not suffer from large self interaction errors the physical interpretability is strong [158]. It has to be noted that it is unknown if the materials at hand suffer from such errors, but it is assumed not to be so.

[159]: Koethe (2006), *Bulk sensitive Photoelectron Spectroscopy of strongly correlated transition metal oxides*

If possible, different spectra are used to highlight differences and interpretations as it is known that the spectra themselves depend not only on the absorption cross sections but also the state of the sample, its surface and even the angle of incidence of the incoming high energy photons.[159] The spectra themselves are scaled for best representation as needed, as the spectroscopic spectra are arbitrary in their intensity scaling.

[160]: Almladh et al. (1985), *Exact results for the charge and spin densities, exchange-correlation potentials, and density-functional eigenvalues*

The DoS are "negated" and aligned with the rising edge of the spectra as dictated by the ionization potential (IP) theorem [160]<sup>2</sup>:

2: This is very similar to Koopmans' theorem which is formulated for Hartree-Fock [161]

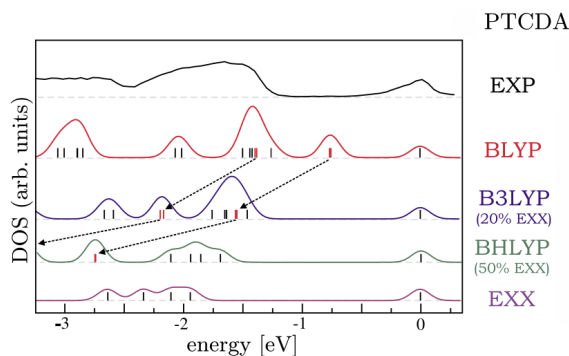
**Theorem 4.3.1** *The IP theorem of the Kohn-Sham density functional theory states that the energy of the highest occupied molecular orbital (HOMO)  $\epsilon_{HOMO}$  equals the negative of the first ionization potential.*

[162]: Körzdörfer et al. (2010), *Single-particle and quasiparticle interpretation of Kohn-Sham and generalized Kohn-Sham eigenvalues for hybrid functionals*

The spectra are also stretched to fit most of the features, even though this might initially seem like *data manipulation*, it is not so and it has been proven to have merit. T. Körzdörfer and S. Kümmel showed that for systems where self-interaction error does not distort the spectrum too much then the stretching of KS spectra "provide for computationally cheap alternatives to numerically costly many-body perturbation theory in the GW approximation." [162].

It has to be noted that this shift is not always constant as can be seen in fig. 4.22. The DoS here are stretched to better represent the near  $E_f$  states and therefore the stretching might prove lacking at lower energies further away from the Fermi level.

**Figure 4.22:** An example of this semi-linear stretching behaviour by [162]. Here a spectrum of a biomolecule (PTCDA) is compared to GGA results (BLYP) and Hybrid functional results. It is notable that this stretch is *generally*





### 4.3.1 $LaFeO_3$ DoS and PES

#### DoS

A range of optical band gaps has been measured with a range of 2.12-2.65 eV [127, 163] for powder material, with it being shown that the band gap is particle size dependent (larger particle - smaller gap) [127]. A more in depth computational + Tauc analysis by Scafetta et al. [164] obtained a band gap of 2.34 eV for epitaxial films of around 15-36 nm in height, this is taken as a better representation of the bandgap of the bulk material.

[164]: Scafetta et al. (2014), *Band structure and optical transitions in  $LaFeO_3$ : theory and experiment*

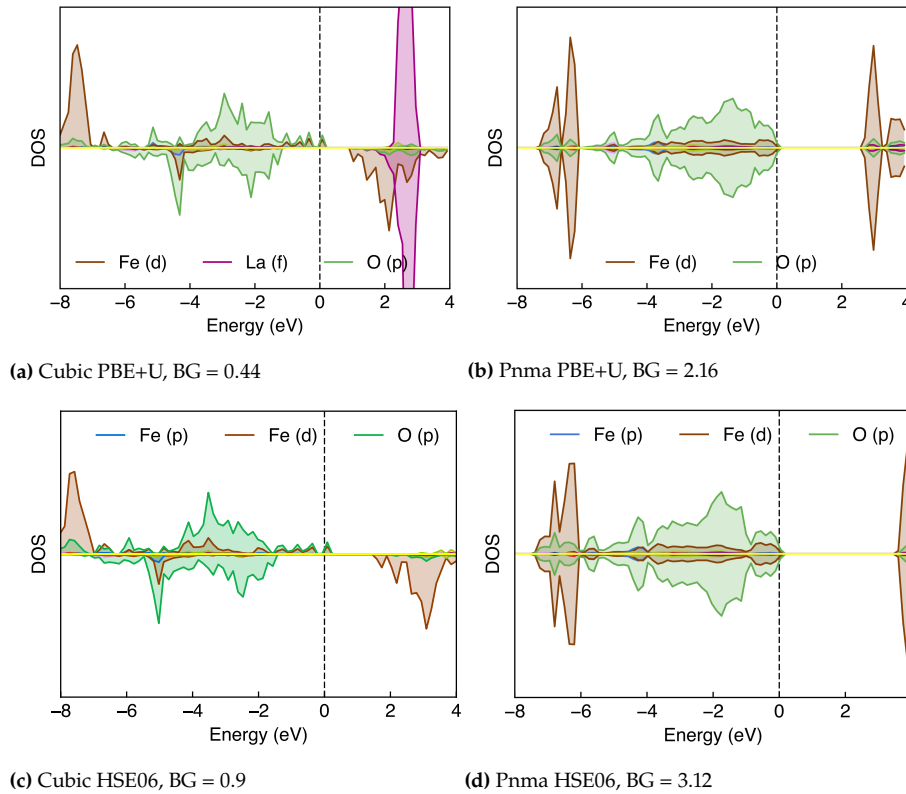


**Figure 4.23:** The DoS plots of  $LaFeO_3$  for various functionals and structures. The  $Pnma$  results are presented for the ground state magnetic ordering AFM-G, the reason the  $Pnma$  plots look symmetric in spin is because the average DoS is plotted here.

In figure 4.23 the DoS plots for the various  $LaFeO_3$  configurations are shown. The cubic structures appear to be half-metals and the bandgap reported is the one directly above it, surprisingly HSE06 overpredicted the gap in the  $Pnma$  structure while PBE+U is within experimental range. The cubic structures under-represent the gap severely. In all cases  $LaFeO_3$  is a charge transfer insulator as predicted, if one excludes the small contribution of the Fe-d band just below  $E_f$ . The most notable thing is that the DoS seem to be functionally equal between functionals but not structures, if one excludes the erroneous La-f band contribution in the first picture. Another issue is that the cubic structures show a small number of states crossing the Fermi level, so the bandgap reported is the one above these erroneous states.

#### PES

There are some studies presenting PES data of epitaxied  $LaFeO_3$  thin films [165, 166]. Even though the latter one was produced at a higher

[165]: Wadati et al. (2005), *Hole-doping-induced changes in the electronic structure of  $\text{La}_{1-x}\text{Sr}_x\text{FeO}_3$ : Soft x-ray photoemission and absorption study of epitaxial thin films*

energy range, the earlier one is of higher quality and provides more detail near  $E_f$  so it will be used for comparison with DoS [165].

The comparison of PES spectra to the DoS of the various structures can be found in 4.24. The Y axis is an arbitrary scale, and the x axis is the PES binding energy. The DoS are overlaid and matched to the rising edge of spectra.

The spectra shows three prominent peaks in the near  $E_f$  spectra and a small satellite after the main part. The middle of the three peaks is wider than the other two peaks of the near  $E_f$  spectra.

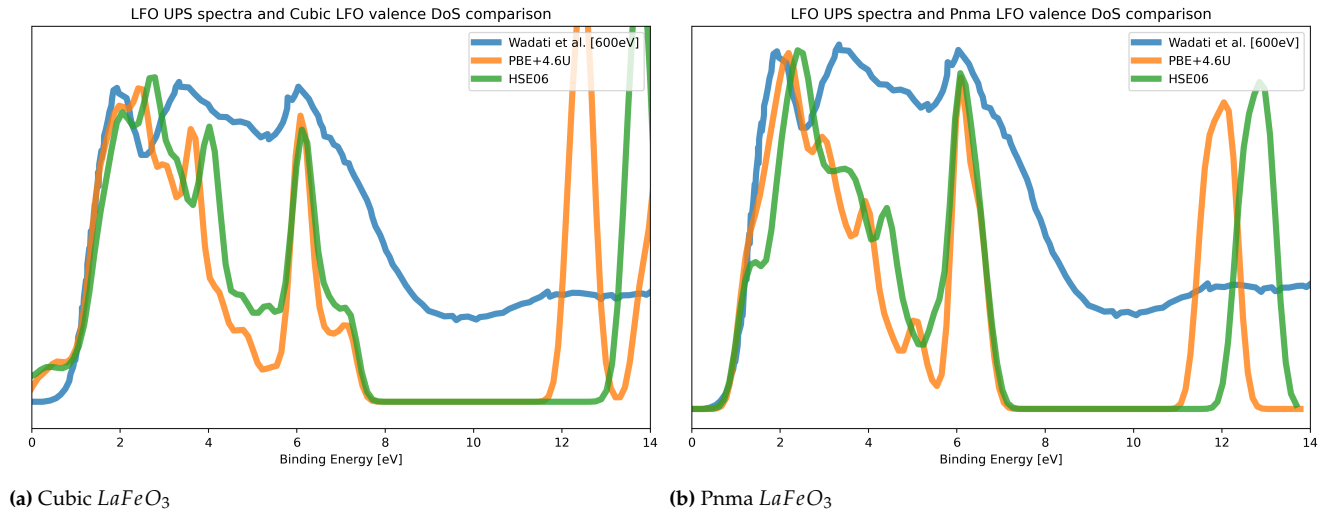


Figure 4.24: Valence band DoS comparison to PES results from Wadati et al. [165].

On the in figure 4.24a the DoS results of the cubic structure are laid over the measured spectra. There it is noticeable that both functionals exhibit a pre-peak which comes from the erroneous vanishing DoS at  $E_f$  discussed before. Both DoS are functionally very similar with the PBE+U producing a better satellite location at higher binding energies, and a more accurate location of the first and second peaks.

In 4.24(b) the same comparison is made, but now with the  $Pnma$  structure DoS. Here the HSE06 results produce an anomalous pre-peak not found in the spectra here nor in the newer spectra not shown here [166]. PBE+U again produces a better satellite peak location and a sharper onset peak more closely matching the PES spectra compared to the HSE06 result. It has to be said that the  $Pnma$  structure does not manage to produce the "shoulder" seen in the spectrum at 7-8 eV at the end of the third peak.

In terms of the bandgap the  $Pnma$  structure calculated with PBE+U provides the best result.

However the Cubic structure calculated with the same functional provides a better mid-spectra fit reproducing the middle peak much better. The cubic structure does under represent the bandgap, and shows a weirdly metallic behaviour and places the La-f states too low in the conduction band. Besides that it provides a surprisingly good computational representation of  $\text{LaFeO}_3$ .

### 4.3.2 $\text{LaCoO}_3$ DoS and PES

#### DoS

An x ray absorption gap has been measured at 0.9 eV by [148], and 0.6 by UPS and BIS spectroscopy [167] and optical absorption [163].

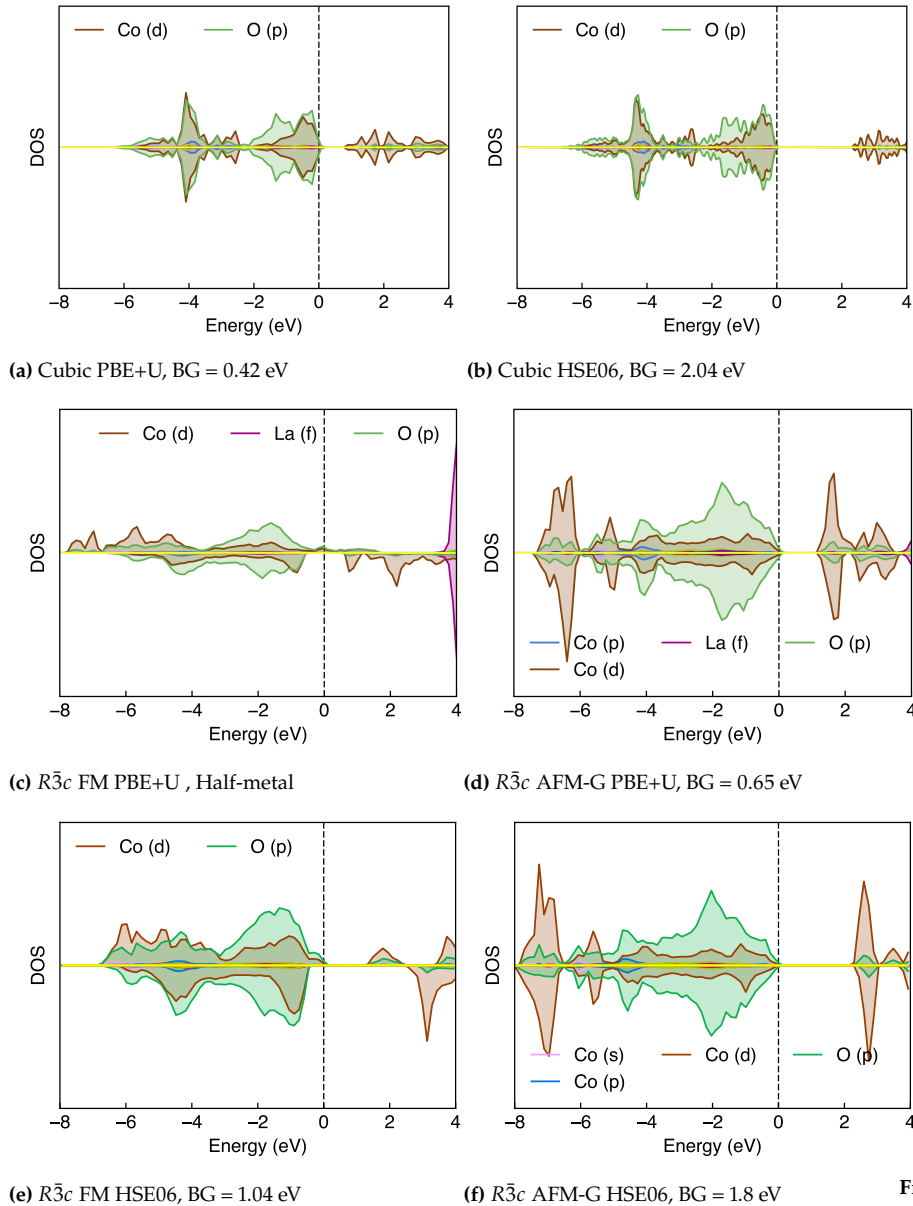


**Figure 4.25:** The DoS plots of LCO for various functionals and structures.

The DoS of all the differing structures and magnetic orderings can be seen in figure 4.25. Surprisingly the cubic structure has an acceptable band gap of 0.42 eV for PBE+U compared to the 2.04 eV of the HSE06 result which is an over-prediction roughly doubling the experimental value.

For the  $R\bar{3}c$  structure calculated with PBE+U the FM ordering produces a half-metal, which is a strange result knowing that this ordering is the one measured in thin films. The AFM-G results calculated with PBE+U provides a band gap which exactly matches known measurements so this

is spot on. The AFM-G ordering also reproduces more of the expected charge transfer insulator character expected of this material with more separation between the O2p and TM3d bands compared to the other DoS.

The HSE06 result for the  $R\bar{3}c$  structure with the AFM-G ordering is functionally similar to the PBE+U result, just with a larger band gap. The FM ordering result now has a bandgap that is close to the experimental one (1.04 eV), while the locations of the states are functionally similar to the PBE+U solution.

## PES

[145]: Saitoh et al. (1997), *Electronic structure and temperature-induced paramagnetism in  $\text{LaCoO}_3$*

[159]: Koethe (2006), *Bulk sensitive Photoelectron Spectroscopy of strongly correlated transition metal oxides*

There is a multitude of spectra available [145, 159, 168], but a select of these will be used. Of them a large spectroscopy study by Saitoh et al. [145], which was done over a large energy range. And newer work from T.C. Koethe, who worked on eliminating errors in  $\text{LaCoO}_3$  PES measurement by negating surface effects, incidence angle and energy thus producing clear spectra with a selection of multiple of photon energies of up to 6 keV [159].

The work by Saitoh et al. will be used first as it covers a larger energy range. This will allow the comparison of states further away from the Fermi level. The spectra is characterised by two main parts - the near  $E_f$  part, consisting of a pre-peak and a flat-band, and the higher binding energy part consisting of three peaks in descending intensity. This is displayed in figure 4.26.

The HSE06 results for the  $R\bar{3}c$  structure are not plotted, as these results were converged very late in the process of writing this thesis.

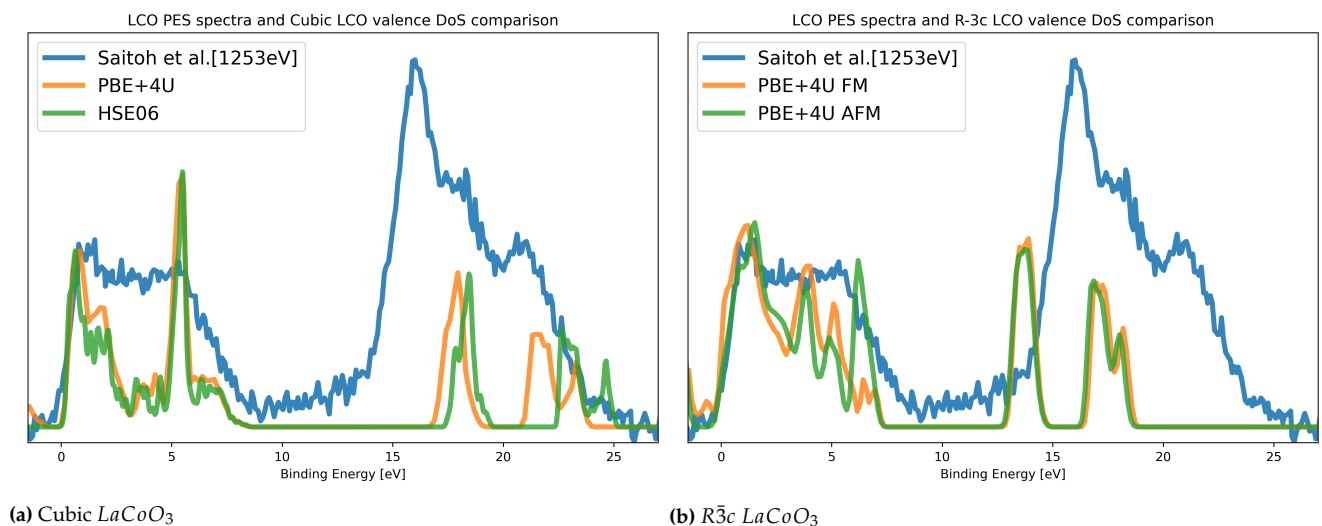


**Figure 4.26:** Valence band DoS comparison of  $\text{LaCoO}_3$  to PES results from Saitoh et al. [145], PBE+U and HSE for the Cubic structure and PBE+U FM and AFM-G for the  $R\bar{3}c$  structure. The PES results have their background subtracted in the paper already.

In figure 4.26 the comparison of DoS to PES is made. As mentioned in the before the stretching is non linear, and in this case the states are stretched to match the near section of the PES spectra.

It is clear to see that the  $R\bar{3}c$  structure provides good correspondence to the spectra especially reproducing the flat-band behaviour of the near  $E_f$  part and the placing the states of the far part closer together akin to the PES spectra.

The cubic structure results are largely the same across the two functionals, proving that the added computational cost of HSE06 is a hindrance without merit in this example. Both functionals do not reproduce the flat-band like behaviour of the near  $E_f$  spectra.

To have a closer look at the near valence spectra the DoS is again compared to another PES spectra. This time with the high energy spectra from [159] measured at roughly 6 keV.

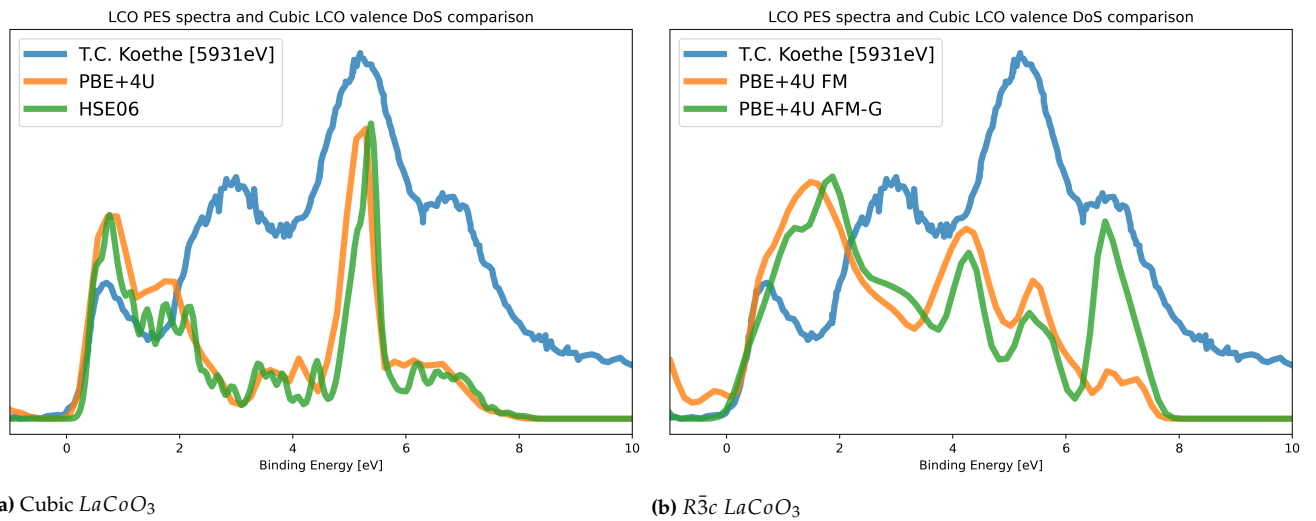


**Figure 4.27:** Valence band DoS comparison of  $LaCoO_3$  to PES results from the thesis of T.C. Koethe [159], PBE+U and HSE for the Cubic structure and PBE+U FM and AFM-G for the  $R\bar{3}c$  structure.

The comparison to the high energy PES spectra from Koethe are visible in figure 4.27. The spectrum is characterised by four, almost equidistant, distinct peaks of different height, with the second to last peak being the highest.

Here it is easy to see that the  $R\bar{3}c$  structure produces the 4 characteristic peaks measured. On the other hand the cubic structure result provides broader, smaller peaks contrasted by the very sharp main peak (second to last) similar to the spectra, thus it is hard to tell if the four peak structure is recovered here.

As we don't know the cross sections of each of these states or the *joint densities of state*, its hard to say which one of them is better.

As for the approaches of each structure, the PBE+U result for the cubic structure arguably provides a better result, if one interprets the second peak in the DoS as corresponding to the second peak in the PES spectra, and the the last peak in the PES spectra as the shoulder to the main in the DoS then one can recover correspondence.

$R\bar{3}c$  AFM-G approach produces four clear, distinct peaks, compared to the FM approach where the peaks are less distinct. In both cases the first three peaks are not in their expected locations. But due to the increased peak distinction the  $R\bar{3}c$  AFM-G approach is considered the best.

All in all it seems that  $LaCoO_3$  is a very complicated material and its representation does gain a lot from added complexities such as symmetry breaking distortions and specific spin orderings. If possible the more complex structures and representations should be used.

### 4.3.3 $\text{LaNiO}_3$ DoS and PES

#### DoS

The DoS of all the structural and functional configurations are plotted in figure 4.28. This material is expected to have a metallic behaviour with few states at the Fermi level. All of the provided DoS reproduce these aspects except for the fact that they are found to be half metals. It is not clear if the material is a half-metal in real life but similar results are found in computational literature [169, 170].

Qualitatively the HSE06 results have a larger substantially larger gap for the minority spin channel, and a large bulk of the Ni 3d states are found further away from the Fermi level.

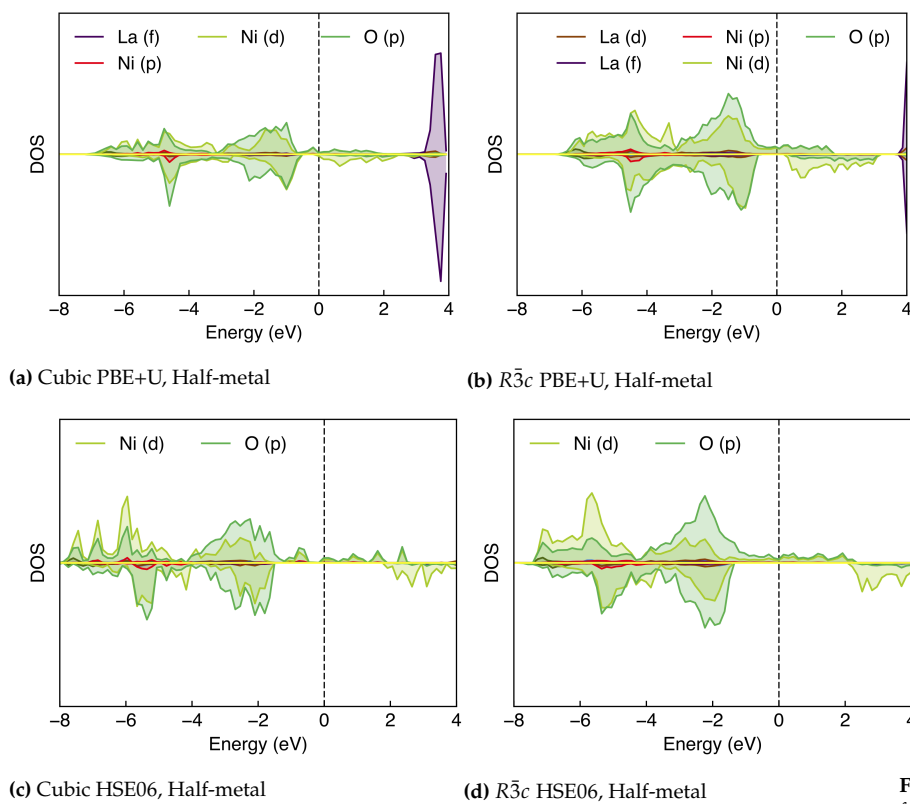


**Figure 4.28:** The DoS plots of  $\text{LaNiO}_3$  for various functionals and structures.

#### PES

There are many lower energy PES spectra available for  $\text{LaNiO}_3$  with 21.1 eV He1 line results from Barman et al [171] and Kemp and Cox [172], but as will be shown later the cross-sections of the constituent materials at this energy is such that very little detail can be discerned.

Barman et al. does provide a higher energy 1253.3 eV Magnesium X-ray line measurements but those seem to be not that detailed when compared to a much newer spectrum at 800 eV from Horiba et al. [173].<sup>3</sup> The preferable cross-sections and accurate measurement makes the Horiba et al. spectrum the spectrum of choice for this comparison.

[173]: Horiba et al. (2007), *Electronic structure of  $\text{LaNiO}_{3-x}$ : An in situ soft x-ray photoemission and absorption study*

3: The Horiba et al. spectrum provides a markable resolution of 0.2 eV, they also provide a close up spectrum near the  $E_f$  with a resolution of only 0.07 eV.

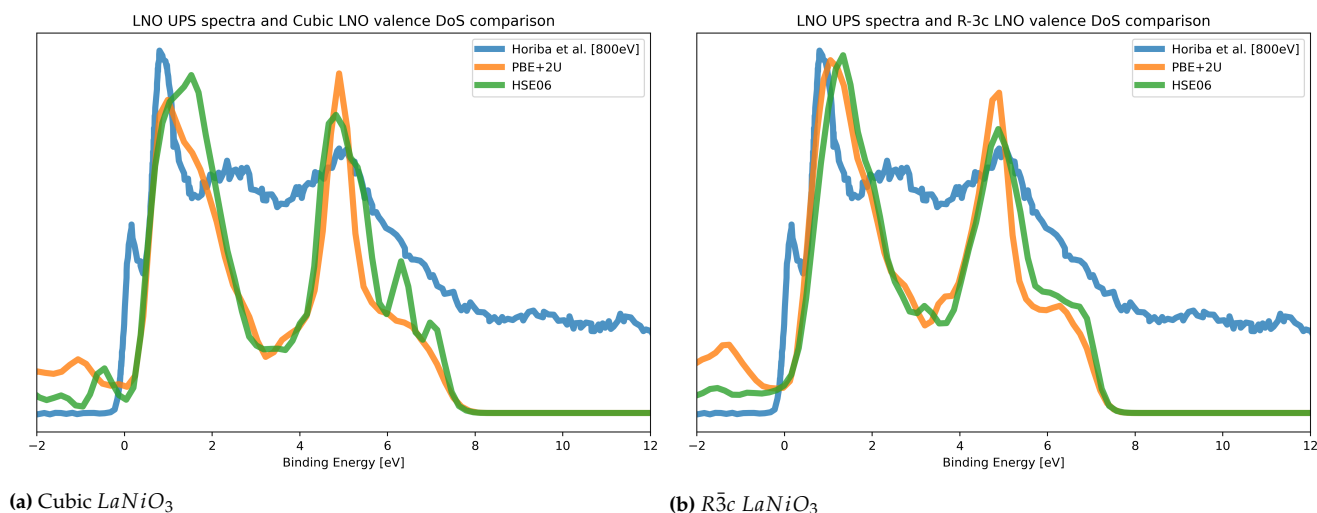


Figure 4.29: Large energy comparison with existing PES spectra from [173].

In figure 4.29 the comparison between the PES spectra of Horiba et al [173] and the DoS is shown. The spectrum is characterised by a sharp pre-peak near the Fermi level followed by the most prominent peak of the spectra. After that two smaller peaks of equal height are found. A thing to note is that the small pre-peak in the Horiba et al. measurement is not present in the 1253.3 eV measurement by Barman et al. This is strange as the absorption cross-sections should be very similar between 1253.3 eV and 800 eV. In the paper Horiba et al. attribute this small pre-peak to 3d  $e_g$  orbitals.

Nevertheless the comparisons seen in figure 4.29 have some notable differences. To start with the pre-peak, the small peaks seen in both of the cubic spectra and the PBE+U result of the  $R\bar{3}c$  structure are indeed projected to be mostly of  $d^{x^2-y^2}$  character, thus belonging to the  $e_g$  irreducible representation (group of orbitals with the same symmetry). In the DoS this peak is often at  $E_f$  and has more distance to the  $t_{2g}$  peak that follows. One could shift the spectra more to the left to obtain a more visual correspondence but it is not done here.

[120]: Gou et al. (2011), *Lattice normal modes and electronic properties of the correlated metal LaNiO<sub>3</sub>*

4: In said paper they do highlight that none of the functionals were able to reproduce the  $e_g$  pre-peak in the spectrum, and they reason that XC functionals cannot correctly capture this  $e_g$  peak. This work however disproves that, adding evidence to observations by a later study using an all-electron DFT code (Wien2k) showed that a GGA functional (PBEsol) easily reproduces all the characteristics of the PES spectra including the  $e_g$  onset peak [174].

[175]: Saloman et al. (1988), *X-ray attenuation cross sections for energies 100 eV to 100 keV and elements Z = 1 to Z = 92*

Further, all DoS present reproduce the most prominent peak and the last peak, with the Cubic structure HSE06 result showing erroneous peaks on the shoulder after the last main peak.

These findings are matching with previous findings by Gou et al. [120], which found that GGA functionals are better at reproducing this spectrum compared to Hybrid functionals, especially HSE (exact screening length not mentioned in the paper).<sup>4</sup>

The only disparity is the middle one of the three larger peaks which, upon first glance is not reproduced in any of the DoS. Initially this might seem as a shortcoming of DFT but if you look at figure 4.28 you can see Ni 3d peaks in all of them right in the middle of the two larger peaks (often covered by O2p states). It also happens that at 800 eV the absorption cross section of Nickel is  $\approx 2 - 3$  times higher than that of Oxygen [175], so we are in essence probing mostly Nickel states with this spectroscopic measurement.



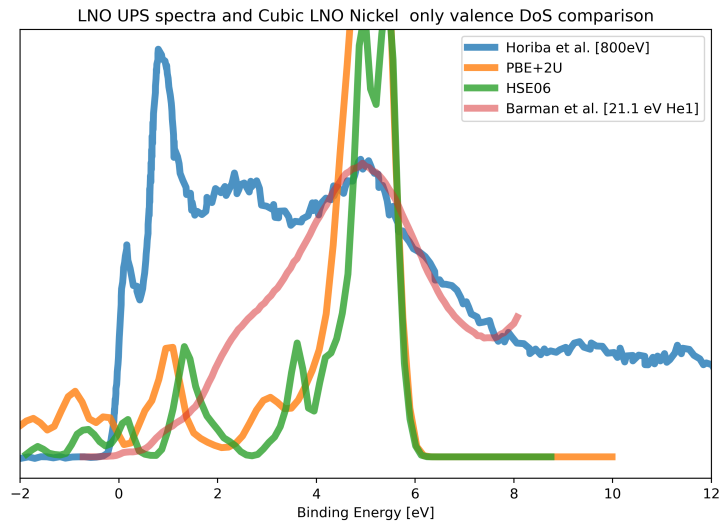


**Figure 4.30:** Ni only DoS of the cubic LNO structure, with the addition of the Barman He1 line spectra. [171]

In figure 4.30 the Ni only DoS of the cubic structures is plotted against the spectra highlighting that both functionals reproduce the middle peak with the PBE+U result being in a more favourable location. The disparity in height is explainable by the fact that we are not only probing the valence DoS but rather the *joint densities of state* as per *Fermi's golden rule*, meaning that it could be that in the core region there are few states in this very transition range.

To highlight the impact that the indecent photon energy has on the relative intensities of the peaks; the Barman et al. He1 spectrum is plotted in red. At this energy the cross sectional difference between the ions and the joint DoS is such that the last peak located at 5-6 eV in the DoS is the most prominent structure seen in the measured spectra. The middle peak is identifiable as a right hand side shoulder of the He1 spectra, with the pre-peak and the most prominent peak of the Horiba et al. spectrum not visible.

## 4.4 Conclusions

Overall it seems that the choice of structure and magnetic ordering is very important for these materials. For almost all cases the TM oxidation state of the distorted structures was higher than that of the highly symmetric cubic ones. Moreover  $LaCoO_3$  results showed that for the same structure as simple change in magnetic ordering can drastically change the DoS and introduce a bandgap. A more favourable conclusion is the fact that in many cases PBE+U is just as good if not better at reproducing experimental PES spectra as long as the structural and magnetic symmetries were broken. This means that representing the ground state magnetic ordering and structural distortions is more important than the functional choice.



# Bulk contact charge transfer investigation

# 5

Now that baseline for the bulk structures is established, it is logical to follow with a *bulk contact scenario*. Here the bulk contact is defined as the interface between two bulk materials where any surface is far away from the interface of the two constituent materials. An illustration can be seen in figure 5.1.

The charge transfer hypothesis of Zhong and Hansmann [15] does not specify any constraints on the contact itself, thus it is assumed to work across *any* interface as long as the band alignment conditions discussed in Chapter 3 are met.

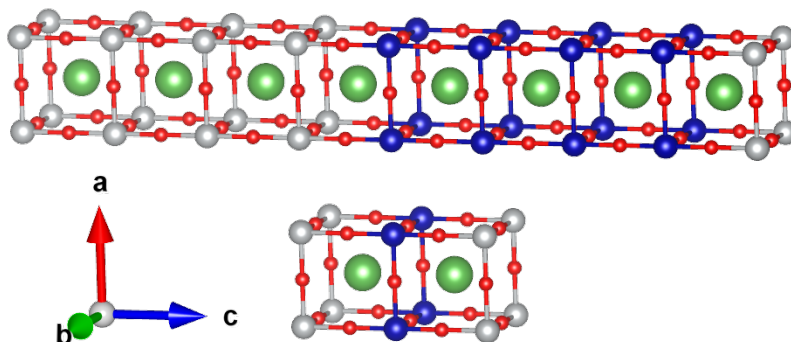
Bulk contact arises as a natural choice of test framework as the initial calculations of Zhong and Hansmann were done on bulk unit cells, moreover in a bulk contact the only new variable introduced is the interface itself; making it easier to test the hypothesis [15].

An important thing to disclose is that these results were largely produced before the conclusions of Chapter 4 were made, so many conclusions and remarks about the materials and their modelling are not taken into account here. Nevertheless, the results presented in this Chapter should be viewed in the context of Chapter 4, especially with regard to the differences caused by structure, magnetic ordering and functional choice.

## 5.1 Structure and convergence

Last chapter it was shown that these materials have different lattice parameters even in their simple cubic forms. An assumption is made - that if these materials make contact and remain crystalline and faultless, then their in plane lattice parameters would be the average of the two.

To simplify the problem of matching planes, cubic unit cells are used. Since it is a bulk material the structure used is one unit cell in size in the a and b directions and thickness is defined as the extent in the c direction. Examples of such structures can be seen in figure 5.2 *The exact details pertaining to the structure construction and other convergence tests made can be found in the Appendix.*



5.1	Structure and convergence	59
5.1.1	<i>LaNiO<sub>3</sub>-LaCoO<sub>3</sub></i> structure convergence	60
5.1.2	<i>LaNiO<sub>3</sub>-LaFeO<sub>3</sub></i> structure convergence	61
5.2	Relaxation and Charge results for the bulk contact structures	64
5.2.1	Relaxation results	64
5.2.2	Charge results	66
5.3	Conclusion	70

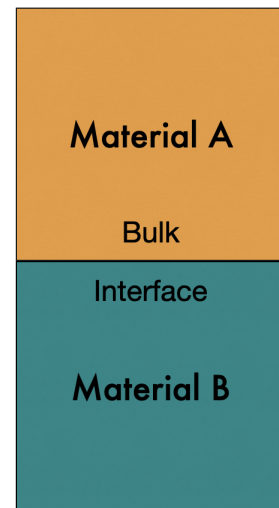


Figure 5.1: A schematic of a *bulk* material interface. The surfaces of the constituent materials are assumed to be very far away.

Figure 5.2: LNO-LCO interfacial structures, only the 1+1 and 4+4 structures are shown. The Co atoms are blue and Ni atoms are gray. The Ni atoms on the other end of the structure are there only because of the periodic representation of the cell, and are not actually part of the computational structure.

1: One of the reasons one has to converge thickness is the periodic plane wave representation of the materials, meaning that the interface would interact with its images on both sides of the material. Moreover the finite size of the structures can be a limitation to finding the true ground state of the materials.

Here the interfacial structure thickness convergence results are shown. This is done because the properties of these materials both in bulk and at the interface are different for different thicknesses, and the goal is to find a structure where the properties of the materials are not susceptible to changes in thickness; i.e. are converged.<sup>1</sup>

Another reason to find a converged structure is time and computational resources. Later structural relaxations and computational investigations of these large cells are computationally costly and time intensive even with modern computational facilities, so they can be done on a limited set of structures.

### 5.1.1 $LaNiO_3$ - $LaCoO_3$ structure convergence

Here the convergence data is shown in figure 5.3. The magnetisation shown is the total difference between spin up and spin down densities of the whole cell divided by the total number of unit cells present in the material. The energy is the total free energy of the structure divided by the number of unit cells.

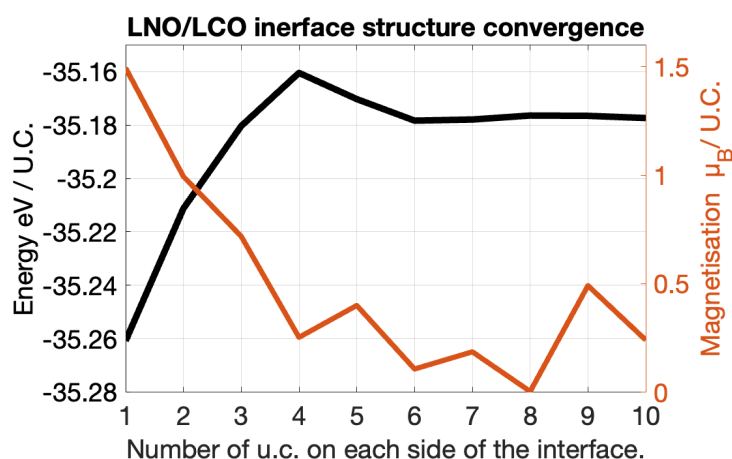


**Figure 5.3:** The total magnetisation and energy per unit cell of the  $LaCoO_3$  and  $LaNiO_3$  interfacial structure as a function of the number of unit cells on each side of the interface.

The energy data shows us that convergence is achieved with 4-6 unit cells of material on each side of the interface. As the the energy per unit cell does not change significantly with addition of more cells

The high total magnetisation per unit cell seen in the range of 1-2 unit cells on each side of the interface in figure 5.3 can be attributed to the fact that up two 2+2 unit cells in size, the local magnetic moment of Co near the interface is  $\approx 2\mu_B$ , with the magnetic moment decaying further from the surface. After 3+3 unit cells the magnetic moment of all the Co atoms is quenched to zero signalling convergence. To visualise this the Wigner-Seitz integral magnetic moments are shown in figure 5.4. In figure 5.4b the increased magnetisation of Co in  $LaCoO_3$  at the interface can be seen, this increased magnetisation is subsequently quenched fully when the system is extended to 4 unit cells.

From this observation we can conclude that it is not octahedral stretching and increase in unit cell volume that are solely responsible for the

magnetic behaviour of Co in  $LaCoO_3$ , unlike suggested by figures 4.19 a and b.

As seen in figure 5.4a the  $LaNiO_3$  does exhibit a strange AFM-Ferrimagnetic ordering, with sometimes entering a more FM like state. From this image we can conclude that this ordering is the steady state ordering of  $LaNiO_3$  in this structure. And figure 5.4b it appears the the interfacial local magnetic moment of Ni is  $1 \mu_B$  with 4 and 5 unit cell thickness results being the exception.

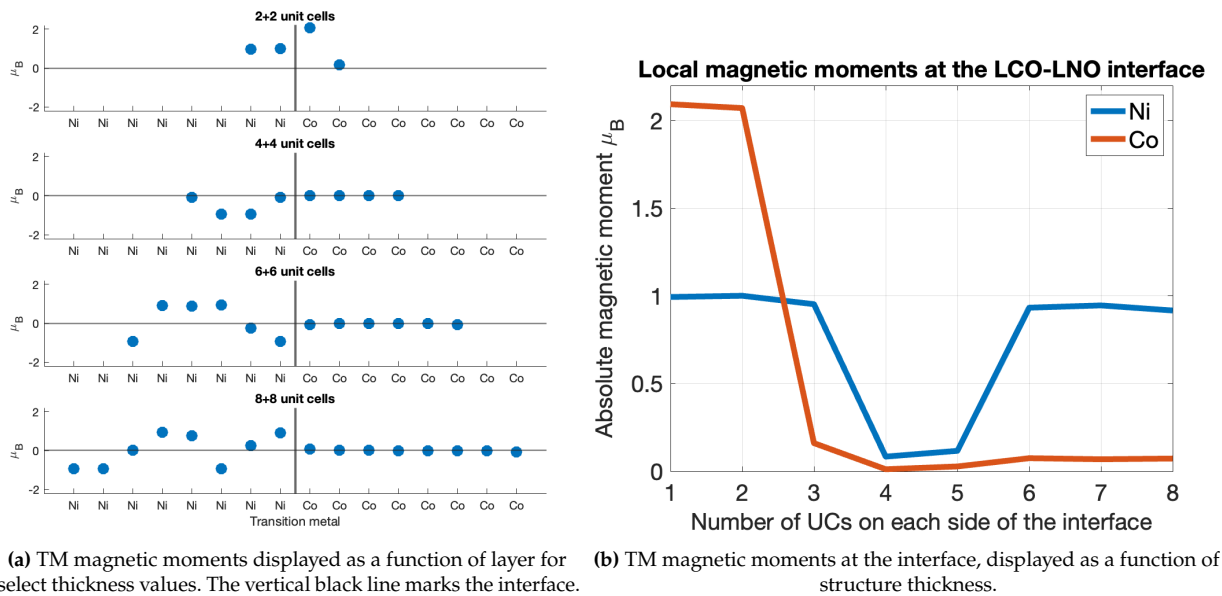


Figure 5.4: Local Wigner-Seitz integral magnetic moment convergence graphs for the  $LaNiO_3$ - $LaCoO_3$  structures.

To conclude, the energy convergence results point to convergence at a minimum of 4 unit cells thickness. The Co reaches magnetic convergence from 4 unit cells thickness, but at 4-5 unit cells thickness the local magnetic moment of Ni at the interface is low, and the normal magnetisation is resumed from 6 unit cells thickness. Therefore the 6+6 unit cell thick structure is chosen.

### 5.1.2 $LaNiO_3$ - $LaFeO_3$ structure convergence

The convergence results are shown in figure 5.5. The magnetisation and energy are defined the same as before.

In terms of energy it seems that convergence is reached from 4 unit cells on each side of the interface and onwards.

Here a magnetic ordering representation problem arises. As shown in Chapter 4 the preferred magnetic ordering for  $LaFeO_3$  is AFM-G but the only anti ferromagnetic ordering properly representable with this structure is AFM-A, which was shown to be much higher in energy, even higher than Ferromagnetic ordering (see table 4.7 in Ch. 4). This means that FM is the expected ordering of  $LaFeO_3$  in this structure.

This representation problem manifests in two ways - the constant change of magnetic ordering seen in figure 5.6a, and the fact that the local

magnetic moment of Fe has been reduced to  $\approx 1 \mu_B$  from the  $\approx 4.2 \mu_B$  seen in all the reference structures shown in table 4.8 in Ch. 4.

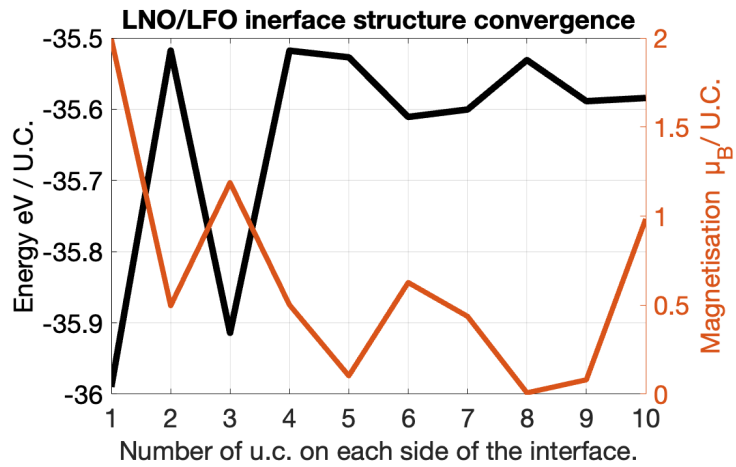
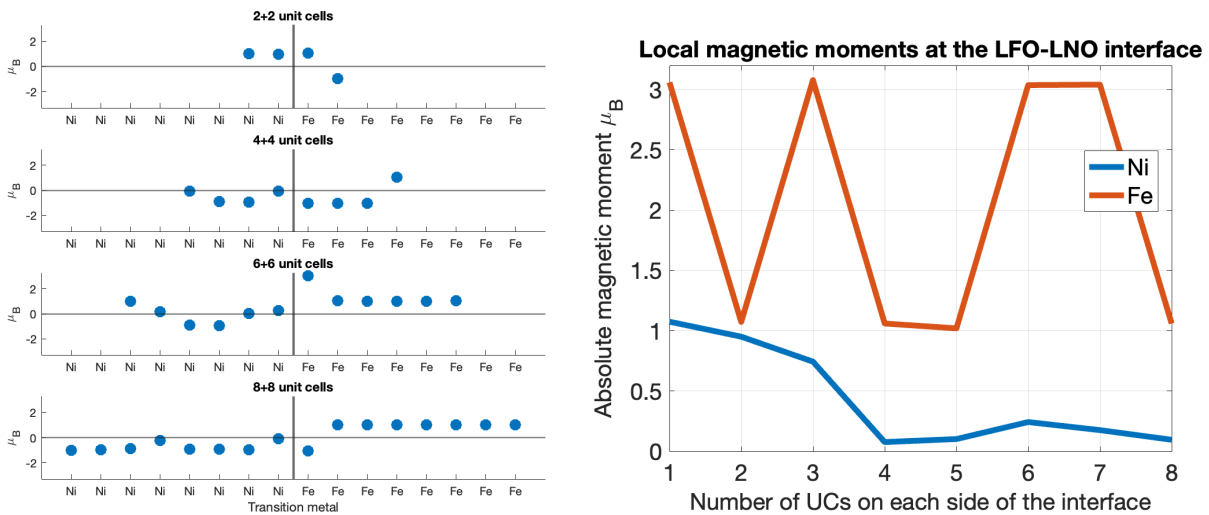


**Figure 5.5:** The total magnetisation and energy per unit cell of the  $LaFeO_3$  and  $LaNiO_3$  interfacial structure as a function of the number of unit cells on each side of the interface.

The increased magnetisation of the 1,3,6 and 7 unit cell thick structures seen in figure 5.5 can be explained by the fact that the local magnetic moment of Fe at the interface is  $\approx 3 \mu_B$  as can be seen in figure 5.6b. What is notable is that the magnetisation of the Fe ion at the interface is often of a different sign than the "bulk" like ferromagnetic section of  $LaFeO_3$  as seen in figure 5.6a.



**(a)** TM local W-Z integral magnetic moments displayed as a function of layer for select thickness values. The vertical black line marks the interface.

**(b)** TM local W-Z integral magnetic moments at the interface, displayed as a function of structure thickness.

**Figure 5.6:** Local W-Z integral magnetic moment convergence graphs for the  $LaNiO_3$ - $LaFeO_3$  structures.

As expected from the magnetic ordering convergence test seen in table 4.7 in Ch. 4, the magnetic ordering of Fe is largely FM with interfacial exceptions. When comparing the magnetic ordering of Ni of the previous structure in figure 5.4a and the current structure seen in figure 5.6a, it seems that for small structures the ordering is similar but for larger structures the ordering here is FM. This could again be caused by

the magnetic ordering representation problem in this structure as the ferromagnetism found in  $LaFeO_3$  could be interacting magnetically with  $LaNiO_3$  forcing FM ordering but of opposite majority spin. As a consequence the interfacial magnetic moments of Fe do not stabilise and the interfacial magnetic moments of Ni are quenched as can be seen in figure 5.6b.

As the interface magnetic moment and magnetic order convergence tests do not show clear convergence, it is assumed that the ferrimagnetic like ordering of Ni seen in the previous structure is representative. Coupled with the quenching of interfacial Ni magnetic moment seemingly being the preferred state this leaves the 6+6 structure as a reasonable choice for further investigation.

## 5.2 Relaxation and Charge results for the bulk contact structures

After the convergence tests the 6+6 cells were relaxed for both material combinations. The relaxation is done with symmetries disabled as mentioned in the introduction of this section, with the initialised magnetic orderings discussed in the Appendix.

In this section I will talk about the relaxation and charge results comparing both the relaxed and un-relaxed structures, and the relaxed structure charge results to the reference structure values seen in Ch.4.

### 5.2.1 Relaxation results

Firstly only the atomic positions in the structures were relaxed without allowing the cell volume to relax; these structures are referred to as "Position-only" structures. After that the volume of the structure was also relaxed to allow the cells to change the common in-plane lattice parameter, these structures are referred to as "Relaxed". The initial constrained structures that were not relaxed are referred to as "Non-relaxed" in this section.

#### *LaNiO<sub>3</sub>-LaCoO<sub>3</sub>* structure relaxation results

For this structure the relaxation did not result in a significant drift of atoms or large changes in structure. The first unit cell of *LaNiO<sub>3</sub>* above the interface did stretch, changing the *c* parameter of the cell from 3.84 Å to 3.842 Å. Meaning that the *LaNiO<sub>3</sub>* positions near the surface relaxed closer to it, while the next unit cell up relaxed away from the interface. This signifies a local interface driven enlargement of the unit cell.<sup>2</sup>

2: The change due to relaxation is so small that it cannot be visually identified if the structure is plotted. So plots were omitted.

The in plane lattice parameter changed from the assumed 3.826 Å to 3.818 Å. So the final lattice parameter is closer to the *LaCoO<sub>3</sub>* one. No changes in magnetic ordering or spin state were seen.

#### *LaNiO<sub>3</sub>-LaFeO<sub>3</sub>* structure relaxation results

Here in figure 5.7 we see that the Fe octahedra (Ochre colour) shrunk in the *c* direction quite substantially. This also lead to an expansion of the Ni octahedra (Gray colour) in *c* parameter near the interface. The shrinkage of the *LaFeO<sub>3</sub>* cells was largest in the centre of *LaFeO<sub>3</sub>* part of the structure, with a maximum reduction of the cells *c* parameter to 3.9 Å from the initial 4.1 Å *c* parameter..



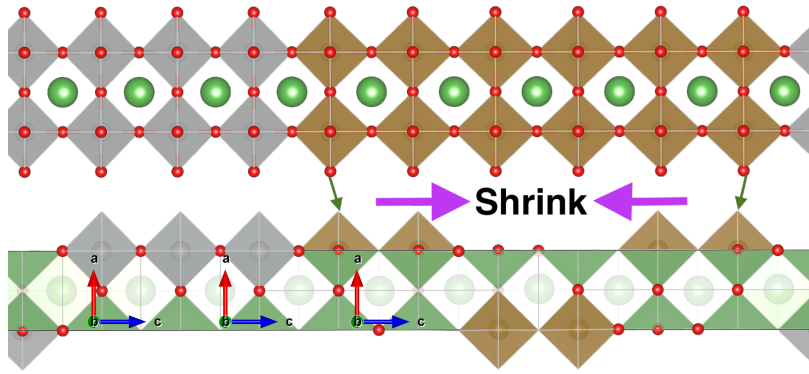


**Figure 5.7:**  $LaNiO_3-LaFeO_3$  interfacial structure relaxation changes illustrated. The top structure is the unrelaxed one and the bottom structure is the relaxed one. The Fe octahedra are ochre and the Ni octahedra are gray. The oxygen atoms are red and the lanthanum atoms are green. The arrows illustrate the  $LaFeO_3$  atom displacement during relaxation. The bottom image shows fewer octahedra because the atomic positions at the edge are no longer equivalent due to distortions so the visualisation software does not search for bonds for those atoms across the interface, the number of atoms has not changed.

When relaxing the in-plane lattice parameter, it did reduce substantially from the assumed  $3.89 \text{ \AA}$  to  $3.84 \text{ \AA}$ ; again in line with shrinking  $LaFeO_3$  cell volume.

The in plane lattice parameter of  $3.84 \text{ \AA}$ , and the shrunk out of plane parameter of  $3.9 \text{ \AA}$  give an average lattice parameter of  $3.86 \text{ \AA}$ . If we look back at figure 4.5a<sup>3</sup>, this change of lattice parameter places the  $LaFeO_3$  of this relaxed superstructure firmly in the FM false ground state. This is a seemingly logical consequence of the FM magnetic ordering - the structure is relaxing to accommodate the FM magnetic ordering.

3: The data in figure 4.5a is plotted in length units of  $r_{Bohr}$ ,  $3.86 \text{ \AA}$  is  $\approx 7.29 r_{Bohr}$

Despite this prediction the final structure relaxed to a different ordering for Fe, the final magnetic ordering of the structure is seemingly also ferrimagnetic. The simple reason for the emergence of this ordering is the contact. The comparison of TM local magnetisation before and after relaxation is shown in figure 5.8.

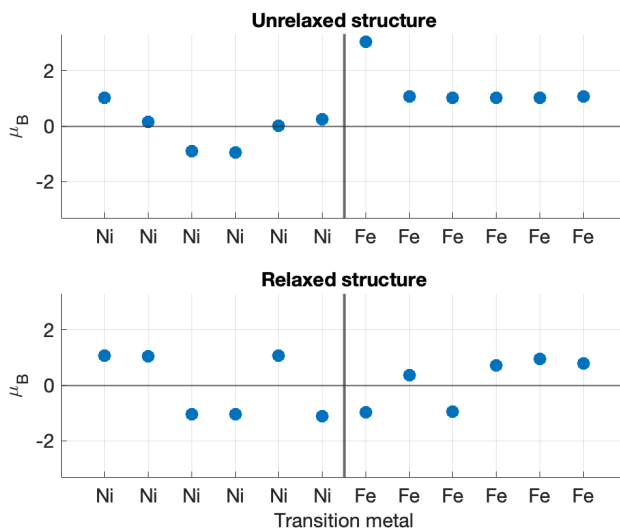


**Figure 5.8:**  $LaNiO_3-LaFeO_3$  interfacial structure relaxation changes of TM local magnetic moments illustrated.

This change in lattice parameters and magnetic ordering is attributed to the fact that AFM-G ordering cannot be reproduced, so the material shrinks to accommodate the next best magnetic ordering and spin state (low spin) in energy.

## 5.2.2 Charge results

Here the oxidation states of the transition metal ions in these superstructures is discussed. Since Löwdin projected charges are known to fail in purely ionic cases, and Bader charges to fail in covalent cases, both charge types are presented.

As it was found in the relaxation step, the  $LaFeO_3$  shrinks in volume to a degree where it is known to assume a false ground state as per figure 4.5a, the intermediary relaxation results are also included in the discussion. This is done for both superstructures.

### $LaNiO_3$ - $LaCoO_3$ interface charge

First we shall look at the difference in oxidation state from the Non-relaxed, the Position-only relaxed, and Relaxed structures as explained previously. These results are shown in figure 5.9.

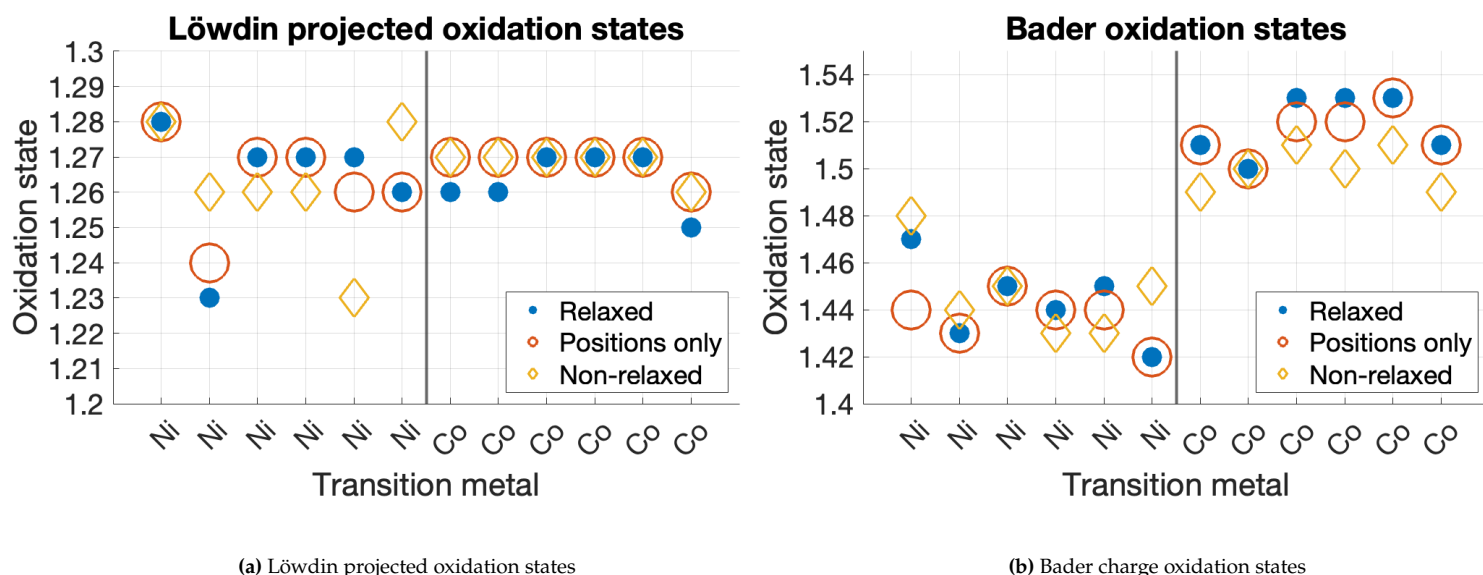


**Figure 5.9:**  $LaNiO_3$ - $LaCoO_3$  interfacial structure Löwdin projected and Bader Oxidation states. The oxidation states displayed are those of the transition metals, with the black line indicating the interface.

As can be seen in figure 5.9, the influence of relaxation is not large, in the case of Löwdin projected oxidation states the oxidation states at the interface were reduced for both materials. While the Bader oxidation states veered further apart at the interface with Ni oxidation state decreasing and Co oxidation state increasing. This signifies that the interface has become more Ionic as the Löwdin charges are not sensitive to small movements of charge in the interstitial space.

For the next comparison only the results of the relaxed structure will be used.

To place these results in context, the results of the relaxed structure are further compared to the results of the two two reference structures from Ch. 4 - Cubic cell reference and Experimental lattice parameter

cell reference ( $R\bar{3}c$  for both materials). These results are shown in figure 5.10.

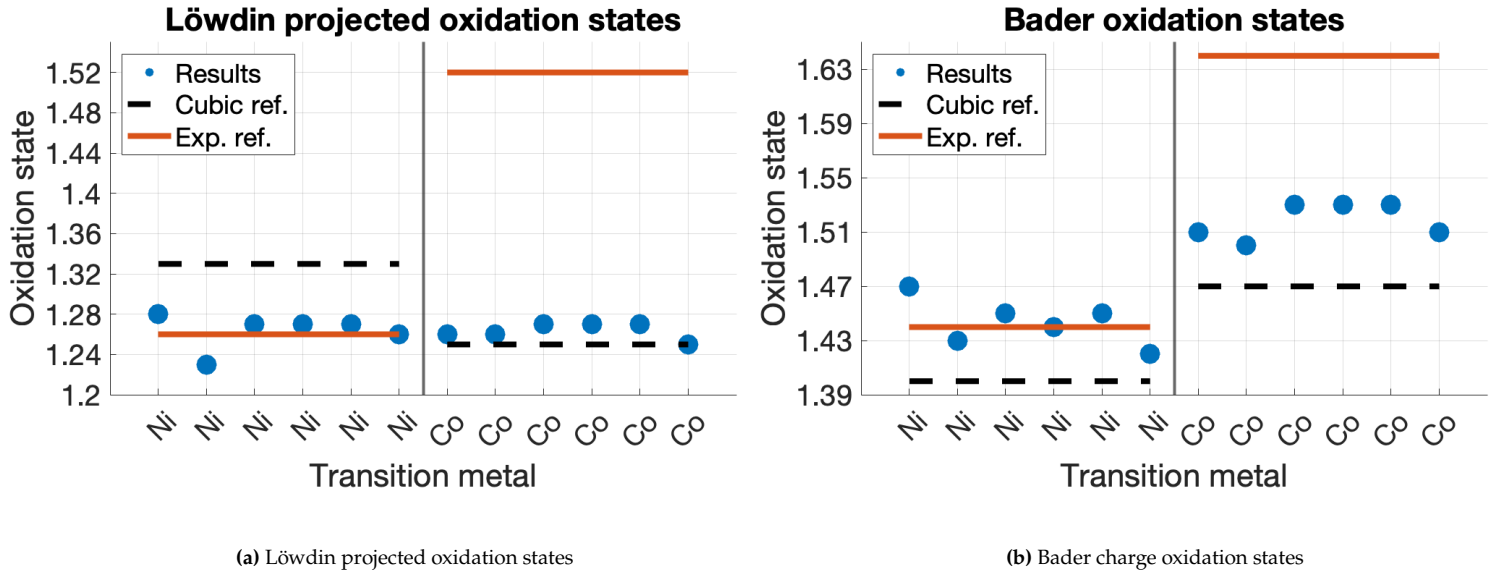


**Figure 5.10:**  $LaNiO_3$ - $LaNiO_3$  interfacial structure Löwdin projected and Bader oxidation state comparison with the oxidation states of the reference structures from Chapter 4. The cubic reference is one of the simple cubic cell, and the experimental lattice parameter structure reference is that of the distorted structure in its lowest energy magnetic ordering. In this case those are the results of the  $R\bar{3}c$  cells for each of the constituent materials.

Comparing the two sets of results in figure 5.10 it is clear to see that the Löwdin projected oxidation states do not show much change when approaching the interface, while Bader oxidation states do. In this case it could be understood as a decrease in covalency between the materials, as the Löwdin projection method would account for charge *shared*, while the Bader charge method would just decide to cut it along a boundary, granting more or less to one atom.

The 2nd and 6th Ni atoms from the left in both graphs converged to anomalously low local magnetic moments of 0.3 and 0.5 respectively, which are correlated with the lower-than-expected oxidation states. On the other hand the consistent increase in oxidation state of the first Ni atom does not correlate with increased local magnetic moment.

In both analysis cases the Ni oxidation states are much more like the ones in the distorted  $R\bar{3}c$  structure seen in Chapter 4, this can be attributed to the fact that the  $LaNiO_3$  *experimental lattice* structure is much less tilted and distorted compared to the  $LaCoO_3$ . Meaning that  $LaNiO_3$  in this structure is closer to its distorted state compared to  $LaCoO_3$  to its distorted state. Another reason for such difference is the added symmetry breaking of having a larger cell with more unit cells of  $LaNiO_3$ , as the distorted reference cells are always larger than the cubic ones in Ch. 4.

As for the Co ions, again, only Bader oxidation states show a significant difference compared to the reference structures. The Co oxidation state has increased slightly compared to the cubic reference structure result towards the *experimental* reference structure oxidation state by  $\approx 0.06 e^-$ .

As there is not much change in the Löwdin oxidation states in this structure. The Bader oxidation states can be examined for charge transfer.

If we consider Co and Ni ions close to the interface (marked by the vertical black line) and compare them to the "bulk like" ions further away from the interface, then there is a decrease in the Co oxidation state of  $\approx 0.03 e^-$  and a decrease of Ni oxidation state of  $\approx 0.03 e^-$ . While the decrease of oxidation state of Co is in line with the extended prediction of Zhong and Hansmann from Ch. 3 figure 3.1, the accompanied decrease of Ni oxidation state is not.

To conclude, the observed difference of Ni oxidation state across the structure can be attributed to symmetry breaking induced by the larger cell as well as the slight relaxation. The same can be concluded about the increase in average oxidation state of Co across the whole structure.

The observed oxidation state difference at the interface is rather small and does not follow the trend of TM donating electrons across the interface predicted by Zhong and Hansmann [15].

#### *LaNiO<sub>3</sub>-LaFeO<sub>3</sub>* interface charge

Just as before; first the difference in oxidation state from the Non-relaxed, the Position only relaxed, and Relaxed structures is discussed. The oxidation state results for the different structures are shown in figure 5.11.

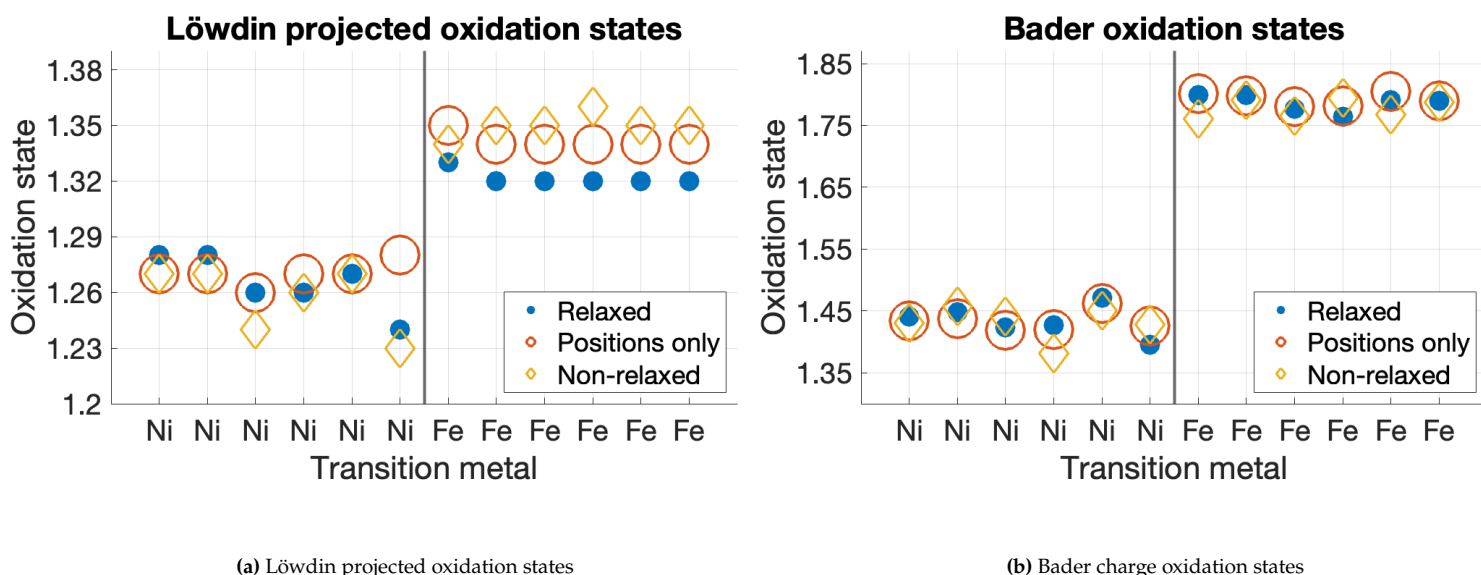


**Figure 5.11:** *LaNiO<sub>3</sub>-LaFeO<sub>3</sub>* interfacial structure Löwdin projected and Bader Oxidation states. The oxidation states displayed are those of the transition metals, with the black line indicating the interface.

For the Löwdin projected oxidation states seen in figure 5.11a both the Non-relaxed and Relaxed structures show a lower oxidation state for the Ni atom at the surface compared to the Position only result. This difference can be attributed to the fact that the Positions only relaxed structure

exhibits FM ordering for the Fe atoms compared to the ferrimagnetic ordering found in the other structures.

The general trend seems to be an increase in Ni oxidation states and a decrease for Fe oxidation states with relaxation. This trend is not seen with the Bader oxidation states seen in 5.11b.

To provide context, results of the relaxed structure are compared to the oxidation states of the reference structures for each constituent material in Ch. 4. This comparison is shown in figure 5.12.

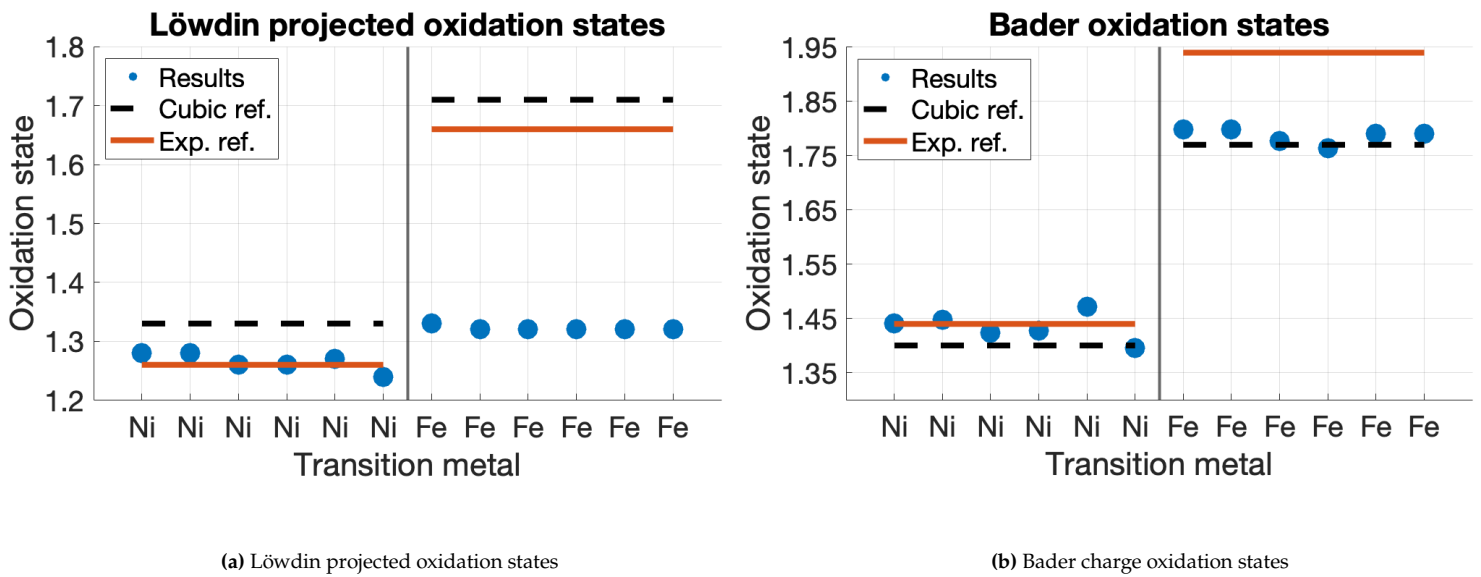


**Figure 5.12:**  $LaNiO_3-LaFeO_3$  interfacial structure Löwdin projected and Bader oxidation state comparison with the oxidation states of the reference structures from Chapter 4. The cubic reference is one of the simple cubic cell, and the experimental structure reference is that of the distorted structure in its lowest energy magnetic ordering. This is the  $R\bar{3}c$  cell for  $LaNiO_3$  and the  $Pnma$  cell for  $LaFeO_3$ .

In figure 5.12, the Ni oxidation states, for both Löwdin and Bader results, exhibit the same likeness to the *experimental* reference structure oxidation states, as seen in the previous ( $LaCoO_3 - LaNiO_3$ ) superstructure. Unlike before the lowering of the local magnetic moment of Ni is not correlated with the oxidation state.

For the Fe ions the Löwdin projected oxidation state differs drastically from the reference structures, while the Bader oxidation states are in line with the cubic reference structure oxidation states.

The observed significant difference in trends between the two charge analysis methods would signify an increase in covalency and orbital hybridisation as Fe ions now share more orbital overlap with other ions increasing the amount of charge shared in the interstitial space. This increase in covalency could be correlated with the observation that in all of these structures the local magnetic moment is  $\approx 1\mu_B$  compared to the reference structure magnetic moments of  $\approx 4.2\mu_B$  seen in table 4.8.

While this drastic lowering of Fe Löwdin oxidation state is in line with the expanded prediction of Zhong and Hansmann seen in Ch. 3 figure 3.1 these results are to be considered erroneous as the trend is not

dependant on the distance from the surface and could be attributed to the misrepresentation of the material in this structure.

If the Bader results are discussed then there is a small increase in oxidation state of Fe near the interface of  $\approx 0.02 e^-$  and a decrease in Ni oxidation state of  $\approx 0.04 e^-$ . This would mean that Fe donates electrons to Ni, which is inverse of the expanded prediction of Zhong and Hansmann seen in Ch. 3 figure 3.1.

In conclusion the results provided show inverse behaviour to that of the prediction of Zhong and Hansmann [15]. But these results are not to be considered definitive because of the representation problem of the constituent materials in this structure, and therefore a more complete structure should be evaluated for a definitive answer.

### 5.3 Conclusion

In both cases the observed change in oxidation state is inverse to that of the prediction of Zhong and Hansmann [15]. But these results are not very trustworthy as both  $LaNiO_3$  and  $LaFeO_3$  are not represented correctly in these structures and exhibit weird and unexpected magnetic and charge behaviours. Moreover it seems that due to the representation issues the changes seem to be relaxation driven, at least in the case of the  $LaNiO_3-LaFeO_3$  superstructure.

# Experimental structure charge transfer investigation

# 6

In experimental situations the heterostructures are deposited on top of matching (often other perovskite) substrates. In this case, one is interested in  $LaCoO_3$  and  $LaFeO_3$  as catalysts, therefore it is logical to place them on the surface in an ultra-thin layer such that any short-range charge transfer improvements to OER are at their largest where the reaction takes place. This assumes that the reaction takes place *on* the surface and not *in* it.[176].

Real life bulk materials -  $LaCoO_3$  and  $LaFeO_3$  are insulators, while  $LaNiO_3$  is a conductor. To have small resistance path the bulk is also chosen to be a conductor, and the  $LaNiO_3$  layer is thick to ensure minimal bulk tilt influence and coupling.<sup>1</sup>

Here the substrate is taken to be Niobium doped Strontium titanate - Nb:STO ( $Nb : SrTiO_3$ ) bulk substrate. Which is an often used, and readily available conducting bulk perovskite substrate, with a lattice parameter that is similar to the lattice parameters of our superstructure perovskites.

It has to be disclaimed that these results were produced before the conclusions of Chapter 4 were made, so the results of this chapter are presented *as is*. The results are discussed in the light of the conclusions of Chapter 4 however and should be viewed in that context.

## 6.1 Examining epitaxy on a bulk material

Here I will talk about the assumptions made when considering the material stack and epitaxy. A schematic of the experimental structure is seen in fig. 6.1, it must be said that the 25 unit cell deep layer of  $LaNiO_3$  is a structure of size that is far above the size limitations afforded to me by the hardware at hand, so this section is about the choices made in choosing a structure that is representative.

As this chapter will encompass thin films on known substrates, more regard will be given to experimental literature as to help result interpretation. Computational details and considerations are found in the Appendix.

From experimental observations by Ellen Kiens, it is known that all individual perovskites and heterostructures are fully strained to the substrate in-plane lattice parameter at all thicknesses considered in the experiments and simulation. Therefore, possible thickness-dependent strain relaxation of the epitaxial thin films is ignored and all films are fixed to the substrate in-plane lattice parameter in the simulations discussed below.

6.1 Examining epitaxy on a bulk material . . . . .	71
6.1.1 STO - $SrTiO_3$ . . . . .	72
6.1.2 Impact of epitaxy on $LaNiO_3$ . . . . .	72
6.1.3 Impact of epitaxy on $LaFeO_3$ . . . . .	73
6.1.4 Impact of epitaxy on $LaCoO_3$ . . . . .	73
6.2 Slab convergence and relaxation . . . . .	74
6.2.1 Converging vacuum and slab thickness . . . . .	74
6.2.2 Slabs and relaxation . . . . .	75
6.3 Magnetic and Charge results . . . . .	79
6.3.1 $LaNiO_3$ - $LaCoO_3$ slab results . . . . .	79
6.3.2 $LaNiO_3$ - $LaFeO_3$ slab results . . . . .	83
6.4 Conclusions and orbital occupancy . . . . .	86

1: The electrical contact is not always made through the bulk.

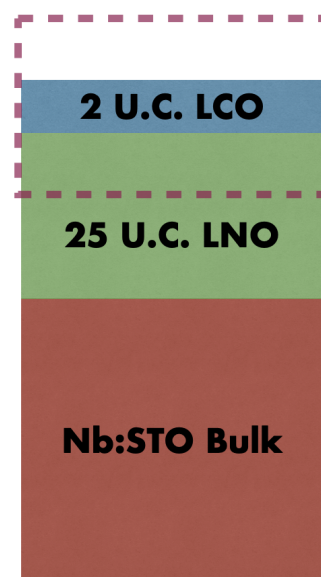


Figure 6.1: The experimental layer stack investigated. The dashed line marks the actual extend of the computational structure.



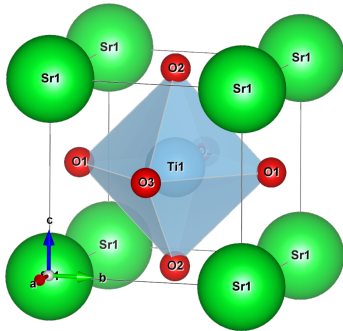


Figure 6.2: The cubic structure of STO

While the Zhong and Hansmann prediction would include charge transfer between  $LaNiO_3$  and  $SrTiO_3$ . The layer stack of 25 unit cells of  $LaNiO_3$  is roughly 10 nm thick. This means that any substantial charge transfer effects that could be expected of the  $LaNiO_3 - SrTiO_3$  interface are mellowed out by sheer distance and not considered.

[178]: Rondinelli et al. (2011), *Structure and Properties of Functional Oxide Thin Films: Insights From Electronic-Structure Calculations*

[179]: McBride et al. (2015), *Effects of biaxial stress and layer thickness on octahedral tilts in  $LaNiO_3$*

[180]: Fowlie et al. (2019), *Thickness-Dependent Perovskite Octahedral Distortions at Heterointerfaces*

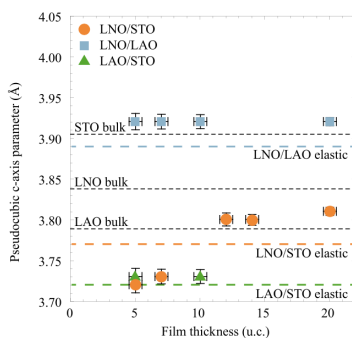


Figure 6.3: Measured c axis parameters for various material and substrate combinations from Fowlie et al. [180]

### 6.1.1 STO - $SrTiO_3$

Strontium titanate  $SrTiO_3$  is a prototypical perovskite with a perfect cubic structure (seen in fig. 6.2) and a relatively average lattice parameter, which allows for various other perovskites to be grown on top of it without much issues.

In this particular situation the  $SrTiO_3$  is doped with Niobium.  $SrTiO_3$  by itself is an insulator with an indirect bandgap of 3.2 eV [177], so Niobium is added to enhance conduction. The doping is so low that it does not influence the lattice parameter and physical structure of the material.

The experimental lattice parameter of  $SrTiO_3$  is 3.905 Å. Thus it is the lattice parameter that the heterostructure is going to be constrained to in-plane, as the growth is considered to be on top of the  $SrTiO_3$  (001) plane. The parameter itself is much larger than those of  $LaCoO_3$  (3.82 Å) and  $LaNiO_3$  (3.84 Å) cubic structures but smaller than that of the  $LaFeO_3$  (3.927 Å) cubic structure. This means strain distortion effects are expected.

### 6.1.2 Impact of epitaxy on $LaNiO_3$

Here we start off by examining the first step in the epitaxy -  $LaNiO_3$  on  $SrTiO_3$ . In this structure the  $LaNiO_3$  layer would be under tensile strain as its lattice parameter is substantially smaller than that of  $SrTiO_3$ . If the  $LaNiO_3$  is fully constrained to the lattice of  $SrTiO_3$  it should exhibit  $\approx +1.7\%$  strain.

In a 2011 study Rondinelli and Spaldin [178] highlighted that once grown on a substrate  $LaNiO_3$  lowers symmetry to tetragonal and engages in interfacial connectivity of the octahedra, changing its tilt pattern.

$LaNiO_3$ , when positively strained onto an  $SrTiO_3$  substrate, has a glazer tilt pattern of  $a^-a^-c^-$  compared to the free crystal having  $a^-a^-a^-$ . A computational study by McBride et al.[179] found the tilts to be  $6^\circ$ ,  $6^\circ$  and  $2^\circ$  degrees respectively. This tilt structure of  $LaNiO_3$  on  $SrTiO_3$  has been experimentally verified by Fowlie et al., and the tilts were measured to be  $9^\circ$ ,  $9^\circ$ ,  $0^\circ$  at a height of 20 unit cells [180]. The  $9^\circ$  tilts are not much larger than the experimental findings ( $8.29^\circ$ ) of  $LaNiO_3$  tilts of the free crystal, discussed in Ch. 4, thus only tilts in one direction are changed by epitaxy.

What the computational study of McBride et al. [179] also found was that within 4 monolayers of  $LaNiO_3$  deposited on  $SrTiO_3$  the out of plane lattice parameter  $c$  was almost equal to the normal bulk lattice parameter of  $LaNiO_3$ . The experimental findings of Fowlie et al. [180] seen in figure 6.3 indicate that  $LaNiO_3$  deposited on  $SrTiO_3$  does relax in its  $c$ -axis lattice parameter, just not as quickly as predicted computationally. This is also confirmed by fitting experimental XRD data available for a sample of 25 unit cells of  $LaNiO_3$  deposited on  $SrTiO_3$ , which resulted in a  $c$  lattice parameter of 3.8341 Å. The fit details are found in the Appendix.

This means that if we ignore the change in tilt patterns we can decouple the  $SrTiO_3$  bulk substrate from the  $LaNiO_3/LaCoO_3$  superstructure,

and only investigate an in plane strained topmost part of the experimental structure with the in-plane lattice parameter being set to that of  $SrTiO_3$ .

### 6.1.3 Impact of epitaxy on $LaFeO_3$

In a study by Seo et al. [181], where  $LaFeO_3$  was grown onto  $SrTiO_3$ , it was observed that the c-axis parameter of  $LaFeO_3$  increased by 0.4% , and the glazer tilt system changed to enable in plane twinning (this would mean going from a  $a^+b^-b^-$  to a  $a^+a^+b^-$  or a  $a^-a^-b^-$  glazer tilt system).<sup>2</sup>

In the same study negative exchange bias in magnetic measurements of  $LaFeO_3$  was found, suggesting a complicated spin environment. There are also reports of Ferromagnetic ordering in thin  $LaFeO_3$  films, which are accompanied by oxidation state and octahedral volume ordering [183].

These findings highlight that  $LaFeO_3$  is a material with a strong spin–lattice interaction and that it is important to consider changes in lattice when representing this material.

### 6.1.4 Impact of epitaxy on $LaCoO_3$

Many authors find that  $LaCoO_3$  thin films have a FM spin ordering with an average measured magnetisation of  $0.7 \mu_B$  per Co atom [185][141]. Similar behaviour of  $LaCoO_3$  has been seen in bilayer structures together with  $LaNiO_3$  [143]. The cause of this FM spin ordering has been revealed in studies by both Sterbinsky et al. [186] and Fuchs et al. [187] to be strain and distortion driven.<sup>3</sup>

The tensile strain of these films leads to octahedral stretching which in turn reduces tilting, these two lead to FM for any Co-O-Co angle above 160 deg. Moreover according to Fuchs et al. the magnetisation is linearly dependant on the in plane lattice parameter set by the substrate, this is shown in figure 6.4.

Meng et al. [142] and Durand et al. [188] also see such FM behaviour, but highlight that it not only comes from strain but also possibly from Oxygen vacancies and their ordering.

Both Wang et al. and Rata et al. find the the out of plane lattice parameter of  $LaCoO_3$  to be roughly  $3.78 \text{ \AA}$ , when constrained to  $SrTiO_3$ , and they also see a general volume increase from  $55 \text{ \AA}^3$  to  $57.5 \text{ \AA}^3$ . [141, 147]

[181]: Seo et al. (2008), *Antiferromagnetic  $LaFeO_3$  thin films and their effect on exchange bias*

2: It has to been found that tilts and buckling in orthoferrites ( $RFeO_3$ ) causes changes in exchange interaction promoting different spin orderings.[182]

Paudel et al. see a valence band maximum shift of 0.28-0.33 eV upwards for  $LaFeO_3$  when pinned to  $LaNiO_3$ . In the same paper Paudel et al. highlight an increase in OER activity for this superstructure [184].

[185]: Posadas et al. (2011), *Epitaxial integration of ferromagnetic correlated oxide  $LaCoO_3$  with Si (100)*

[141]: Rata et al. (2010), *Lattice structure and magnetization of  $LaCoO_3$  thin films*

3: LCO on STO has roughly 2.2% strain

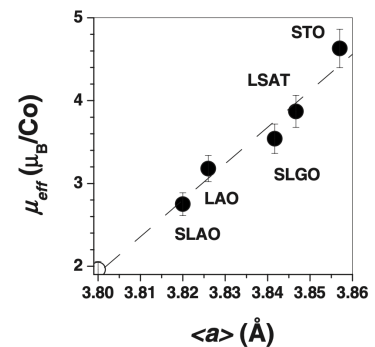


**Figure 6.4:** The observed linear relation between Co magnetisation and average lattice parameter from Fuchs et al. [187]. The average lattice parameter is the average of the a,b,c parameters of the unit cell.

## 6.2 Slab convergence and relaxation

In order to correctly represent a surface termination in VASP, we need to create a slab and place it in the middle of vacuum. This vacuum is needed to make sure that our structure will not interact with its periodic images on the top and bottom of the structure. This image problem, while a blessing in bulk calculations, is a crux of the plane-wave representation in abruptly terminated finite structure calculations. Just in the previous Chapter the chosen structure is relaxed afterwards.

### 6.2.1 Converging vacuum and slab thickness

Since we know that the "bulk" of our material here will be  $LaNiO_3$ , the convergence tests are carried out for  $LaNiO_3$  only.

The approach taken here is to first converge vacuum size necessary for the surface termination of  $LaNiO_3$ , after that the size of the slab in the z direction is converged. The parameters themselves are converged with respect to the surface energy, which is defined as the slab energy minus the equivalent bulk energy (if a slab is 4 unit cells thick then you would subtract four times the energy of the bulk unit cell) divided by the surface area exposed.

Firstly a single unit cell of  $LaNiO_3$  is taken, and then vacuum is added symmetrically to the cell on each side<sup>4</sup>. The structure is then converged and the energy per surface area is extracted. This is repeated for a multitude of vacuum sizes. The results can be seen in the figure 6.5.

4: This is done by increasing the computational cell in size in the z direction, with the single cubic unit cell of  $LaNiO_3$  in the middle.

Here 30 Å of vacuum was chosen as 20 Å seems to be converged but the extra 10 Å are added to accommodate for the two unit cells of either  $LaCoO_3$  or  $LaFeO_3$  to be added.

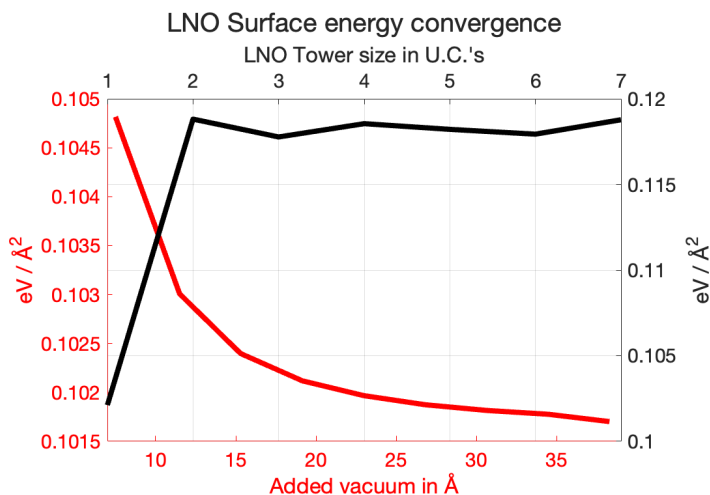


**Figure 6.5:** Surface energy of the LNO slab as a function of size and added vacuum. The Fiorentini and Methfessel correction to bulk energy is used to obtain true surface energy convergence [189].

To converge the thickness, cells of many monolayers were built, and to each of them 30 Å of vacuum was added. These structures were again converged and their surface energies extracted, these energies as a function of size can be seen figure 6.5.

While the calculation is convergent at 2 monolayers of  $LaNiO_3$ , the 4 monolayer structure is chosen as a safety margin. The 4 monolayer structure is chosen over the 3 monolayer structure, as that is the next number up from 2 which can represent different types of spin ordering in the cubic Ni sub lattice of  $LaNiO_3$ .

### 6.2.2 Slabs and relaxation

The eventual structures consist of  $2 \times 2 \times 4$  unit cells of  $LaNiO_3$  topped with  $2 \times 2 \times 2$  unit cells of  $LaCoO_3$  or  $LaFeO_3$ . The  $2 \times 2$  structure in the a-b plane is chosen as it can represent the magnetic orderings and possible anti-phase tilts of the constituent materials. These structures can be seen in the figure 6.6 below. Further when referring to the "bottom" or "top" of these structures, it is done with the context of this image and the C axis within it.

The exact details pertaining to the construction of these cells can be found in the Appendix.

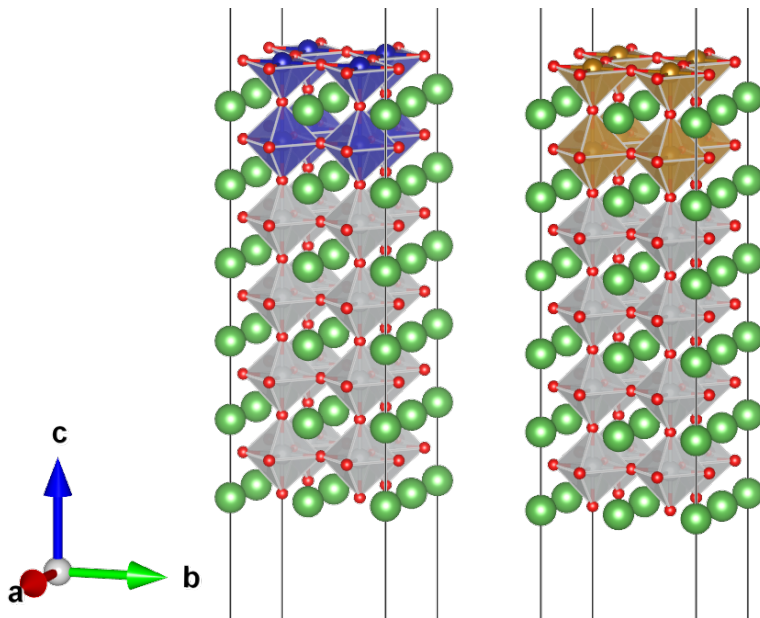


**Figure 6.6:** The *experimental* slabs. On the left is the  $LaNiO_3$ - $LaCoO_3$  stack and on the right you have the  $LaNiO_3$ - $LaFeO_3$  stack.

The atomic positions were allowed to relax in the computational cell in two ways:

1. A way where the bottom mono layer of  $LaNiO_3$  was constrained to the  $SrTiO_3$  in plane parameters only allowing the top most part to relax.
2. A way where all the atomic positions could relax.

In most of this Chapter, I will discuss the results of the structures relaxed with the second method, as it was the method where relaxation was run without symmetries enabled - leading to octahedral tilts and other physical distortions.

The the structures relaxed with the first type of relaxation did not display any octahedral distortions or bond buckling and only developed Jahn-Teller distortions. This is because the relaxation runs were run with

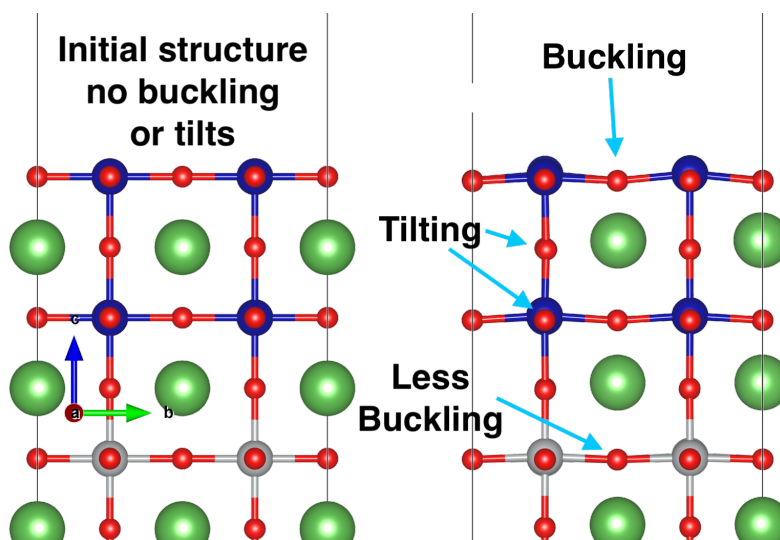
symmetries enabled. If the results from structures relaxed with the second method are discussed, it will be explicitly mentioned.

#### *LaNiO*<sub>3</sub>-*LaCoO*<sub>3</sub> slab relaxation changes

In the whole stack the tilting behaviour of *LaNiO*<sub>3</sub> increases from the bottom to the top. Growing from no tilts ( $a^0a^0a^0$ ) to  $a^-a^-c^{-/0}$  with  $a = 1.16^\circ$ ,  $b = 1.1^\circ$  and  $c = 0.025^\circ$ , as expected from literature. It has to be said that the amplitude of tilting here is far less than what was reported in literature. The x and y axis are almost twinning but the z axis has massively reduced tilting (essentially  $a^0$ ) when compared to the experimental structure findings in Ch. 4 table 4.4. The tilting values did not reach the computational ones found by McBride due to the fact that there was no *SrTiO*<sub>3</sub> at the structure base, and this was not simulated via an added potential. The only constraint was the in plane lattice parameter of *SrTiO*<sub>3</sub> and the *LaNiO*<sub>3</sub>-*LaCoO*<sub>3</sub> interface.

Moving upwards to the *LaCoO*<sub>3</sub> layer, *LaCoO*<sub>3</sub> further exaggerates this tilting to  $a^-b^-c^-$  with  $a = 1.5^\circ$ ,  $b = 3.42^\circ$  and  $c = 0.37^\circ$ . The tilts of the *LaCoO*<sub>3</sub> thus couple with those of the *LaNiO*<sub>3</sub> "bulk". These tilts are measured at the very top octahedra of the structure.

**Figure 6.7:** Relaxations results of the top of the *LaNiO*<sub>3</sub>-*LaCoO*<sub>3</sub> slab with the unrelaxed slab on the left and the relaxed one on the right. Only the top is shown as that is where the distortions are the largest.



A visualisation of the differences in structure arising from relaxation is shown in figure 6.7. Here buckling is also highlighted. In *LaNiO*<sub>3</sub> the buckling angle grows from  $179^\circ$  at the bottom of the structure to  $176^\circ$  at the top of the structure. The *LaCoO*<sub>3</sub> again increases this buckling from  $171^\circ$  at the lowest *LaCoO*<sub>3</sub> layer to  $168^\circ$  at the very top of the structure.

The out of plane lattice parameter of *LaNiO*<sub>3</sub> expanded from initialised  $3.71 \text{ \AA}$  to a gradient starting at  $3.79 \text{ \AA}$  near the interface and ending at  $3.87 \text{ \AA}$  at the bottom end of the structure. While this follows the experimental trend seen in figure 6.3 of out of plane lattice parameters increasing (resulting in a negative Poisson's ratio). It has to be said that the *inverse* nature of relaxation, where the bottom relaxes the most, is a product of the way structures are relaxed with VASP, i.e. the bottom most atoms are more free to move than the ones at the interface. This could be mended by

relaxing for a substantially longer time, or manually editing the structure and searching for the lowest energy solution.

On the other hand  $LaCoO_3$  out of plane lattice parameter shrunk from the initialised 3.79 Å to 3.71 Å further intensifying the Jahn-Teller distortions induced when the in-plane lattice parameter was constrained to that of  $SrTiO_3$ . Notably the structure showed ordering of lower and higher volume octahedra, characterised by different Co-O bond lengths, with these differences being larger at the topmost layer. This means that the top of the  $LaCoO_3$  structure starts showing bulk like  $R\bar{3}c$  like behaviour shown in Ch. 4 table 4.3, which exhibits octahedra ordering in size.

#### $LaNiO_3$ - $LaFeO_3$ relaxation changes

The  $LaNiO_3$  stack did not exhibit any tilting along the z direction with a resultant tilting structure of  $a^-a^-a^0$  similar to the one found in the previous superstructure.

The x and y tilts actually decreased as the  $LaFeO_3$  part of the structure was approached, reducing from  $a \approx 0.3^\circ$  to  $a \approx 0.1^\circ$ . This "anti-coupling", where the tilts are larger away from the surface rather than closer to it, could be explained by the fact that when relaxing, these structures transform from the cubic forms to different forms closer to the distorted cells seen in Ch.4. And the distorted cells of  $LaNiO_3$  and  $LaFeO_3$  seen Ch. 4 are of different tilt systems.

In the top structure the  $LaFeO_3$  tilting shows the experimentally found x-y axis twinning, showing a tilting system of  $a^-a^-b^-$  with  $a = 0.87^\circ$  &  $0.89^\circ$  for the x and y tilts and  $b = 0.133^\circ$ . The relaxed tilts are smaller in amplitude compared to what one might expect when looking at the tilt angles found in the distorted  $Pnma$  structure of  $LaFeO_3$  in Ch.4 ( $a = 1.25^\circ$  and  $b = 8.33^\circ$ ).

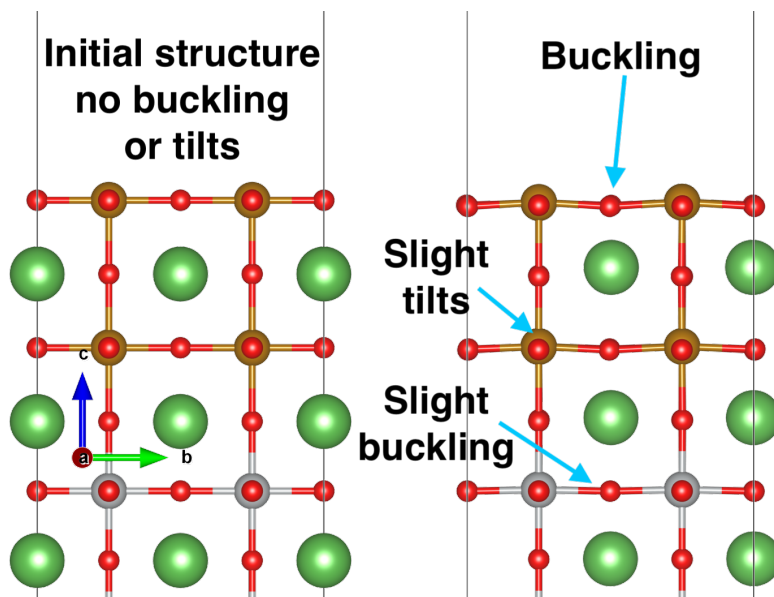


**Figure 6.8:** Relaxations results on of the  $LaNiO_3$ - $LaFeO_3$  slab with the unreaxed slab on the left and the relaxed one on the right. Only the top of the structure is displayed.

The comparison of the relaxed structure to the initial one is shown in figure 6.8. The bond buckling amplitudes of the Tm-O-Tm bonds found



in this system are smaller compared to the previous superstructure (there it was the Co-O-Co bond).

The buckling angle in the  $LaNiO_3$  increased from  $170^\circ$  at the bottom of the structure to  $177^\circ$  at the top, where the  $LaNiO_3 - LaFeO_3$  interface is located. The  $LaFeO_3$  structure was more buckled than the  $LaNiO_3$  sub layer with the buckling angle growing from  $\approx 175.5^\circ$  near the interface to a buckling angle of  $\approx 173.5^\circ$  at the very top.

The final buckling angle of  $173.5^\circ$  is rather unexpectedly large when compared to the smaller buckling angle of  $168^\circ$  seen for the topmost  $LaCoO_3$  layer in the previous superstructure, as experimentally,  $LaFeO_3$  should have the smallest buckling angle out of all the  $La - 3dTM - O_3$  perovskites [181].

The out of plane lattice parameter of  $LaNiO_3$  expanded from the initialised  $3.78 \text{ \AA}$  to a gradient, starting at  $3.78 \text{ \AA}$  found near the interface with  $LaFeO_3$ , to  $3.85 \text{ \AA}$  at the bottom of the structure, similar to the previous superstructure.

The out of plane lattice parameter of  $LaFeO_3$  shrunk from the initialised  $4.01 \text{ \AA}$  to  $\approx 3.92 \text{ \AA}$ , resulting in a negative Poisson ratio.



## 6.3 Magnetic and Charge results

Here the local magnetic moment and charge results of the slabs are discussed. These results are then compared to those of the reference structures seen in Ch. 4.

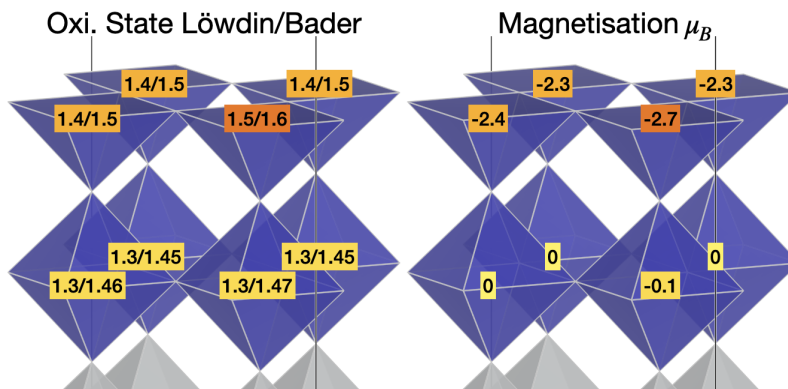
### 6.3.1 $LaNiO_3 - LaCoO_3$ slab results

The magnetic moments are initialised as FM for the Ni atoms and both FM and AFM-G for the Co atoms, due to the magnetic ambiguity of this material.

The structure where Co was initialised in the FM ordering converged with a strange spin ordering across the whole structure and locally quenched spins. Next to this unexpected behaviour, this structure was 28 meV higher in energy per formula unit<sup>5</sup> compared to the structure where the Co was initialised in the AFM-G ordering. Therefore this structure is not discussed here. The results presented here are from the structure where Co was initialised in the AFM-G ordering.

The Löwdin and Bader oxidation state results as well as the local Löwdin projected magnetic moments are shown in figure 6.9.

The Co atoms near the  $LaNiO_3-LaCoO_3$  interface in figure 6.9 seem to have a lower oxidation state compared to the Co atoms at the top, near the surface. There exists a positive correlation with local magnetisation of Co and oxidation state, in line with the findings of Ch. 4 which indicate that the low-spin Co is more covalent, effectively having more charge when compared to the high-spin Co.



5: In this case the energy of the both structures was divided by the total number of unit cells as there are two materials present.

**Figure 6.9:** Top two layers of  $LaCoO_3$  with the oxidation states and the local projected Löwdin magnetic moments of Co.

If we compare the charge and magnetic moments seen in 6.9, the values seem similar to those of the  $R\bar{3}c$  structure FM results shown in Ch. 4.

As mentioned before both studies of Sterbinsky et al. [186] and Fuchs et al. [187] have shown that the increased in plane stretching should lead to *less* distortions and buckling thus increasing the magnetic moment, however the findings here and in Ch. 4 indicate that this trend is inverted. The findings of this thesis show that  $LaCoO_3$  structures with more lattice distortions exhibit a higher spin and oxidation state.

The low spin Co found in the layer closer to the interface is very logical from the perspective that the out of plane lattice parameter of  $LaCoO_3$

shrunk, as it was previously discussed in Ch.4 that the ionic radius of the low spin  $\text{Co}^{3+}$  is smaller than that of the high spin  $\text{Co}^{3+}$  ion.

Another notable thing is the induced insulator to metal transition of  $\text{LaCoO}_3$ . The averaged DoS of each of the Co in each of the  $\text{LaCoO}_3$  layers can be seen in figure 6.10. Such transitions have been shown to be introduced either by pressure or temperature, i.e. added energy to the system. [112, 190, 191]

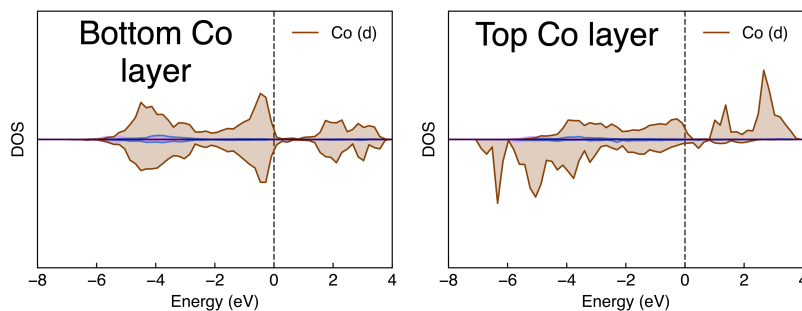


**Figure 6.10:** An apparent insulator to metal transition. With the bottom Co DoS likening to the cubic one but the top one showing  $R\bar{3}c$  FM ordering like results from Chapter 3.

Now examining the  $\text{LaNiO}_3$  sub layer whose magnetisation and charge results can be seen in figure 6.11. A spin reversal at the interface is seen when compared to the spin sign of  $\text{LaCoO}_3$  seen in figure 6.9. Another notable feature is the apparent formation of an AFM ordering on the  $\text{LaNiO}_3$  surface at the bottom of the structure, where the  $\text{LaNiO}_3$  substructure is exposed to vacuum.

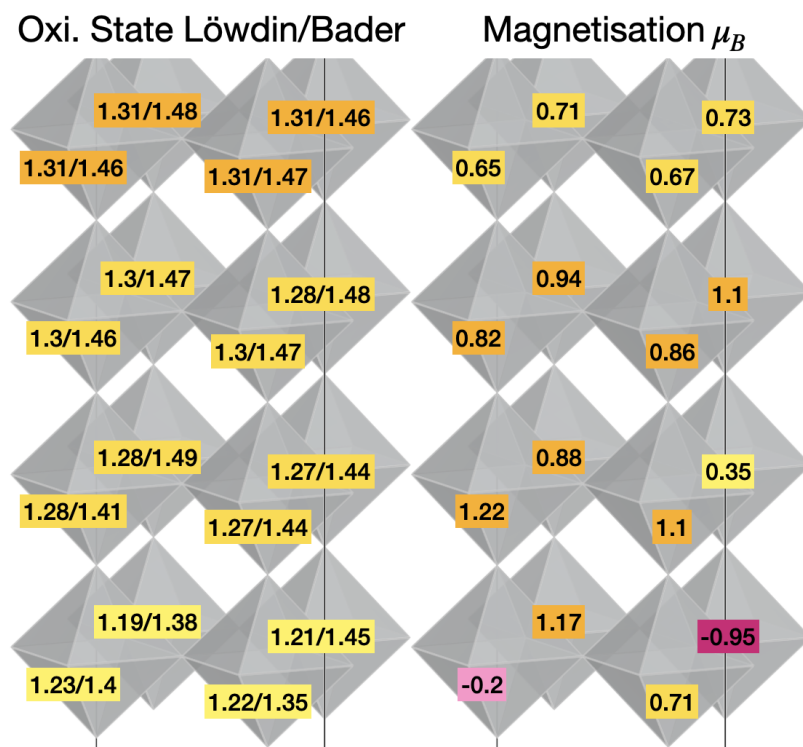


**Figure 6.11:** Bottom four layers of LNO with the oxidation states and the local projected Löwdin magnetic moments of Ni.

The apparent AFM ordering in  $\text{LaNiO}_3$  thin films has been discussed by Guo et al. [118] and Liu et al. [192]. It appears that in this case the  $\text{LaNiO}_3$  surface at the bottom of the structure has developed this ordering, either

[192]: Liu et al. (2020), *Observation of an antiferromagnetic quantum critical point in high-purity  $\text{LaNiO}_3$*

because it has an exposed "free" surface, or because of the distortions, which were found to be largest at the bottom of the  $LaNiO_3$  layer.

It also seems that the oxidation state of the Ni atoms is larger at the top, near the  $LaNiO_3$ - $LaCoO_3$  interface, when compared to the Ni atoms at the bottom of the structure. However we have to take in mind the observations of structural distortions here. It was found that as you approach the  $LaCoO_3$  layers the distortions get smaller. Which would mean that the changes in oxidation state are in line with a gradient from  $R\bar{3}c$  structure Ni oxidation state of 1.26 to the cubic structure Ni oxidation state of 1.33 found in Ch. 4.

To get a better insight on the validity of the predictions of Zhong and Hansmann [15] the average oxidation state of the TM metals per layer is plotted against the oxidation states of the reference structures found in Ch. 4, this comparison can be seen in figure 6.12. The cubic reference is that of the Cubic reference structure, and the Experimental reference is that of the distorted structures for each material. In this case that would be the  $R\bar{3}c$  structure of both  $LaCoO_3$  and  $LaNiO_3$ .

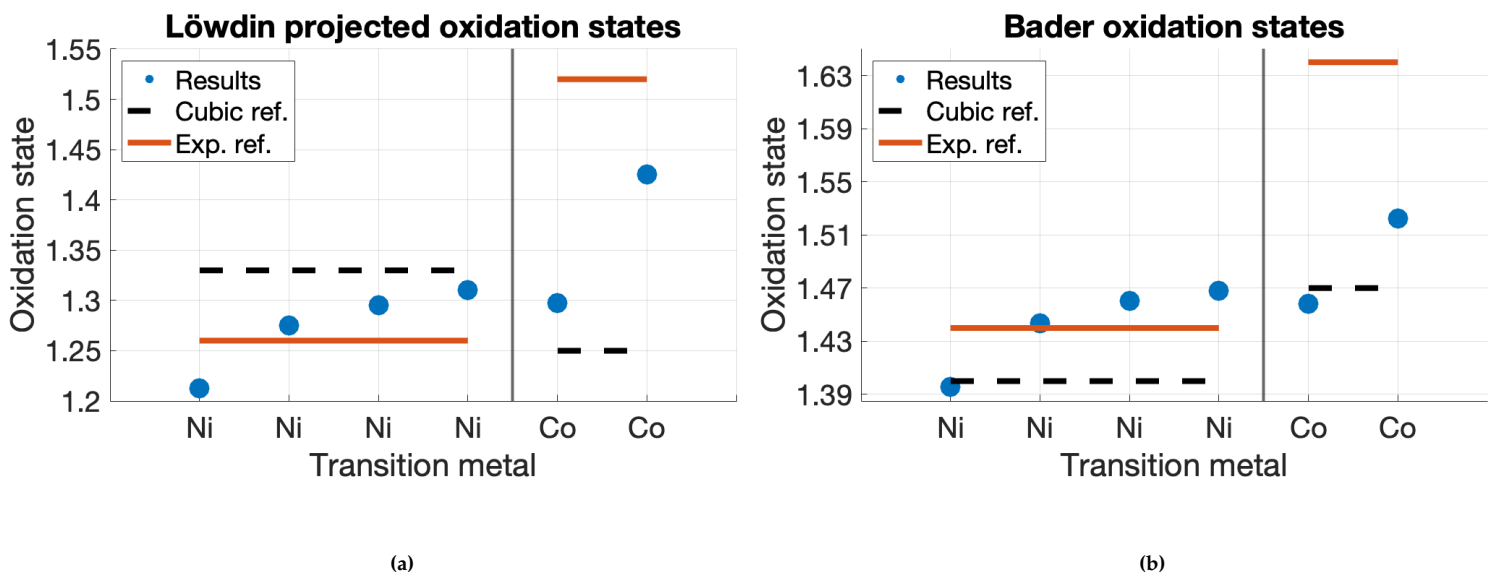


**Figure 6.12:**  $LaNiO_3$ - $LaCoO_3$  slab layer averaged TM Bader and Löwdin oxidation states compared to the oxidation states of the reference structures in Ch. 4. The interface is marked by the vertical black line.

If we examine the Ni oxidation states seen in figures 6.12a and 6.12b, they seem to be most like the oxidation states found in the distorted  $R\bar{3}c$  structure marked by the orange line and reported in Ch.4. In both figure 6.12a and 6.12b the oxidation states of Ni seem to follow the same trend and even the same trajectory of increasing as we approach the  $LaNiO_3$ - $LaCoO_3$  interface. It has to be noted that this change is also correlated with the decrease in out of plane lattice parameter of  $LaNiO_3$  going from the bottom of the structure (here on the left hand side) to the  $LaNiO_3$ - $LaCoO_3$  interface (here marked by the vertical black line).

Proceeding to the oxidation states of Co, again shown in figures 6.12a and 6.12b, they exhibit a trend of increasing when moving further away from the  $LaNiO_3$ - $LaCoO_3$  interface marked by the vertical black line. While

in figure 6.12a all the Löwdin projected oxidation states are higher than the Cubic reference oxidation states, in figure 6.12b the Bader oxidation state of the Co atom just above the interface is slightly below the Cubic reference oxidation state. Just as with Ni, the oxidation state changes seem to be correlated with the shrinking out of plane lattice parameter, which for  $LaCoO_3$  was more pronounced at the top of the structure.

Another reason for this strange trajectory of oxidation states is polarisation at the interface which was calculated to be  $7.75 \mu C/cm^2$  as per Löwdin projections. These are calculated by a simple dipole calculation of all the atomic positions and their Löwdin projected oxidation states. This would lead to a dipole forming along the z axis moving charge towards one end.

Nevertheless these results are in line with the extended prediction of Zhong and Hansmann, which predict a decrease in oxidation state of Co and an increase of oxidation state of Ni upon contact.

In a bid to exclude such possible influence of structural parameters and polarisation in this analysis the  $LaNiO_3$  and  $LaCoO_3$  slabs were severed at the interface and converged individually. The atomic Bader and Löwdin oxidation states of the separated structures were then subtracted from the structure with the interface. This leads to an oxidation state difference graph seen in figure 6.13.

In this graph it is clear to see that the oxidation state of Ni below the interface is higher and the Co oxidation state just above the surface is significantly lower. It has to be disclaimed that *This graph was made with the structures relaxed using the first relaxation method and therefore only have Jahn-Teller distortions..*

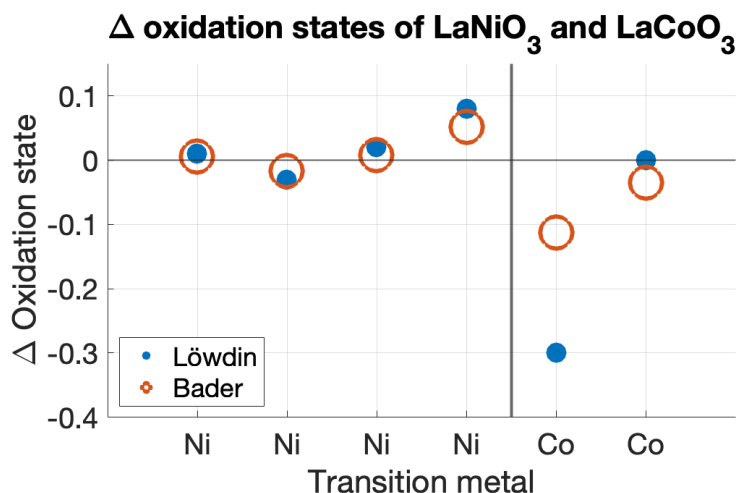


**Figure 6.13:** The oxidation state difference between the interfacial structure and the constituent slabs on their own. *This graph was made with the structures relaxed using the first relaxation method and therefore only have Jahn-Teller distortions.*

This result is very much in line with the prediction of Zhong and Hansmann [15] with increasing Ni oxidation states near the interface and decreasing oxidation states of Co near the interface.

### 6.3.2 $LaNiO_3 - LaFeO_3$ slab results

The magnetic moments were initialised as AFM-G for the Fe atoms as per expected lowest energy ordering discussed in Ch.4, and the Nickel atoms were initialised in a FM ordering.

The local Fe oxidation states and local magnetic moments can be seen in figure 6.14. Just as with Co in the previous superstructure it seems that high oxidation state is correlated with high local magnetisation. A notable observation is that in the  $LaFeO_3$  layer closer to the  $LaNiO_3 - LaFeO_3$  interface the magnetic ordering of Fe is Ferromagnetic, while in the surface layer above it returns to AFM-G type ordering, albeit with somewhat quenched magnetisation for one channel.

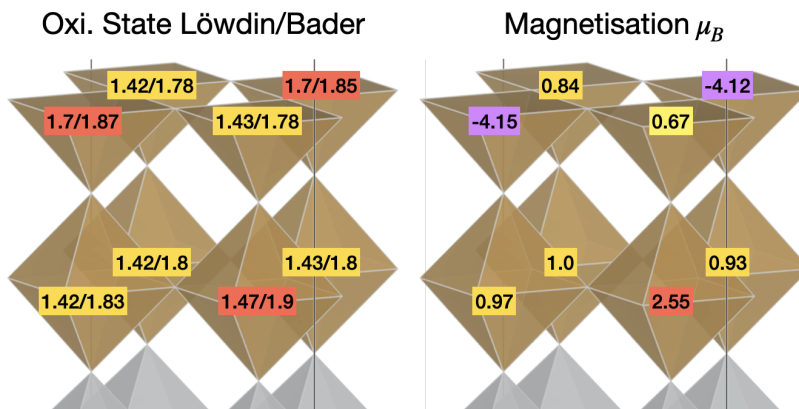
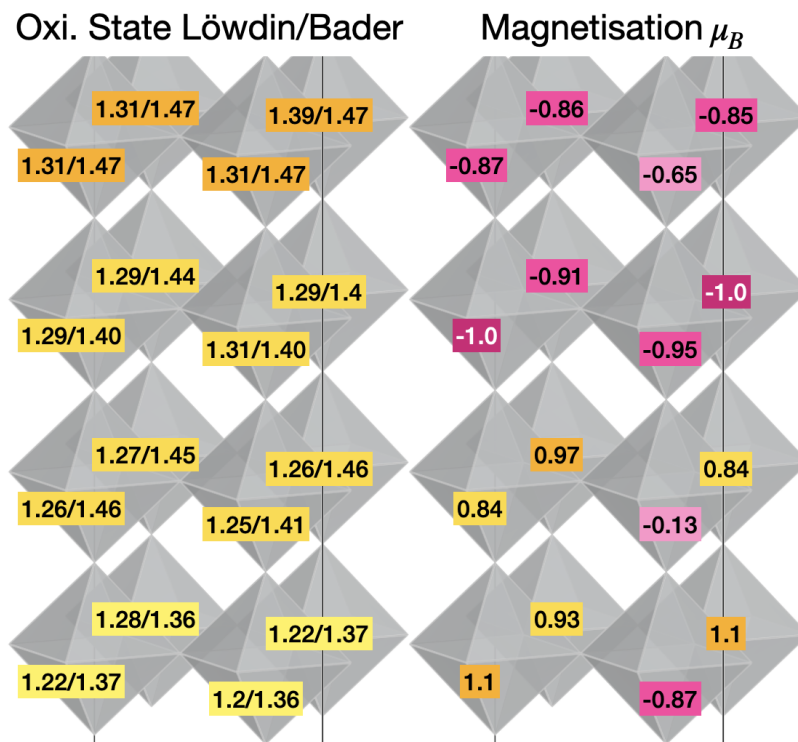


Figure 6.14: Top two layers of LFO with the oxidation states and the local projected Löwdin magnetic moments of Fe.

What is more interesting, is that negative high magnetisation Fe atoms have a high Löwdin oxidation state and a somewhat elevated Bader oxidation state, while for the positive high magnetisation Fe atom in the lower layer it is the other way around. This might come from the fact that at the interface the bonding is more ionic, while at the top layer the bonding is more covalent.

Now moving on to the  $LaNiO_3$  sub layer; unlike in the Fe of the  $LaFeO_3$  layer above, the Ni atoms do not exhibit a correlation between oxidation state and local magnetic moment. But just as with the previous superstructure ( $LaNiO_3 - LaCoO_3$ ) the oxidation state seems to grow monotonously approaching the  $LaNiO_3 - LaFeO_3$  interface on top. Just as before the increasing oxidation state of Ni is correlated with decreasing out of plane lattice parameter going from the bottom of the structure to the  $LaNiO_3 - LaFeO_3$  interface. This is visualised in figure 6.15.



**Figure 6.15:** Bottom four layers of  $LaNiO_3$  in the superstructure with  $LaFeO_3$ . Displaying the oxidation states and the local projected Löwdin magnetic moments of Ni.

Observing the local magnetic moments of Ni in figure 6.15, it is clear that at the  $LaNiO_3 - LaFeO_3$  interface at the top, the majority spin channels flip. Moving down the structure, at the halfway point there is a *switch of magnetic domains*. This ordering, found in the lowest eight octahedra in figure 6.15 cannot be matched with any of the known cubic lattice orderings displayed in figure 4.11 in Ch.4.

One would expect that due to our *forced* U parameter and metallic behaviour of the material, that the Ni in  $LaNiO_3$  would always comply to the stoner criterion with one type of majority spins dominating. But this is not the case, and there is no physical change there that could facilitate a change in magnetic domains. The ordering is also not periodic *in an apparent fashion* so this is less likely to be the kind of AFM ordering discussed in the experimental papers.

The fact that this current spin structure does not fit in any cubic ordering could mean either it being the best effort of the material to represent a paramagnetic state (the physical, experimental state) in a format where spins can only be parallel, or that this structure still does not allow for a correct representation of the magnetic ordering of this material.

In any case, we can examine the the layer averaged transition metal oxidation states in figures 6.16a and 6.16b. Here the layer averaged TM oxidation states are plotted with the oxidation states of the reference structures found in Ch.4. The cubic reference is that of the simple cubic structure of each constituent material, and the experimental structure reference is that of the distorted cells. That is  $Pnma$  for  $LaFeO_3$  and  $R\bar{3}c$  for  $LaNiO_3$ .

Just as before there is a monotonous increase in Ni oxidation states going from the bottom of the structure to the  $LaNiO_3 - LaFeO_3$  interface, with

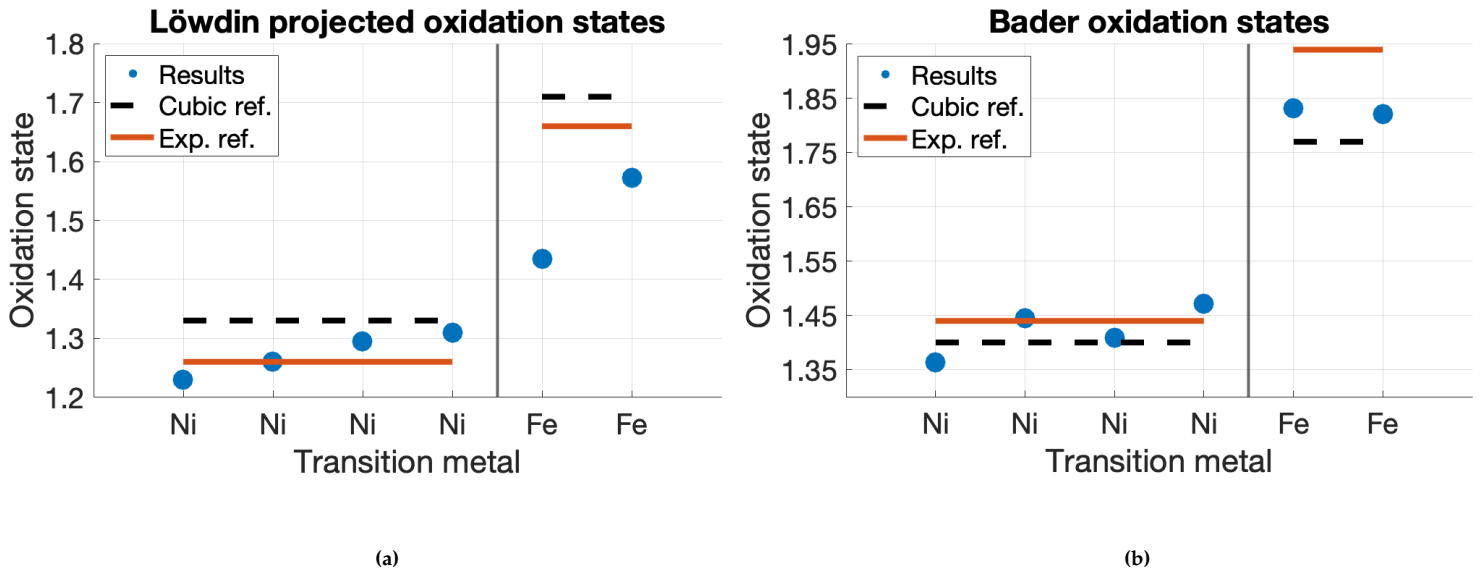


**Figure 6.16:**  $LaNiO_3$ - $LaFeO_3$  slab layer averaged TM Bader and Löwdin oxidation states compared to the oxidation states of the reference structures in Ch. 4. The interface is marked by the vertical black line.

the overall average oxidation state of Ni liking more to the oxidation state of the distorted structure.

Another possible reason for this trajectory of oxidation states is polarisation at the interface which was calculated to be  $9.61 \mu C/cm^2$  as per Löwdin projections. These are calculated by a simple dipole calculation of all the atomic positions and their Löwdin projected oxidation states. This would lead to a dipole forming along the z axis moving charge towards one end. Such polarisation is expected and has been seen experimentally [193].

The Fe Löwdin projected oxidation states seem to be in line with the expanded Zhong and Hansmann prediction of Chapter 3 figure 3.6 - the oxidation state of Fe is lower than that of all the reference structures from Ch. 4. On the other hand Bader oxidation states show that there is no change at hand and the local oxidation states are in-between the oxidation states of the non-distorted and the fully distorted reference. As this structure allows for distortions such as tilting and buckling, it is therefore reasonable to assume that the oxidation state is elevated due to these distortions.

Just as for the previous superstructure, in a bid to exclude such possible influence of structural parameters in this analysis the  $LaNiO_3$  and  $LaFeO_3$  slabs were severed at the interface and converged individually. The atomic Bader and Löwdin oxidation states of the separated structures were then subtracted from the structure with the interface. This leads to an oxidation state difference graph seen in figure 6.13.

Here the oxidation states of Ni below the interface are lower than for the individually converged slab, and the Fe oxidation states closer to the surface are lowered substantially. It has to be disclaimed that *This graph was made with the structures relaxed using the first relaxation method and therefore only have Jahn-Teller distortions..*



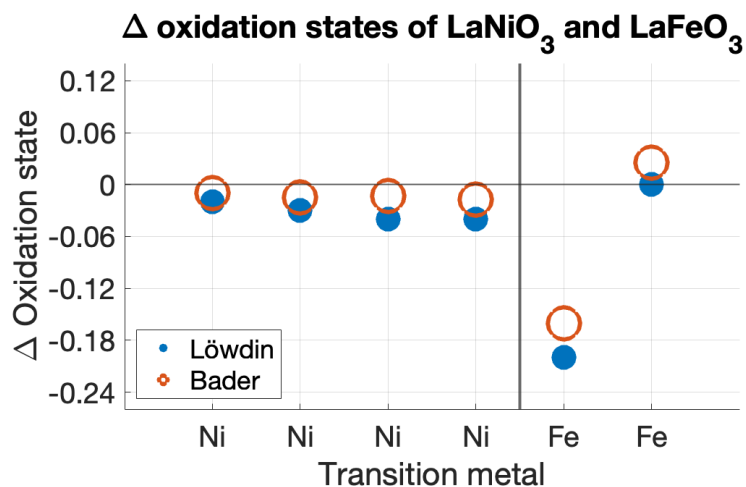


**Figure 6.17:** The oxidation state difference between the interfacial structure and the constituent slabs on their own. This graph was made with the structures relaxed using the first relaxation method and therefore only have Jahn-Teller distortions.

Here a large difference in Fe oxidation state between the structures with and without the interface is found, the change in oxidation state at the interface is smaller than that of the  $\text{LaCoO}_3\text{-LaNiO}_3$  superstructure, in line with the prediction. Unlike for the  $\text{LaCoO}_3\text{-LaNiO}_3$  superstructure, the Ni oxidation states do not increase near the interface. But the conclusion here is that the prediction of Zhong and Hansmann [15] is only partially true for this structure.

## 6.4 Conclusions and orbital occupancy

When the spin states and distortions of these materials are represented correctly, a multitude of interesting observations can be made, many of which have also been confirmed experimentally.

While in some cases the magnetic ordering and structural distortion description could be improved from the one presented here, it is safe to say that these structures are quite representative of the experimental ones. Moreover, when the possible inhomogeneity of charge, due to polarisation or local difference in unit cell size, was accounted for, it looks that the prediction of Zhong and Hansmann [15] holds merit.

While bonding and  $e_g$  orbital occupancy changes were discussed at the start of the thesis to be predictors of OER performance this is left as future work.

Initially, it was shown in Ch.3 that due to the simple structures and choice of functional used by Zhong and Hansmann [15] in making the original predictions, the authors end up predicting un-physical properties in these Tm-O perovskites indicating that this prediction would most likely fail in real life.

This idea of correct representation was built upon in Ch.4 where it was highlighted that these structures have a very intricate relationship between structure and the spin and oxidation states of the transition metal ions. It was also shown that often breaking physical symmetries was more important than the choice of functional when seeking correct representation.

This lack of proper representation in Ch.5 showed that these materials will indeed behave unexpectedly if not represented correctly and will converge to both erroneous lattice sizes and magnetisations.

The description was improved in Ch.6., where it was possible to partially represent the correct magnetic orderings and distortions of these materials. This led to results that were seemingly more physical and also more in line with experimental observations. While the results themselves still suffered from representation issues such as cell size and oxidation state correlations and possible issues due to polarisation, when it was at least partially accounted for these issues the extension of the original prediction of Zhong and Hansmann [15] in Ch.3. was shown to hold some merit.

It has to be noted that the prediction here held true in its entirety only for one of the two superstructures tested - the  $LaNiO_3 - LaCoO_3$  one. And only two combinations, out of the hundreds possible, were tested here, meaning that the theoretical prediction of Zhong and Hansmann [15] cannot be fully verified or falsified even for the two combinations explored here. Moreover it is hard to say if the cause of the charge transfer in the structures tested was fully due to band alignment.

As it was shown, the materials explored in this thesis show sensitivity to structural changes, that result in changes of magnetic ordering, local magnetic moments and oxidation states. In further research into this topic, both computational and experiential, more attention has to be devoted to the separation of these variables from the variable of interest; namely the formation of a heterointerface between two transition metal oxide perovskites.

The following steps should be to first fully understand the distortion and tilting behaviour of these materials when in contact with each-other. Then to try and understand how that influences the magnetic and charge behaviour of the system, and whether or not these computational observations are physical or just products of the limited computational representation. Finally if this is understood, then a larger structure containing more cells of each material should be made and explored computationally. The previously gained knowledge about the local influence

of structure on magnetisation and charge states would then allow for a decoupled analysis of the charge transfer, isolating the heterointerface as the only new variable.

# APPENDIX



# A

## Computational details and convergence tests.

Here the computational details regarding the process of producing the results are broken down by chapter.

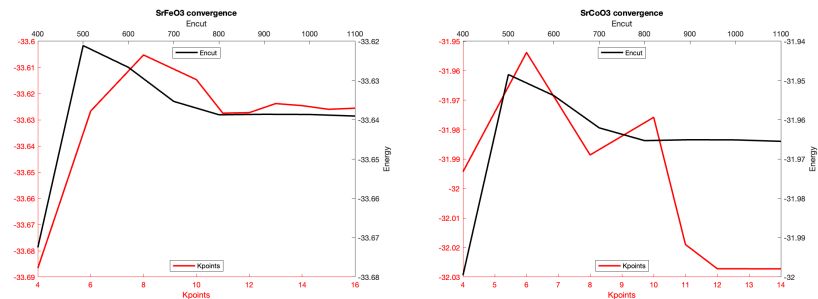
### A.1 Chapter 3

Most of the computational details are disclosed in the Chapter itself, so the information presented here is extra to that.

To benchmark the reproduce-ability of the data presented in Figure 1.6 (Ch. 1), not only was the La - TM3d line reproduced but also the Sr - Tm line. The O2p and Tm-d averages were not extracted from the Sr line.

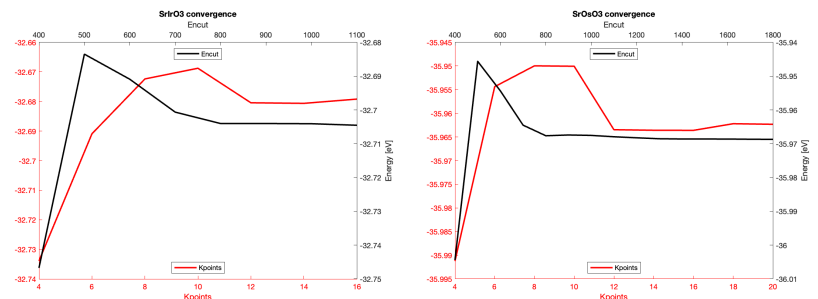
Firstly the structures were obtained from Materials project [194], and convergence tests were done. A selection of the convergence tests is displayed in figure A.1. These convergence tests show that these materials need high plane wave cut-off energies and a fine K-point grids.

A.1 Chapter 3 . . . . .	91
A.2 Chapter 4 . . . . .	93
A.2.1 Magnetic ordering of $LaNiO_3$ . . . . .	94
A.3 Chapter 5 . . . . .	96
A.3.1 $LaNiO_3$ - $LaCoO_3$ interface vertical relaxation . . . . .	96
A.3.2 $LaNiO_3$ - $LaFeO_3$ interface vertical relaxation . . . . .	97
A.3.3 Magnetic ordering . . . . .	97
A.3.4 HSE06 results for $LaNiO_3$ - $LaCoO_3$ . . . . .	98
A.4 Chapter 6 . . . . .	100
A.4.1 Vertical relaxation of $LaNiO_3$ . . . . .	100
A.4.2 Vertical relaxation of $LaFeO_3$ . . . . .	100
A.4.3 Vertical relaxation of $LaCoO_3$ . . . . .	100
A.4.4 XRD result fitting . . . . .	101
A.4.5 Slab relaxation issues . . . . .	101



(a)  $SrFeO_3$  convergence

(b)  $SrCoO_3$  convergence



(c)  $SrIrO_3$  convergence

(d)  $SrOsO_3$  convergence

[194]: Jain et al. (2013), *Commentary: The Materials Project: A materials genome approach to accelerating materials innovation*

Figure A.1: The ENCUT (Plane wave cut-off energy) and K-point convergence graphs for select Sr line unit cells.

Since these calculations are of small cubic unit cells, it was decided to use 12x12x12 regular gamma centered k-point grids for all the calculations and a plane wave cut-off energy of 1000eV for all the structures.

Using these parameters the structures were relaxed using PBE until all the forces were less than  $10^{-8} eV/\text{angstrom}$ .

As it was not a-priori known if these are insulators, metals or semiconductors Gaussian smearing was used (ISMEAR=0) with a smearing parameter SIGMA=0.05. This smearing is used for the rest of the thesis for all calculations.

When doing the DoS calculations non-spherical contributions to the density gradient in the PAW spheres was included (LASPH = .TRUE.) and LMAXMIX=4 was used to obtain fast convergence. For the spin polarized calculations the magnetic moments were initialised as  $1 \mu_B$  for all atoms in the unit cell. The DoS plots were made using SUMO software

[195]: Ganose et al. (2018), *sumo: Command-line tools for plotting and analysis of periodic \*ab initio\* calculations*

[195].



## A.2 Chapter 4

The structures used in this chapter and later were initially obtained from Materials Project [194] and relaxed using PBE+U. The U parameter was taken from literature and is different for each material, and the reasoning behind the choice of each U parameter is described in the main body. The U parameter was only applied to the TM 3d orbitals.

The relaxation was done without any symmetry constraints and with a well converged basis set (Encut = 1000eV) and a regular gamma centred k-point grid of (8x8x8) for the Cubic structures, the k-point grid for the distorted structures was scaled according to real space dimension compared to the cubic structures. For the relaxation the magnetic moments were initialised as  $1 \mu_B$  for all atoms in the computational cell, but they are not constrained to this value throughout the Kohn-Sham self-consistent cycle. The structures were converged till all the forces were less than  $10^{-4} eV/\text{angstrom}$ .

After that the main calculations were run with the same k-point grids but with a plane wave cut-off energy of 600eV. For these calculations the magnetic moments were initialised only for the transition metal atoms with all the other atom initial magnetic moments set to zero. The initialised magnetic moments were 20% to 30% higher than those of the largest expected magnetic moment for each constituent material. This expectation was based on the high spin filling of the 3d orbitals in octahedral splitting  $t_{2g}$  and  $e_g$ .

As the HSE06 calculation are very computationally costly it was decided to use PRECFOCK=Fast for all HSE06 calculations.

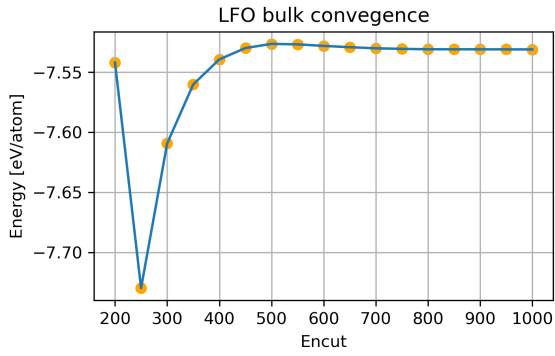
For the LOBSTER projection, the basis functions used were:

- ▶ O 2s 2p<sub>y</sub> 2p<sub>z</sub> 2p<sub>x</sub>
- ▶ La 5s 6s 5p<sub>y</sub> 5p<sub>z</sub> 5p<sub>x</sub> 5d<sub>xy</sub> 5d<sub>yz</sub> 5d<sub>z<sup>2</sup></sub> 5d<sub>xz</sub> 5d<sub>x<sup>2</sup>-y<sup>2</sup></sub>
- ▶ Ni 4s 3d<sub>xy</sub> 3d<sub>yz</sub> 3d<sub>z<sup>2</sup></sub> 3d<sub>xz</sub> 3d<sub>x<sup>2</sup>-y<sup>2</sup></sub>
- ▶ Fe 4s 3d<sub>xy</sub> 3d<sub>yz</sub> 3d<sub>z<sup>2</sup></sub> 3d<sub>xz</sub> 3d<sub>x<sup>2</sup>-y<sup>2</sup></sub>
- ▶ Co 4s 3d<sub>xy</sub> 3d<sub>yz</sub> 3d<sub>z<sup>2</sup></sub> 3d<sub>xz</sub> 3d<sub>x<sup>2</sup>-y<sup>2</sup></sub>

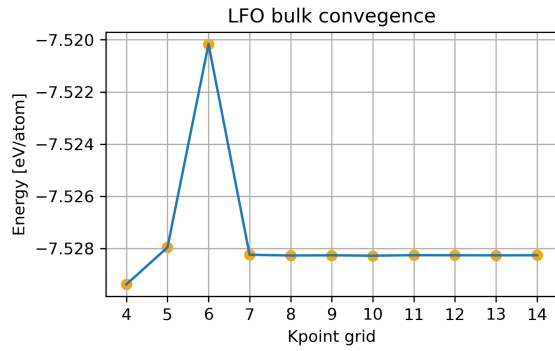
This meant that there were at least 28 bands needed per formula unit of  $ABO_3$  of calculation.

The convergence plots of  $LaFeO_3$ ,  $LaCoO_3$  and  $LaNiO_3$  are visible in figures A.2,A.3 and A.4 respectively.

To obtain detailed DoS for the PES spectra comparison, the number of DoS points generated was increased from the default 301 to 1000 (NEDOS = 1000).

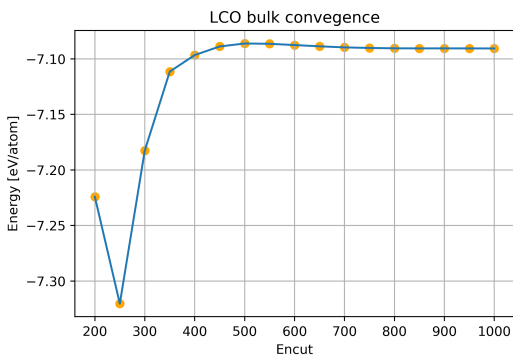


(a) Energy convergence

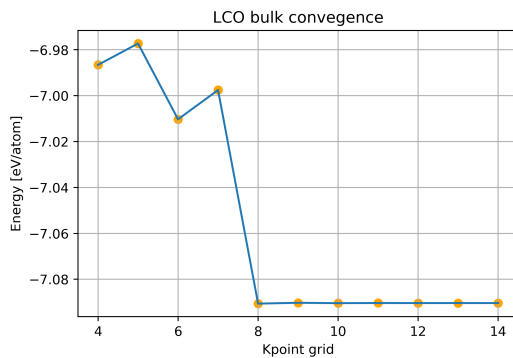


(b) K-point grid convergence

Figure A.2: Convergence graphs of the  $LaFeO_3$  cubic structure.

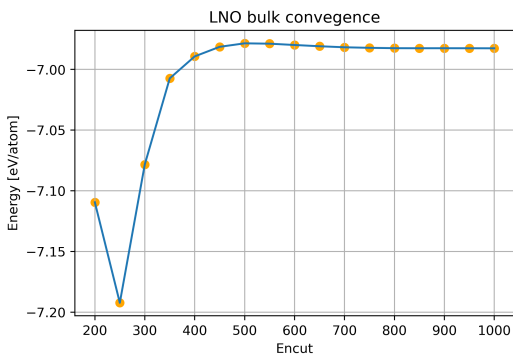


(a) Energy convergence

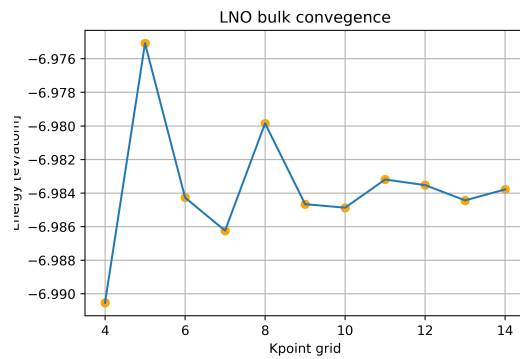


(b) K-point grid convergence

Figure A.3: Convergence graphs of the  $LaCoO_3$  cubic structure.



(a) Energy convergence



(b) K-point grid convergence

Figure A.4: Convergence graphs of the  $LaCoO_3$  cubic structure.

### A.2.1 Magnetic ordering of $LaNiO_3$

The magnetic ordering of cubic  $LaNiO_3$  was investigated for a  $2 \times 2 \times 2$  cubic supercell structure. This is done in light of strange results of Ch.5. The results can be seen in table A.1.

Magnetic ordering for the Cubic LNO superstructure			
Initialised ordering	Final ordering	$\Delta$ per f.u. [meV]	Mag. per f.u.
AFM-A	Ferrimagnetic	5	0.2
FM	FM	0.0	1.0
AFM-C	AFM-C	17	0.0
AFM-D	AFM-D	10	0.0
AFM-E	AFM-A	10	0.0
AFM-F	AFM-F	6	0.0
AFM-G	FM	13	0.3
Non-magnetic	Ferrimagnetic	5	0.4

**Table A.1:** The magnetic ordering test results for the cubic  $2 \times 2 \times 2$  LNO super-cell. Here the initialised magnetic ordering is compared to the final one. Energy is given with respect to lowest energy ordering (FM in this case) and per 5 atoms. Magnetisation shown is the total magnetisation per 5 atoms.

Based on the results seen in the table A.1, in chapters 4, 5 and 6  $LaNiO_3$  is always initialized using FM magnetic ordering since this is the lowest-energy ordering of the cubic and  $R\bar{3}c$   $LaNiO_3$  structures.

## A.3 Chapter 5

Most materials have a positive Poisson's ratio and are therefore expected to expand vertically if compressed horizontally (and shrink vertically if stretched horizontally). So, in another bid to save computational time, the unit cells are pre-relaxed with their new in plane lattice parameter constrains before they are used to construct the superstructures. This relaxation is only done in the vertical direction and only volumetrically (meaning that the relative positions of the atoms remains unchanged). This relaxation is done on the simple cubic unit cells each consisting of 5 atoms.

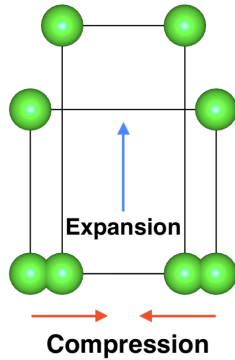


**Figure A.5:** An illustration of unit cell vertical expansion upon horizontal compression expected from a material with a positive Poisson's ratio.

The magnetic moment was initialised as  $1 \mu_B$  on all transition metal ions with  $0 \mu_B$  for all other atoms for this relaxation step. The cut-off energy used was 1000 eV and the same converged k-point grids seen in Ch.4 were used.

### A.3.1 $LaNiO_3$ - $LaCoO_3$ interface vertical relaxation

The averaged lattice parameter of the cubic structures of  $LaNiO_3$  and  $LaCoO_3$  is 3.827 Å. This was then set as the in-plane lattice parameter for both  $LaNiO_3$  and  $LaCoO_3$  and the cells were relaxed. The resultant out of plane lattice parameters and volumes can be found in table A.2.

**Table A.2:** The out of plane relaxed unit cell volumes and lattice parameters of  $LaCoO_3$  and  $LaNiO_3$ .

LNO-LCO interface					
Material	Unit cell volume			New Lattice parameters	
	Starting	After relaxation	Difference %	In plane	Out of plane
LaCoO3	55.46	56.23	1.38%	3.827	3.839
LaNiO3	56.62	56.64	0.02%		3.867

The  $LaCoO_3$  out of plane lattice parameter increased together with the increase of the in-plane one, indicating negative Poisson's ratio for this material.

This vertical expansion gives way to tetragonal distortion in the upwards direction, it was shown in Chapter 4 that this leads to magnetic behaviour of the Co atoms. This is confirmed as the octahedral ratio presented there is now 1.003 and consistent with the data shown in figure 4.18 (a).

The lowest energy configuration for the  $LaCoO_3$  unit cell is now magnetic, as shown in table A.3, the magnetic configuration is 0.219 eV lower in energy, this matches observations in figure 4.18(b).

In conjunction with the previous changes the charge state also exhibits differences. The extent of these changes can be seen in table A.3.

**Table A.3:** The change in local magnetisation and oxidation state of the Co ion in various structures. The first two structures are the vertically relaxed unit cells and the last one is the simple cubic reference from Chapter 4.

Changes exhibited	Oxi state			Magnetic moment		
	WZ	Bader	Loewdin	Total	WZ	Loewdin
LaCoO magnetic	0.71	1.51	1.34	2	2.1	2.07
LaCoO non-magnetic	0.69	1.47	1.25	0	0	0
LaCoO cubic reference	0.65	1.47	1.25	0	0	0

The relaxed  $LaNiO_3$  unit cell did not exhibit any changes in charge or magnetism upon relaxation.

### A.3.2 $LaNiO_3$ - $LaFeO_3$ interface vertical relaxation

The average lattice parameter of the  $LaFeO_3$  and  $LaNiO_3$  combination is 3.891 Å. The simple cubic structures were constrained in plane to this new parameter and relaxed, with the overview of these results visible in table A.4.

LNO-LFO interface					
Material	Unit cell volume			New Lattice parameters	
	Starting	After relaxation	Difference %	In plane	Out of plane
LaFeO3	61.21	62.95	2.83%	3.891	4.053
LaNiO3	56.62	56.72	0.18%		3.747

**Table A.4:** The out of plane relaxed unit cell volumes and lattice parameters of  $LaFeO_3$  and  $LaNiO_3$ .

While there is no change in magnetisation for either material, there is difference in oxidation states. These changes are shown in table A.5.

Changes in oxidation state			
	WZ	Bader	Löwdin
LaFeO	1.04	1.8	1.72
LaFeO cubic reference	1.05	1.77	1.71
LaNiO	0.65	1.43	1.3
LaNiO cubic reference	0.65	1.4	1.33

**Table A.5:** The exhibited change in oxidation states after vertical relaxation for both the  $LaFeO_3$  and  $LaNiO_3$  unit cells. The cubic references are taken from Chapter 4.

### A.3.3 Magnetic ordering

The computational structure used in Ch. 5 has TM atoms arranged in a linear fashion. This arrangement of TM atoms can represent only two magnetic orderings - AFM-A and FM. As FM or AFM-A are not the preferred magnetic orderings for  $LaCoO_3$  and  $LaFeO_3$  the magnetic ordering combinations are tested explicitly. This is done with the 4+4 unrelaxed unit cells.

#### $LaNiO_3$ - $LaCoO_3$

The results are shown in table A.6, We find that for all instances the local magnetic moment of Co was quenched. The initialised ordering is noted as  $LaCoO_3$  first and then  $LaNiO_3$ .

Initialised ordering ( $LaNiO_3$ - $LaCoO_3$ )	Converged to	$\Delta E_n$ per f.u. [meV]
AFM	AFM Ni	13
AFM-FM	FM Ni	0.0
FM	Ferrimagnetic	7
FM- (-FM)	FM Ni	0.0
FM-AFM	AFM Ni	13

**Table A.6:** The magnetic ordering combinations and their energies with respect to the ground state. The Co local magnetic moment was always found to be zero. The (-FM) denotes Ferromagnetic ordering of opposite sign.

In the table A.6 above, it can be seen that the Ni does converge to ferrimagnetic or AFM solution depending on the initialised spin ordering. These orderings are higher in energy compared FM one so they are not used.

The final magnetic ordering initialised in the the LNO-LCO interfacial structure for this chapter is FM - (-FM).

### *LaNiO<sub>3</sub>-LaFeO<sub>3</sub>*

The same test is performed for the *LaNiO<sub>3</sub>-LaFeO<sub>3</sub>* interfacial superstructure. The results of this test are displayed in table A.7.

The results from Chapter 4 indicate that AFM-A is the least favourable anti ferromagnetic spin ordering of the ones tested for *LaFeO<sub>3</sub>*. Here in all cases the AFM ordering converged to a Ferrimagnetic - like solution with seemingly no order and a mix of of high and low spin Fe atoms, meanwhile the FM ordering was had only low spin Fe atoms present ( $\approx 1 \mu_B$  per Fe atom). The local magnetic moments of all the Co atoms were again quenched.

**Table A.7:** The magnetic ordering test for the *LaNiO<sub>3</sub>-LaFeO<sub>3</sub>* interface. Here all the AFM orderings converged to Ferrimagnetic ones with low-high spin, and FM was low spin.

Initialised ordering ( <i>LaNiO<sub>3</sub>-LaFeO<sub>3</sub></i> )	$\Delta E_n$ per f.u. [eV]
AFM	0.154
AFM-FM	0.235
FM	0.498
FM- (-FM)	0.000
FM-AFM	0.155

A notable observation is that the Ferrimagnetic orderings with a larger percentage of Higher spin Fe atoms were more energetically favourable

The magnetic ordering initialised in the the *LaNiO<sub>3</sub>-LaFeO<sub>3</sub>* interfacial structure for this chapter is FM - (-FM).

### **A.3.4 HSE06 results for *LaNiO<sub>3</sub>-LaCoO<sub>3</sub>***

The 6+6 interfacial structure was also converged with HSE06, in a bid to improve representation. The results are displayed in figure A.6. Only Bader results are available as there was not enough memory to compute all the bands for a Löwdin projection.

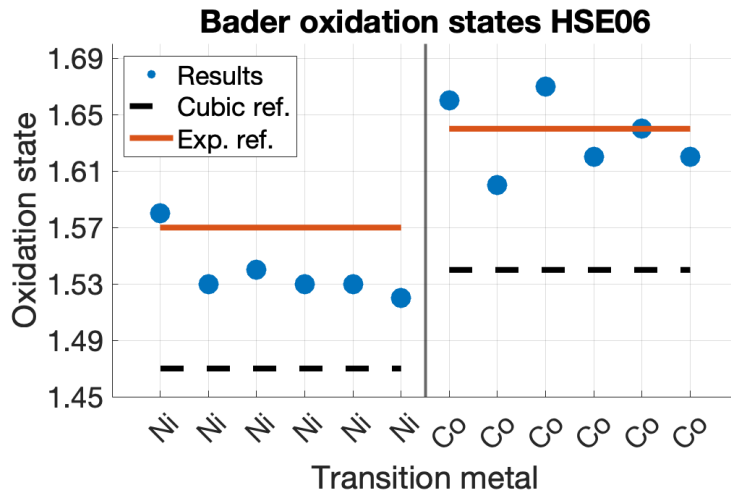


**Figure A.6:**  $LaNiO_3$ - $LaCoO_3$  interfacial structure Bader Oxidation states. The oxidation states displayed are those of the transition metals, with the black line indicating the interface. The experimental structure oxidation state for Co is that of the FM HSE06  $R\bar{3}c$  calculation.

These results show that the representation of these materials in this structure is bad.



## A.4 Chapter 6

Here the unit cell pre-convergence is explored in the same way as for chapter 5. But in this case the lattice parameter is pinned to the one of STO (3.905 Å). After relaxation all the slabs are made with the pymatgen package slab module [196].

### A.4.1 Vertical relaxation of $LaNiO_3$

The unit cell is relaxed in the same vain as in Chapter 5,

LaNiO3 changes	Volume	Out of plane parameter	Bader oxidation state	Lowdin oxidation state
After vertical relaxation	57.71	3.784	1.42	1.28
Cubic reference	56.62	3.840	1.4	1.33
Difference	2%	-1%	1%	-4%

The changes are displayed in table ???. The Bader oxidation state increased while the Löwdin oxidation state decreased.

The out of plane lattice parameter is in line with literature predictions of the Poisson ratio as can be seen with the orange dotted line in fig. 6.3 calculated with ratio from [197].

### A.4.2 Vertical relaxation of $LaFeO_3$

Again the in-plane strained unit cell is relaxed vertically.

LaFeO3 changes	Volume	Out of plane parameter	Bader oxidation state	Lowdin oxidation state
After vertical relaxation	61.22	4.015	1.8	1.72
Cubic reference	61.21	3.927	1.77	1.71
Difference	0.02%	2%	2%	1%

The increases in the lattice parameter is larger than in the experimental case (0.4%), but it is still in the same trend. Both oxidation states increased.

### A.4.3 Vertical relaxation of $LaCoO_3$

The in-plane strained unit cell is again allowed to relax.

LaCoO3 changes	Volume	Out of plane parameter	Bader oxidation state	Lowdin oxidation state	Magnetisation
After vertical relaxation	55.37	3.794	1.52	1.34	2.1
Cubic reference	55.46	3.820	1.47	1.25	0
Difference	0%	-1%	3%	7%	NaN

Just as in Ch.5, changes in Löwdin projected oxidation state and local magnetisation are seen

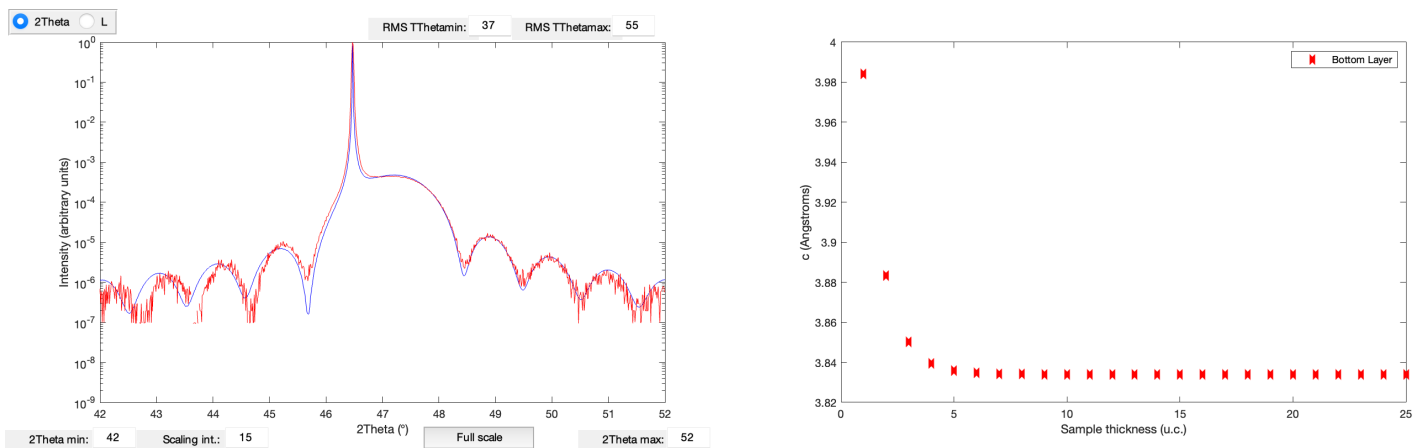
### A.4.4 XRD result fitting

There were experimental XRD results available of a 25 unit cell stack of  $LaNiO_3$  deposited onto a  $SrTiO_3$  substrate, and results of a stack consisting of 4 unit cells of  $LaCoO_3$  on top of a 25 unit cell stack of  $LaNiO_3$  deposited onto a  $SrTiO_3$  substrate. These were analysed using the *InteractiveXRDFit* software by Céline Lichtensteiger [198], with the atomic scattering factors for each atom taken from the International Tables for Crystallography [199].

First the 25 unit cell stack of  $LaNiO_3$  deposited onto a  $SrTiO_3$  substrate was analysed. The resultant out of plane lattice parameter was found to be 3.8341 Å. With the exact fit along the z axis being  $0.15e^{z/-0.9} + 3.843$ . The immediate fit results are seen in figure A.7. The large increase of out of plane parameter at the base is rather un-physical, and most likely has to do with defects in the measured structure.

[198]: Lichtensteiger (2018), *InteractiveXRDFit: a new tool to simulate and fit X-ray diffractograms of oxide thin films and heterostructures*

[199]: Brown et al. (2006), *Intensity of diffracted intensities*



(a) Measured (red) and simulated (blue) spectra comparison

(b) The out of plane lattice parameter as a function of height z.

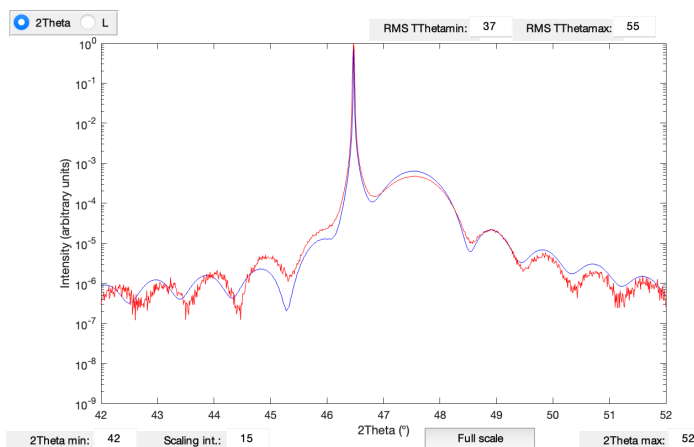
**Figure A.7:** XRD fit results for 25 u.c. of  $LaNiO_3$ , deposited on a  $SrTiO_3$  substrate.

Next the total layer stack of 4 u.c. of  $LaCoO_3$  on top of a 25 unit cell stack of  $LaNiO_3$  was fitted. The final result was an average out of plane lattice parameter of 3.8166 Å for  $LaNiO_3$  and 3.7836 Å for  $LaCoO_3$ . With the exact fits along the z axis being  $0.1e^{z/-1.8} + 3.826$  and  $0.003e^{z/2} + 3.791$  respectively. The fit results can be seen in figure A.8.

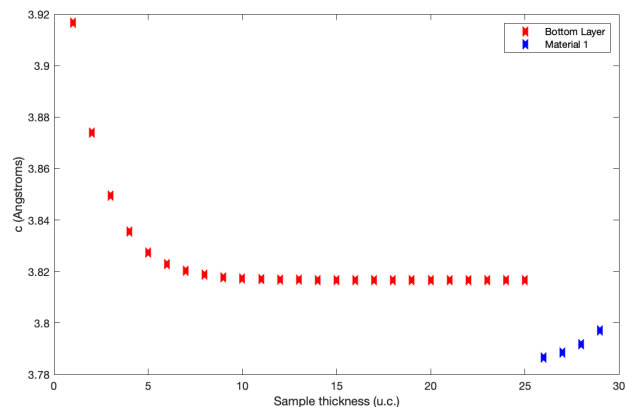
The fits seem un-physical indicating a  $LaNiO_3$  lattice parameter that is too small compared to experiment and a  $LaCoO_3$  lattice parameter that is too large. This is most likely due to the fact that this simple software does not account for surface distortions and the fact that the spectra is made of co-joined thickness's and gradients, thus being prone to fits that reproduce the spectra but have lost physical meaning, as there are too many interacting parameters. This result was not used in the body, as it was deemed un-physical.

### A.4.5 Slab relaxation issues

It was not possible to relax the structures fully. In the first case, because of the constrained atoms in the first monolayer and in the second case because of the residual strain at the interface. An example plot of mean



(a) Measured (red) and simulated(blue) spectra comparison

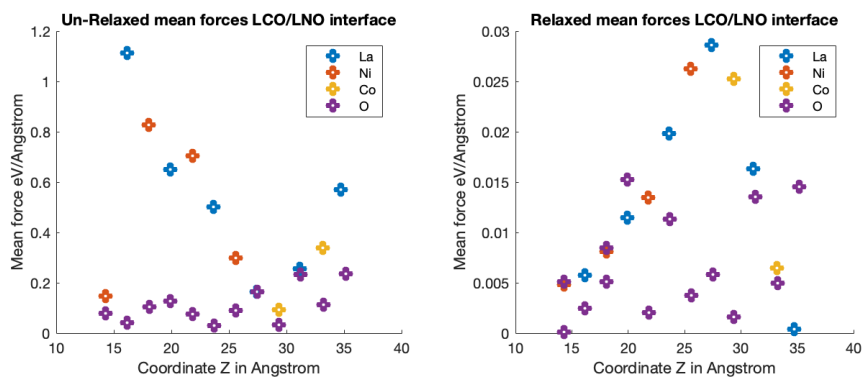


(b) The out of plane lattice parameter as a function of height z.

Figure A.8: XRD fit results for 4 u.c. of  $LaCoO_3$  on top of 25 u.c. of  $LaNiO_3$ , deposited on a  $SrTiO_3$  substrate.

absolute xyz forces of the second relaxation type can be seen in figure A.9. Note that initial forces are reduced by  $\approx 30$  fold, so this structure can be considered as relaxed as the residual interface stress is physical. Similar behaviour is also seen in the other relaxation type of structures.

Figure A.9: The mean absolute xyz forces on each atom as a function of their z coordinate illustrating residual stress at the interface.



# B

## Work functions and experiments

Here the work functions of the materials are discussed. It was intended to measure the work functions of the individual materials as deposited by PLD and then the work functions of the experimental structures. It was however not possible to do so and there are only limited results of the experiments. The work functions were only determined for  $LaFeO_3$ ,  $LaCoO_3$  and  $LaNiO_3$ .

To determine work functions of the materials one has to know the Fermi level of the material and what the vacuum reference potential is. The Fermi level is readily available in VASP output files. The reference potential is obtained by adding vacuum on both sides of the cells creating a surface. It was decided to use 25 Å of vacuum for all the cells and only converge the cell size. The relaxed cubic unit cells (seen in Ch.4) of each material were used.

An example of such cells with vacuum is seen in figure B.1. These structures are made in a way where for each material there is an exposed TM-O terminated surface and a La-O terminated surface as it is expected that the two surfaces produce a different work function.

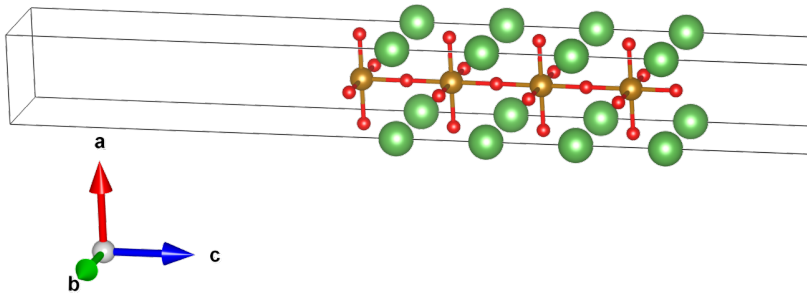


**Figure B.1:** Cubic  $LaFeO_3$  cells with 25 Å of vacuum added.

As it was found, the slabs constructed are polarised due to the different terminations, which means that dipole corrections have to be used to obtain a stable vacuum reference. The impact of such corrections is seen in figure B.2.

In the end the settings used to obtain the work functions were as follows:

1. LDIPOL = .TRUE. - Enable corrections to forces, energy and potential due to dipole.
2. IDIPOL=3 - Dipole corrections in the z direction only
3. DIPOL = 0.5 0.5 0.5 - Calculate from the center of the cell
4. LVTOT = .TRUE. - Determine the total local potential (in eV)
5. LVHAR = .TRUE. - Add Hartree potentials

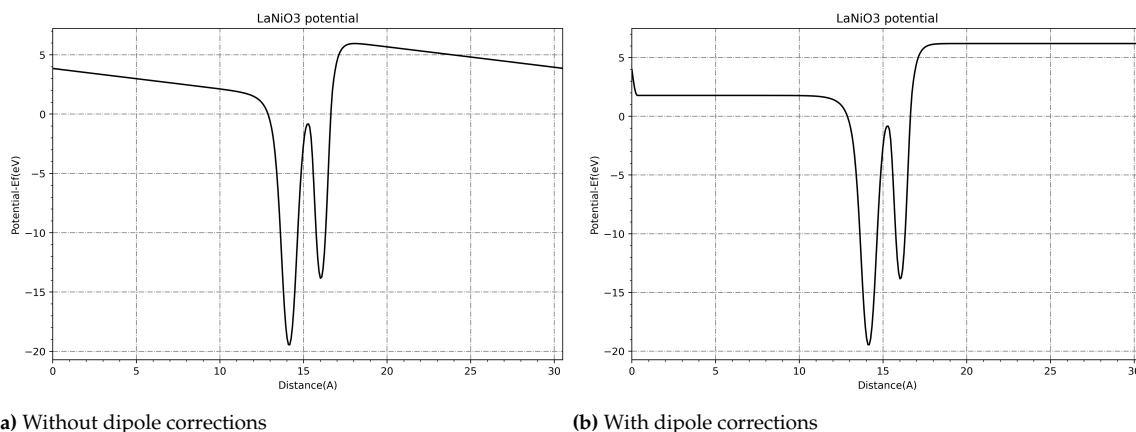


**Figure B.2:** The X-Y averaged potential along the z axis of a  $LaNiO_3$  structure with vacuum. It shows the impact of dipole corrections, as the structure on the left does not use dipole corrections but the structure on the right does.

Structures of different height for each material were converged using PBE+U, and the work functions extracted. The results can be seen in figures B.3, B.4 and B.5. There are missing data points in figure B.3, as those structures did not converge.

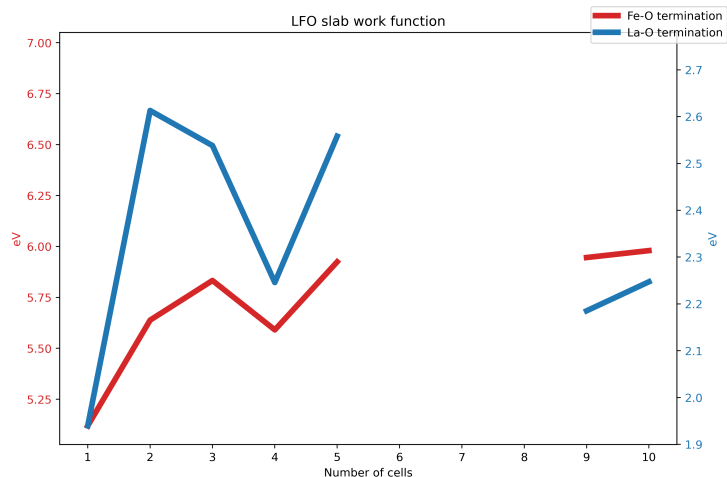


**Figure B.3:**  $LaFeO_3$  structure work function convergence.

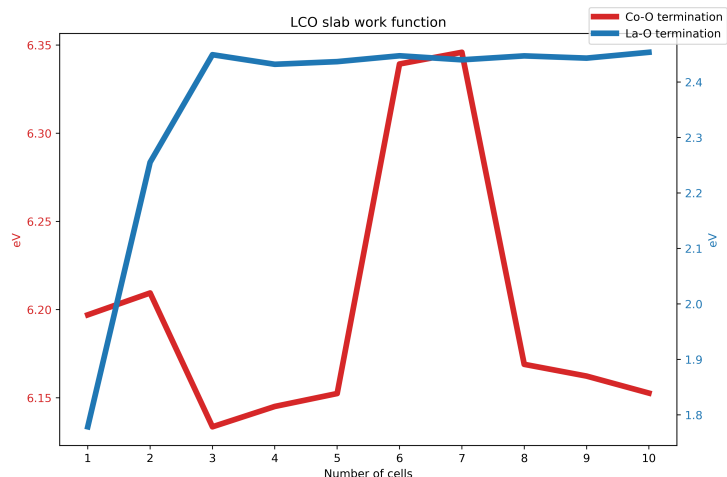


**Figure B.4:**  $LaCoO_3$  structure work function convergence.

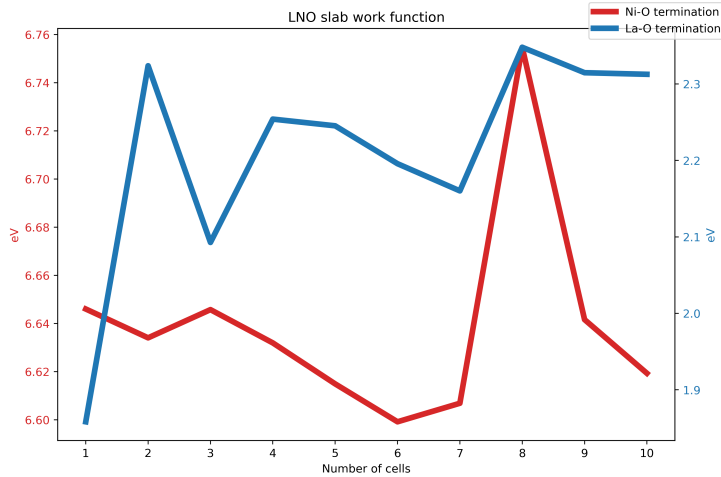


**Figure B.5:**  $LaNiO_3$  structure work function convergence.

If the clear outliers are excluded it seems that the Fe-O termination has a work function of 5.9 eV, the Co-O termination a work function of 6.15 eV and the Ni-O termination a work function of 6.62 eV. In all cases the La-O termination has a work function of 2.3-2.5 eV.

There were KPFM (Kelvin Probe Force Microscopy) preformed at a Park tools Park NX10 AFM tool and the Bruker AFM tool using an ARROW EFM-10 tip. These are conductive PtIr5 coated tips 10  $\mu m$  in length (hence the 10 in the name).

The final work functions are obtained by comparing the potential with reference to the potential of the working tip [200]:

$$\phi_{sample} = \phi_{tip} - eV_{measured} \quad (B.1)$$

The working potential of the tip is found by comparing it to a HOPG (Highly oriented pyrolytic graphite) a material with a known work function of 4.6 eV. The experimental working protocol was taken over from the Park tools NX10 tool operator - Nynke S. Wijnant MSc.

This protocol is :

- ▶ Measure the Al-Au reference sample
- ▶ Peel and measure the HOPG reference sample
- ▶ Measure a sample
- ▶ Peel and measure the HOPG reference sample
- ▶ Calculate the sample work function using the average tip potential of the two HOPG measurements, one before the other one after.
- ▶ Repeat for each sample
- ▶ At the end measure the Al-Au reference sample again and check for drift

Such a protocol is needed as the Work function of HOPG depends on the time difference between measurement and peeling. It was also found that the Al-Au reference sample was old, and therefore the work functions had changed due to surface ageing. Due to time limitations of a single session it was not always possible to re-measure the HOPG before each sample and it was also not always possible to measure the last HOPG sample.

The work functions were measured in two sessions. In one session the LCO and LFO were measured on the Bruker AFM, in the other the LNO on the Park tool AFM. Measuring materials in different sessions and on different tools is known to cause differences in measurement.

The work functions of  $LaNiO_3$  were measured to be 5.45eV, the Work function of  $LaCoO_3$  was measured to be 4.61 eV and the work function of  $LaFeO_3$  was found to be 3.87 eV. When compared to the calculated values, the trend of increasing work function from Fe-O termination to Ni-O termination is there but the values are off by a scaling factor of 1.4. If rescaled, the calculated values match the experimentally obtained ones.

<b>Work function comparison [eV]</b>		
	Calculated	Measured
$LaFeO_3$	5.9	3.87
$LaCoO_3$	6.15	4.61
$LaNiO_3$	6.62	5.45

# Bibliography

Here are the references in citation order.

- [1] John O'M. Bockris. 'Hydrogen no longer a high cost solution to global warming: New ideas'. In: *International Journal of Hydrogen Energy* 33.9 (2008), pp. 2129–2131. doi: <https://doi.org/10.1016/j.ijhydene.2008.02.030> (cited on page 1).
- [2] Jin Suntivich et al. 'A Perovskite Oxide Optimized for Oxygen Evolution Catalysis from Molecular Orbital Principles'. In: *Science* 334.6061 (2011), pp. 1383–1385. doi: [10.1126/science.1212858](https://doi.org/10.1126/science.1212858) (cited on pages 1, 3).
- [3] J. S. Griffith and L. E. Orgel. 'Ligand-field theory'. In: *Q. Rev. Chem. Soc.* 11 (4 1957), pp. 381–393. doi: [10.1039/QR9571100381](https://doi.org/10.1039/QR9571100381) (cited on page 1).
- [4] H. Bethe. 'Termaufspaltung in Kristallen'. In: *Annalen der Physik* 395.2 (1929), pp. 133–208. doi: <https://doi.org/10.1002/andp.19293950202> (cited on page 1).
- [5] J. H. Van Vleck. 'Theory of the Variations in Paramagnetic Anisotropy Among Different Salts of the Iron Group'. In: *Phys. Rev.* 41 (2 July 1932), pp. 208–215. doi: [10.1103/PhysRev.41.208](https://doi.org/10.1103/PhysRev.41.208) (cited on page 1).
- [6] Thomas Wolfram and Sinasi Ellialtioglu. *Electronic and optical properties of d-band perovskites*. Cambridge University Press, 2006 (cited on page 1).
- [7] B.N. Figgis and M.A. Hitchman. *Ligand Field Theory and Its Applications*. Special Topics in Inorganic Chemistry. Wiley, 2000 (cited on pages 2, 41).
- [8] F Albert Cotton. *Chemical applications of group theory*. John Wiley & Sons, 1991 (cited on page 2).
- [9] John B. Goodenough. 'Metallic oxides'. In: *Progress in Solid State Chemistry* 5 (1971), pp. 145–399. doi: [https://doi.org/10.1016/0079-6786\(71\)90018-5](https://doi.org/10.1016/0079-6786(71)90018-5) (cited on page 2).
- [10] Isabela C. Man et al. 'Universality in Oxygen Evolution Electrocatalysis on Oxide Surfaces'. In: *ChemCatChem* 3.7 (Mar. 2011), pp. 1159–1165. doi: [10.1002/cctc.201000397](https://doi.org/10.1002/cctc.201000397) (cited on page 2).
- [11] Asha Raveendran, Mijun Chandran, and Ragupathy Dhanusuraman. 'A comprehensive review on the electrochemical parameters and recent material development of electrochemical water splitting electrocatalysts'. In: *RSC Advances* 13.6 (2023), pp. 3843–3876. doi: [10.1039/d2ra07642j](https://doi.org/10.1039/d2ra07642j) (cited on page 3).
- [12] Sergio Trasatti. 'Electrocatalysis by oxides — Attempt at a unifying approach'. In: *Journal of Electroanalytical Chemistry and Interfacial Electrochemistry* 111.1 (1980), pp. 125–131. doi: [https://doi.org/10.1016/S0022-0728\(80\)80084-2](https://doi.org/10.1016/S0022-0728(80)80084-2) (cited on page 3).
- [13] John O'M. Bockris and Takaaki Otagawa. 'The Electrocatalysis of Oxygen Evolution on Perovskites'. In: *Journal of The Electrochemical Society* 131.2 (Feb. 1984), pp. 290–302. doi: [10.1149/1.2115565](https://doi.org/10.1149/1.2115565) (cited on page 3).
- [14] Wesley T. Hong et al. 'Toward the rational design of non-precious transition metal oxides for oxygen electrocatalysis'. In: *Energy Environmental Science* 8.5 (2015), pp. 1404–1427. doi: [10.1039/c4ee03869j](https://doi.org/10.1039/c4ee03869j) (cited on page 3).
- [15] Zhicheng Zhong and Philipp Hansmann. 'Band Alignment and Charge Transfer in Complex Oxide Interfaces'. In: *Phys. Rev. X* 7 (1 Mar. 2017), p. 011023. doi: [10.1103/PhysRevX.7.011023](https://doi.org/10.1103/PhysRevX.7.011023) (cited on pages 4, 5, 27, 59, 68, 70, 81, 82, 86, 87).
- [16] M. Cwik et al. 'Crystal and magnetic structure of LaTiO<sub>3</sub> : evidence for non-degenerate  $t_{2g}$ -orbitals'. In: *published in Physical Review B Rapid Communication* 68 (2003), p. 060401. doi: <https://doi.org/10.1103/PhysRevB.68.060401> (cited on page 5).
- [17] A. D. Rata et al. 'Lattice structure and magnetization of LaCoO<sub>3</sub> thin films'. In: *The European Physical Journal B* 76.2 (2010), pp. 215–219. doi: [10.1140/epjb/e2010-00203-6](https://doi.org/10.1140/epjb/e2010-00203-6) (cited on page 5).



- [18] Josée E. Kleibeuker. 'Reconstructions at complex oxide interfaces'. English. PhD Thesis - Research UT, graduation UT. Netherlands: University of Twente, Mar. 2012. DOI: [10.3990/1.9789036533201](https://doi.org/10.3990/1.9789036533201) (cited on pages 6, 29).
- [19] Jaap Geessinck. 'Charge transfer at the interface between complex oxide thin films'. English. PhD thesis. Netherlands: University of Twente, Oct. 2020. DOI: [10.3990/1.9789036549936](https://doi.org/10.3990/1.9789036549936) (cited on pages 6, 9).
- [20] Georgios Araizi-Kanoutas et al. 'Co valence transformation in isopolar LaCoO<sub>3</sub>/LaTiO<sub>3</sub> perovskite heterostructures via interfacial engineering'. In: *Phys. Rev. Mater.* 4 (2 Feb. 2020), p. 026001. DOI: [10.1103/PhysRevMaterials.4.026001](https://doi.org/10.1103/PhysRevMaterials.4.026001) (cited on pages 6, 7, 29).
- [21] F. Groot and A. Kotani. *Core level spectroscopy of solids*. Jan. 2008, pp. 1–491 (cited on page 6).
- [22] Bruce Ravel. *Introduction to X-ray Absorption Spectroscopy Introduction to X-ray Absorption Spectroscopy*. Sept. 2015 (cited on page 6).
- [23] A. N. Vasiliev et al. 'Valence states and metamagnetic phase transition in partially B-site-disordered perovskite EuMn<sub>0.5</sub>Co<sub>0.5</sub>O<sub>3</sub>'. In: *Phys. Rev. B* 77 (10 Mar. 2008), p. 104442. DOI: [10.1103/PhysRevB.77.104442](https://doi.org/10.1103/PhysRevB.77.104442) (cited on page 7).
- [24] Wikimedia Commons. *Transitions that contribute to X-Ray Absorption edges*. File: XASEdges.svg. 2009. URL: <https://commons.wikimedia.org/wiki/File:XASEdges.svg> (cited on page 7).
- [25] Bradley H Frazer et al. 'The probing depth of total electron yield in the sub-keV range: TEY-XAS and X-PEEM'. In: *Surface Science* 537.1 (2003), pp. 161–167. DOI: [https://doi.org/10.1016/S0039-6028\(03\)00613-7](https://doi.org/10.1016/S0039-6028(03)00613-7) (cited on page 7).
- [26] Philipp Scheiderer et al. 'Tailoring Materials for Mottronics: Excess Oxygen Doping of a Prototypical Mott Insulator'. In: *Advanced Materials* 30.25 (2018), p. 1706708. DOI: <https://doi.org/10.1002/adma.201706708> (cited on page 7).
- [27] Dechao Meng et al. 'Strain-induced high-temperature perovskite ferromagnetic insulator'. In: *Proceedings of the National Academy of Sciences* 115.12 (2018), pp. 2873–2877. DOI: [10.1073/pnas.1707817115](https://doi.org/10.1073/pnas.1707817115) (cited on page 7).
- [28] Rick Webb. *Transmission Electron Microscopy Training*. Microscopy Australia. Room 234, Madsen Building F09 The University of Sydney NSW 2006, 2006 (cited on page 7).
- [29] J. Verbeeck et al. 'ELECTRON ENERGY LOSS SPECTROMETRY'. In: *Encyclopedia of Analytical Science (Second Edition)*. Ed. by Paul Worsfold, Alan Townshend, and Colin Poole. Second Edition. Oxford: Elsevier, 2005, pp. 324–331. DOI: <https://doi.org/10.1016/B0-12-369397-7/00605-1> (cited on page 8).
- [30] Richard M. Martin. *Electronic Structure: Basic Theory and Practical Methods*. Cambridge University Press, Aug. 2020 (cited on pages 11, 13).
- [31] Klaus Capelle. *A bird's-eye view of density-functional theory*. 2006. URL: <https://arxiv.org/abs/cond-mat/0211443> (cited on page 11).
- [32] Peter E. Blöchl. *Theory and Practice of Density-Functional Theory*. 2011. URL: <https://arxiv.org/abs/1108.1104> (cited on page 11).
- [33] Martin Hilbert and Priscila López. 'The World's Technological Capacity to Store, Communicate, and Compute Information'. In: *Science* 332.6025 (2011), pp. 60–65. DOI: [10.1126/science.1200970](https://doi.org/10.1126/science.1200970) (cited on page 12).
- [34] *Nobel Prize in Chemistry 1998*. Sept. 1998 (cited on page 12).
- [35] P. Hohenberg and W. Kohn. 'Inhomogeneous Electron Gas'. In: *Phys. Rev.* 136 (3B Nov. 1964), B864–B871. DOI: [10.1103/PhysRev.136.B864](https://doi.org/10.1103/PhysRev.136.B864) (cited on page 12).
- [36] W. Kohn and L. J. Sham. 'Self-Consistent Equations Including Exchange and Correlation Effects'. In: *Phys. Rev.* 140 (4A Nov. 1965), A1133–A1138. DOI: [10.1103/PhysRev.140.A1133](https://doi.org/10.1103/PhysRev.140.A1133) (cited on page 13).
- [37] Richard M. Martin. *Electronic Structure: Basic Theory and Practical Methods*. Cambridge University Press, 2004 (cited on page 14).

- [38] John P. Perdew and Karla Schmidt. 'Jacob's ladder of density functional approximations for the exchange-correlation energy'. In: *AIP Conference Proceedings* 577.1 (July 2001), pp. 1–20. doi: [10.1063/1.1390175](https://doi.org/10.1063/1.1390175) (cited on page 15).
- [39] U von Barth and L Hedin. 'A local exchange-correlation potential for the spin polarized case.' In: *Journal of Physics C: Solid State Physics* 5.13 (1972), p. 1629. doi: [10.1088/0022-3719/5/13/012](https://doi.org/10.1088/0022-3719/5/13/012) (cited on page 16).
- [40] D. M. Ceperley and B. J. Alder. 'Ground State of the Electron Gas by a Stochastic Method'. In: *Phys. Rev. Lett.* 45 (7 Aug. 1980), pp. 566–569. doi: [10.1103/PhysRevLett.45.566](https://doi.org/10.1103/PhysRevLett.45.566) (cited on page 17).
- [41] SHANG-KENG MA and KEITH A. BRUECKNER. 'Correlation Energy of an Electron Gas with a Slowly Varying High Density'. In: *Phys. Rev.* 165 (1 Jan. 1968), pp. 18–31. doi: [10.1103/PhysRev.165.18](https://doi.org/10.1103/PhysRev.165.18) (cited on page 17).
- [42] S. H. Vosko, L. Wilk, and M. Nusair. 'Accurate spin-dependent electron liquid correlation energies for local spin density calculations: a critical analysis'. In: *Canadian Journal of Physics* 58.8 (Aug. 1980), 1200 to 1211. doi: [10.1139/p80-159](https://doi.org/10.1139/p80-159) (cited on page 17).
- [43] J. P. Perdew and Alex Zunger. 'Self-interaction correction to density-functional approximations for many-electron systems'. In: *Phys. Rev. B* 23 (10 May 1981), 5048 to 5079. doi: [10.1103/PhysRevB.23.5048](https://doi.org/10.1103/PhysRevB.23.5048) (cited on page 17).
- [44] John P. Perdew et al. 'Understanding band gaps of solids in generalized Kohn–Sham theory'. In: *Proceedings of the National Academy of Sciences* 114.11 (2017), pp. 2801–2806. doi: [10.1073/pnas.1621352114](https://doi.org/10.1073/pnas.1621352114) (cited on page 17).
- [45] John P. Perdew. 'Accurate Density Functional for the Energy: Real-Space Cutoff of the Gradient Expansion for the Exchange Hole'. In: *Phys. Rev. Lett.* 55 (16 Oct. 1985), pp. 1665–1668. doi: [10.1103/PhysRevLett.55.1665](https://doi.org/10.1103/PhysRevLett.55.1665) (cited on page 17).
- [46] John P. Perdew, Kieron Burke, and Matthias Ernzerhof. 'Generalized Gradient Approximation Made Simple'. In: *Phys. Rev. Lett.* 77 (18 Oct. 1996), pp. 3865–3868. doi: [10.1103/PhysRevLett.77.3865](https://doi.org/10.1103/PhysRevLett.77.3865) (cited on page 17).
- [47] C. Filippi, D. J. Singh, and C. J. Umrigar. 'All-electron local-density and generalized-gradient calculations of the structural properties of semiconductors'. In: *Phys. Rev. B* 50 (20 Nov. 1994), pp. 14947–14951. doi: [10.1103/PhysRevB.50.14947](https://doi.org/10.1103/PhysRevB.50.14947) (cited on page 17).
- [48] John P. Perdew, Matthias Ernzerhof, and Kieron Burke. 'Rationale for mixing exact exchange with density functional approximations'. In: *The Journal of Chemical Physics* 105.22 (Dec. 1996), pp. 9982–9985. doi: [10.1063/1.472933](https://doi.org/10.1063/1.472933) (cited on page 18).
- [49] Axel D. Becke. 'Density-functional thermochemistry. III. The role of exact exchange'. In: *The Journal of Chemical Physics* 98.7 (Apr. 1993), 5648 to 5652. doi: [10.1063/1.464913](https://doi.org/10.1063/1.464913) (cited on page 18).
- [50] Axel D. Becke. 'A new mixing of Hartree Fock and local density-functional theories'. In: *The Journal of Chemical Physics* 98.2 (Jan. 1993), pp. 1372–1377. doi: [10.1063/1.464304](https://doi.org/10.1063/1.464304) (cited on page 18).
- [51] Carlo Adamo and Vincenzo Barone. 'Toward reliable density functional methods without adjustable parameters: The PBE0 model'. In: *The Journal of Chemical Physics* 110.13 (Apr. 1999), 6158â–6170. doi: [10.1063/1.478522](https://doi.org/10.1063/1.478522) (cited on page 18).
- [52] Carlo Adamo, Gustavo E. Scuseria, and Vincenzo Barone. 'Accurate excitation energies from time-dependent density functional theory: Assessing the PBE0 model'. In: *The Journal of Chemical Physics* 111.7 (Aug. 1999), pp. 2889–2899. doi: [10.1063/1.479571](https://doi.org/10.1063/1.479571) (cited on page 18).
- [53] Jochen Heyd, Gustavo E. Scuseria, and Matthias Ernzerhof. 'Hybrid functionals based on a screened Coulomb potential'. In: *The Journal of Chemical Physics* 118.18 (May 2003), pp. 8207–8215. doi: [10.1063/1.1564060](https://doi.org/10.1063/1.1564060) (cited on page 18).
- [54] J. Paier et al. 'Screened hybrid density functionals applied to solids'. In: *The Journal of Chemical Physics* 124.15 (Apr. 2006), p. 154709. doi: [10.1063/1.2187006](https://doi.org/10.1063/1.2187006) (cited on page 18).
- [55] Cesare Franchini. 'Hybrid functionals applied to perovskites'. In: *Journal of Physics: Condensed Matter* 26 (May 2014), p. 253202. doi: [10.1088/0953-8984/26/25/253202](https://doi.org/10.1088/0953-8984/26/25/253202) (cited on page 18).

- [56] Benjamin G. Janesko. 'Multiconfigurational Correlation at DFT + U Cost: On-Site Electron–Electron Interactions Yield a Block-Localized Configuration Interaction Hamiltonian'. In: *The Journal of Physical Chemistry A* 128.25 (2024). PMID: 38878060, pp. 5077–5087. doi: [10.1021/acs.jpca.4c02326](https://doi.org/10.1021/acs.jpca.4c02326) (cited on pages 18, 19).
- [57] J. R. Hubbard. 'Electron correlations in narrow energy bands - iv. the atomic representation'. In: *Proceedings of the Royal Society of London. Series A. Mathematical and Physical Sciences* 285 (1403 1965), pp. 542–560. doi: [10.1098/rspa.1965.0124](https://doi.org/10.1098/rspa.1965.0124) (cited on page 18).
- [58] Vladimir I. Anisimov, Jan Zaanen, and Ole K. Andersen. 'Band theory and Mott insulators: Hubbard U instead of Stoner I'. In: *Phys. Rev. B* 44 (3 July 1991), pp. 943–954. doi: [10.1103/PhysRevB.44.943](https://doi.org/10.1103/PhysRevB.44.943) (cited on page 19).
- [59] Vladimir I Anisimov, F Aryasetiawan, and A I Lichtenstein. 'First-principles calculations of the electronic structure and spectra of strongly correlated systems: the LDA+ U method'. In: *Journal of Physics: Condensed Matter* 9.4 (1997), p. 767. doi: [10.1088/0953-8984/9/4/002](https://doi.org/10.1088/0953-8984/9/4/002) (cited on page 19).
- [60] A. I. Liechtenstein, V. I. Anisimov, and J. Zaanen. 'Density-functional theory and strong interactions: Orbital ordering in Mott-Hubbard insulators'. In: *Phys. Rev. B* 52 (8 Aug. 1995), R5467–R5470. doi: [10.1103/PhysRevB.52.R5467](https://doi.org/10.1103/PhysRevB.52.R5467) (cited on page 19).
- [61] S. L. Dudarev et al. 'Electron-energy-loss spectra and the structural stability of nickel oxide: An LSDA+U study'. In: *Phys. Rev. B* 57 (3 Jan. 1998), pp. 1505–1509. doi: [10.1103/PhysRevB.57.1505](https://doi.org/10.1103/PhysRevB.57.1505) (cited on page 19).
- [62] Lei Wang, Thomas Maxisch, and Gerbrand Ceder. 'Oxidation energies of transition metal oxides within the GGA + U framework'. In: *Phys. Rev. B* 73 (19 May 2006), p. 195107. doi: [10.1103/PhysRevB.73.195107](https://doi.org/10.1103/PhysRevB.73.195107) (cited on page 19).
- [63] Peter E. Blöchl. 'Projector augmented-wave method'. In: *Phys. Rev. B* 50 (24 Dec. 1994), pp. 17953–17979. doi: [10.1103/PhysRevB.50.17953](https://doi.org/10.1103/PhysRevB.50.17953) (cited on page 21).
- [64] G. Kresse and D. Joubert. 'From ultrasoft pseudopotentials to the projector augmented-wave method'. In: *Phys. Rev. B* 59 (3 Jan. 1999), pp. 1758–1775. doi: [10.1103/PhysRevB.59.1758](https://doi.org/10.1103/PhysRevB.59.1758) (cited on page 21).
- [65] R. P. Feynman. 'Forces in Molecules'. In: *Phys. Rev.* 56 (4 Aug. 1939), pp. 340–343. doi: [10.1103/PhysRev.56.340](https://doi.org/10.1103/PhysRev.56.340) (cited on page 23).
- [66] Richard FW Bader. 'Atoms in molecules'. In: *Accounts of chemical research* 18.1 (1985), pp. 9–15 (cited on page 24).
- [67] P. W. Atkins and Julio De Paula. *Atkins' Physical chemistry*. 8th ed. Oxford: Oxford University Press, 2006. Chap. xxx, 1064 pages : color illustrations ; 28 cm (cited on page 24).
- [68] W Tang, E Sanville, and G Henkelman. 'A grid-based Bader analysis algorithm without lattice bias'. In: *Journal of Physics: Condensed Matter* 21.8 (2009), p. 084204. doi: [10.1088/0953-8984/21/8/084204](https://doi.org/10.1088/0953-8984/21/8/084204) (cited on page 24).
- [69] Per-Olov Löwdin. 'On the Non-Orthogonality Problem Connected with the Use of Atomic Wave Functions in the Theory of Molecules and Crystals'. In: *The Journal of Chemical Physics* 18.3 (Mar. 1950), pp. 365–375. doi: [10.1063/1.1747632](https://doi.org/10.1063/1.1747632) (cited on page 25).
- [70] Christina Ertural, Simon Steinberg, and Richard Dronskowski. 'Development of a robust tool to extract Mulliken and Löwdin charges from plane waves and its application to solid-state materials'. In: *RSC Adv.* 9 (51 2019), pp. 29821–29830. doi: [10.1039/C9RA05190B](https://doi.org/10.1039/C9RA05190B) (cited on page 25).
- [71] Daniel Sanchez-Portal, Emilio Artacho, and Jose M Soler. 'Projection of plane-wave calculations into atomic orbitals'. In: *Solid State Communications* 95.10 (1995), pp. 685–690. doi: [https://doi.org/10.1016/0038-1098\(95\)00341-X](https://doi.org/10.1016/0038-1098(95)00341-X) (cited on page 25).
- [72] Stefan Maintz et al. 'Analytic projection from plane-wave and PAW wavefunctions and application to chemical-bonding analysis in solids'. In: *Journal of Computational Chemistry* 34.29 (2013), pp. 2557–2567. doi: <https://doi.org/10.1002/jcc.23424> (cited on page 25).

- [73] Fabien Tran and Peter Blaha. 'Accurate Band Gaps of Semiconductors and Insulators with a Semilocal Exchange-Correlation Potential'. In: *Phys. Rev. Lett.* 102 (22 June 2009), p. 226401. doi: [10.1103/PhysRevLett.102.226401](https://doi.org/10.1103/PhysRevLett.102.226401) (cited on page 27).
- [74] Nicola Marzari et al. 'Maximally localized Wannier functions: Theory and applications'. In: *Rev. Mod. Phys.* 84 (4 Oct. 2012), pp. 1419–1475. doi: [10.1103/RevModPhys.84.1419](https://doi.org/10.1103/RevModPhys.84.1419) (cited on page 27).
- [75] Jerry B. Torrance et al. 'Simple and perovskite oxides of transition-metals: Why some are metallic, while most are insulating'. In: *Journal of Solid State Chemistry* 90.1 (1991), pp. 168–172. doi: [https://doi.org/10.1016/0022-4596\(91\)90182-H](https://doi.org/10.1016/0022-4596(91)90182-H) (cited on page 29).
- [76] 'False metals, real insulators, and degenerate gapped metals'. In: (Aug. 2020) (cited on pages 29, 30).
- [77] A. M. Glazer. 'Simple ways of determining perovskite structures'. In: *Acta Crystallographica Section A* 31.6 (1975), pp. 756–762. doi: <https://doi.org/10.1107/S0567739475001635> (cited on page 33).
- [78] Gibin George, Sivasankara Rao Ede, and Zhiping Luo. *Fundamentals of Perovskite Oxides: Synthesis, Structure, Properties and Applications*. CRC Press, Oct. 2020 (cited on page 33).
- [79] C. J. Howard and H. T. Stokes. 'Group-Theoretical Analysis of Octahedral Tilting in Perovskites'. In: *Acta Crystallographica Section B* 54.6 (Dec. 1998), pp. 782–789. doi: [10.1107/S0108768198004200](https://doi.org/10.1107/S0108768198004200) (cited on page 33).
- [80] Fowlie, Jennifer. 'Electronic and structural properties of LaNiO<sub>3</sub>-based heterostructures'. en. PhD thesis. Universite de Geneve, 2018. doi: [10.13097/ARCHIVE-OUVERTE/UNIGE:120334](https://doi.org/10.13097/ARCHIVE-OUVERTE/UNIGE:120334) (cited on pages 33, 38, 46).
- [81] W.C. Koehler and E.O. Wollan. 'Neutron-diffraction study of the magnetic properties of perovskite-like compounds LaBO<sub>3</sub>'. In: *Journal of Physics and Chemistry of Solids* 2.2 (1957), pp. 100–106. doi: [https://doi.org/10.1016/0022-3697\(57\)90095-1](https://doi.org/10.1016/0022-3697(57)90095-1) (cited on pages 33–35, 37–40, 45).
- [82] M. MAREZIO and P. D. Dernier. 'The bond lengths in LaFeO<sub>3</sub>'. In: *Materials Research Bulletin* 6.1 (1971), pp. 23–29. doi: [10.1016/0025-5408\(71\)90155-3](https://doi.org/10.1016/0025-5408(71)90155-3) (cited on pages 34, 35).
- [83] S.E. Dann et al. 'The Effect of Oxygen Stoichiometry on Phase Relations and Structure in the System La<sub>1-x</sub>Sr<sub>x</sub>FeO<sub>3-δ</sub> (0 ≤ x ≤ 1, 0 ≤ δ ≤ 0.5)'. In: *Journal of Solid State Chemistry* 109.1 (1994), pp. 134–144. doi: <https://doi.org/10.1006/jssc.1994.1083> (cited on pages 34, 35).
- [84] A Delmastro et al. 'Synthesis and characterization of non-stoichiometric LaFeO<sub>3</sub> perovskite'. In: *Materials Science and Engineering: B* 79.2 (2001), pp. 140–145. doi: [https://doi.org/10.1016/S0921-5107\(00\)00570-5](https://doi.org/10.1016/S0921-5107(00)00570-5) (cited on pages 34, 35).
- [85] Hideki Taguchi et al. 'Synthesis of perovskite-type (La<sub>1-x</sub>Ca<sub>x</sub>)FeO<sub>3</sub> (0 ≤ x ≤ 0.2) at low temperature'. In: *Materials Research Bulletin* 40.5 (2005), pp. 773–780. doi: <https://doi.org/10.1016/j.materresbull.2005.02.009> (cited on pages 34, 35).
- [86] Geoffrey L. Beausoleil II et al. 'Thermal Expansion of Alkaline-Doped Lanthanum Ferrite Near the Néel Temperature'. In: *Journal of the American Ceramic Society* 97.1 (2014), pp. 228–234. doi: <https://doi.org/10.1111/jace.12625> (cited on pages 34, 35, 40).
- [87] Davis Daniel. 'The Electronic and Thermodynamic Properties of Ca doped LaFeO<sub>3</sub> – A First Principles Study Using Density Functional Theory'. MA thesis. Boise State University, Apr. 2014 (cited on pages 34, 35).
- [88] N. G. Imam et al. 'Correlation between structural asymmetry and magnetization in Bi-doped LaFeO<sub>3</sub> perovskite: a combined XRD and synchrotron radiation XAS study'. In: *Journal of Materials Science: Materials in Electronics* 32.3 (2021), pp. 3361–3376. doi: [10.1007/s10854-020-05084-x](https://doi.org/10.1007/s10854-020-05084-x) (cited on pages 34, 35, 40).
- [89] Sverre M. Selbach et al. 'Non-linear thermal evolution of the crystal structure and phase transitions of LaFeO<sub>3</sub> investigated by high temperature X-ray diffraction'. In: *Journal of Solid State Chemistry* 196 (2012), pp. 249–254. doi: <https://doi.org/10.1016/j.jssc.2012.06.023> (cited on pages 34, 40).
- [90] Hidetoshi Kizaki and Koichi Kusakabe. 'DFT-GGA study of NO adsorption on the LaO (001) surface of LaFeO<sub>3</sub>'. In: *Surface Science* 606.3 (2012), pp. 337–343. doi: <https://doi.org/10.1016/j.susc.2011.10.016> (cited on pages 34, 35).



- [91] Andrew M. Ritzmann et al. 'Ab Initio DFT+U Analysis of Oxygen Vacancy Formation and Migration in  $\text{La}_{1-x}\text{Sr}_x\text{FeO}_{3-\delta}$  ( $x = 0, 0.25, 0.50$ )'. In: *Chemistry of Materials* 25.15 (2013), pp. 3011–3019. doi: [10.1021/cm401052w](https://doi.org/10.1021/cm401052w) (cited on pages 34, 35).
- [92] Zhongqin Yang et al. 'Influence of parameters U and J in the LSDA+U method on electronic structure of the perovskites  $\text{LaMO}_3$  ( $M = \text{Cr, Mn, Fe, Co, Ni}$ )'. In: *Phys. Rev. B* 60 (23 Dec. 1999), pp. 15674–15682. doi: [10.1103/PhysRevB.60.15674](https://doi.org/10.1103/PhysRevB.60.15674) (cited on page 34).
- [93] Igor Shein et al. 'Band structure and the magnetic and elastic properties of  $\text{SrFeO}_3$  and  $\text{LaFeO}_3$  perovskites'. In: *Physics of the Solid State* 47 (Nov. 2005), pp. 2082–2088. doi: [10.1134/1.2131149](https://doi.org/10.1134/1.2131149) (cited on pages 34, 35, 40).
- [94] Yueh-Lin Lee et al. 'Ab initio energetics of  $\text{LaBO}_3(001)$  ( $B = \text{Mn, Fe, Co, and Ni}$ ) for solid oxide fuel cell cathodes'. In: *Phys. Rev. B* 80 (22 Dec. 2009), p. 224101. doi: [10.1103/PhysRevB.80.224101](https://doi.org/10.1103/PhysRevB.80.224101) (cited on pages 34, 35, 40).
- [95] Isaac W Boateng et al. 'A DFT+ U investigation of hydrogen adsorption on the  $\text{LaFeO}_3(010)$  surface'. In: *Physical Chemistry Chemical Physics* 19.10 (2017), pp. 7399–7409 (cited on page 35).
- [96] James M. Rondinelli and Nicola A. Spaldin. 'Structural effects on the spin-state transition in epitaxially strained  $\text{LaCoO}_3$  films'. In: *Phys. Rev. B* 79 (5 Feb. 2009), p. 054409. doi: [10.1103/PhysRevB.79.054409](https://doi.org/10.1103/PhysRevB.79.054409) (cited on pages 36, 42, 44, 45).
- [97] Andrew M. Ritzmann et al. 'Ab initio DFT+U analysis of oxygen transport in  $\text{LaCoO}_3$ : the effect of  $\text{Co}^{3+}$  magnetic states'. In: *J. Mater. Chem. A* 2 (21 2014), pp. 8060–8074. doi: [10.1039/C4TA00801D](https://doi.org/10.1039/C4TA00801D) (cited on pages 36, 44, 45).
- [98] Fred Askham, I. Fankuchen, and Roland Ward. 'The Preparation and Structure of Lanthanum Cobaltic Oxide'. In: *Journal of the American Chemical Society* 72.8 (1950), pp. 3799–3800. doi: [10.1021/ja01164a505](https://doi.org/10.1021/ja01164a505) (cited on pages 36, 37).
- [99] Aaron Wold and Roland Ward. 'Perovskite-Type Oxides of Cobalt, Chromium and Vanadium with Some Rare Earth Elements'. In: *Journal of the American Chemical Society* 76.4 (1954), pp. 1029–1030. doi: [10.1021/ja01633a031](https://doi.org/10.1021/ja01633a031) (cited on pages 36, 37).
- [100] A Ruggiero and R Ferro. 'ORTHO GALLATES OF RARE EARTH ELEMENTS'. In: *Atti accad. nazl. Lincei Rend. Classe sci. fis. mat. e nat.* 17 (July 1, 1954), p. 254 (cited on pages 36, 37).
- [101] Gérard Demazeau, Michel Pouchard, and Paul Hagemüller. 'Sur de nouveaux composés oxygénés du cobalt +III dérivés de la perovskite'. In: *Journal of Solid State Chemistry* 9.3 (1974), pp. 202–209. doi: [https://doi.org/10.1016/0022-4596\(74\)90075-9](https://doi.org/10.1016/0022-4596(74)90075-9) (cited on pages 36, 37).
- [102] G. Thornton, B.C. Tofield, and A.W. Hewat. 'A neutron diffraction study of  $\text{LaCoO}_3$  in the temperature range  $4.2 < T < 1248 \text{ K}$ '. In: *Journal of Solid State Chemistry* 61.3 (1986), pp. 301–307. doi: [https://doi.org/10.1016/0022-4596\(86\)90035-6](https://doi.org/10.1016/0022-4596(86)90035-6) (cited on pages 36, 37, 45).
- [103] P. G. Radaelli and S.-W. Cheong. 'Structural phenomena associated with the spin-state transition in  $\text{LaCoO}_3$ '. In: *Phys. Rev. B* 66 (9 Sept. 2002), p. 094408. doi: [10.1103/PhysRevB.66.094408](https://doi.org/10.1103/PhysRevB.66.094408) (cited on pages 36, 37).
- [104] P. M. Raccach and J. B. Goodenough. 'First-Order Localized-Electron  $\rightleftharpoons$  Collective-Electron Transition in  $\text{LaCoO}_3$ '. In: *Phys. Rev.* 155 (3 Mar. 1967), pp. 932–943. doi: [10.1103/PhysRev.155.932](https://doi.org/10.1103/PhysRev.155.932) (cited on pages 36, 42).
- [105] G. Maris et al. 'Evidence for orbital ordering in  $\text{LaCoO}_3$ '. In: *Phys. Rev. B* 67 (22 June 2003), p. 224423. doi: [10.1103/PhysRevB.67.224423](https://doi.org/10.1103/PhysRevB.67.224423) (cited on pages 36, 37).
- [106] O Haas, R.P.W.J Struis, and J.M McBreen. 'Synchrotron X-ray absorption of  $\text{LaCoO}_3$  perovskite'. In: *Journal of Solid State Chemistry* 177.3 (2004), pp. 1000–1010. doi: <https://doi.org/10.1016/j.jssc.2003.10.004> (cited on pages 36, 45).
- [107] R. D. Shannon. 'Revised effective ionic radii and systematic studies of interatomic distances in halides and chalcogenides'. In: *Acta Crystallographica Section A* 32.5 (1976), pp. 751–767. doi: <https://doi.org/10.1107/S0567739476001551> (cited on page 36).

- [108] Han Hsu, Peter Blaha, and Renata M. Wentzcovitch. 'Ferromagnetic insulating state in tensile-strained LaCoO<sub>3</sub> thin films from LDA + *U* calculations'. In: *Phys. Rev. B* 85 (14 Apr. 2012), p. 140404. doi: [10.1103/PhysRevB.85.140404](https://doi.org/10.1103/PhysRevB.85.140404) (cited on page 36).
- [109] J. Buckeridge, F. H. Taylor, and C. R. A. Catlow. 'Efficient and accurate approach to modeling the microstructure and defect properties of LaCoO<sub>3</sub>'. In: *Phys. Rev. B* 93 (15 Apr. 2016), p. 155123. doi: [10.1103/PhysRevB.93.155123](https://doi.org/10.1103/PhysRevB.93.155123) (cited on pages 36, 42, 44).
- [110] A. Podlesnyak et al. 'Spin-State Transition in LaCoO<sub>3</sub>: Direct Neutron Spectroscopic Evidence of Excited Magnetic States'. In: *Phys. Rev. Lett.* 97 (24 Dec. 2006), p. 247208. doi: [10.1103/PhysRevLett.97.247208](https://doi.org/10.1103/PhysRevLett.97.247208) (cited on pages 37, 45).
- [111] G.H. Jonker and J.H. Van Santen. 'Magnetic compounds with perovskite structure III. ferromagnetic compounds of cobalt'. In: *Physica* 19.1 (1953), pp. 120–130. doi: [https://doi.org/10.1016/S0031-8914\(53\)80011-X](https://doi.org/10.1016/S0031-8914(53)80011-X) (cited on pages 37, 45).
- [112] T. Vogt et al. 'Pressure-induced intermediate-to-low spin state transition in LaCoO<sub>3</sub>'. In: *Phys. Rev. B* 67 (14 Apr. 2003), p. 140401. doi: [10.1103/PhysRevB.67.140401](https://doi.org/10.1103/PhysRevB.67.140401) (cited on pages 37, 80).
- [113] J. B. Torrance et al. 'Systematic study of insulator-metal transitions in perovskites RNiO<sub>3</sub> (R=Pr,Nd,Sm,Eu) due to closing of charge-transfer gap'. In: *Phys. Rev. B* 45 (14 Apr. 1992), pp. 8209–8212. doi: [10.1103/PhysRevB.45.8209](https://doi.org/10.1103/PhysRevB.45.8209) (cited on page 38).
- [114] J. L. García-Muñoz et al. 'Neutron-diffraction study of RNiO<sub>3</sub> (R=La,Pr,Nd,Sm): Electronically induced structural changes across the metal-insulator transition'. In: *Phys. Rev. B* 46 (8 Aug. 1992), pp. 4414–4425. doi: [10.1103/PhysRevB.46.4414](https://doi.org/10.1103/PhysRevB.46.4414) (cited on pages 38, 39).
- [115] Aaron Wold, Benjamin Post, and Ephraim Banks. 'Rare Earth Nickel Oxides'. In: *Journal of the American Chemical Society* 79.18 (Sept. 1957), pp. 4911–4913. doi: [10.1021/ja01575a022](https://doi.org/10.1021/ja01575a022) (cited on pages 38, 39).
- [116] Gérard Demazeau et al. 'Sur une série de composés oxygènes du nickel trivalent dérivés de la perovskite'. In: *Journal of Solid State Chemistry* 3.4 (1971), pp. 582–589. doi: [https://doi.org/10.1016/0022-4596\(71\)90105-8](https://doi.org/10.1016/0022-4596(71)90105-8) (cited on pages 38, 39, 46).
- [117] T. Mizokawa et al. 'Electronic structure of PrNiO<sub>3</sub> studied by photoemission and x-ray-absorption spectroscopy: Band gap and orbital ordering'. In: *Phys. Rev. B* 52 (19 Nov. 1995), pp. 13865–13873. doi: [10.1103/PhysRevB.52.13865](https://doi.org/10.1103/PhysRevB.52.13865) (cited on pages 38, 46).
- [118] Hanjie Guo et al. 'Antiferromagnetic correlations in the metallic strongly correlated transition metal oxide LaNiO<sub>3</sub>'. In: *Nature Communications* 9 (Jan. 2018). doi: [10.1038/s41467-017-02524-x](https://doi.org/10.1038/s41467-017-02524-x) (cited on pages 38, 46, 80).
- [119] J. B. Goodenough and P. M. Raccah. 'Complex vs Band Formation in Perovskite Oxides'. In: *Journal of Applied Physics* 36.3 (Mar. 1965), pp. 1031–1032. doi: [10.1063/1.1714087](https://doi.org/10.1063/1.1714087) (cited on pages 38, 42).
- [120] Gaoyang Gou et al. 'Lattice normal modes and electronic properties of the correlated metal LaNiO<sub>3</sub>'. In: *Phys. Rev. B* 84 (14 Oct. 2011), p. 144101. doi: [10.1103/PhysRevB.84.144101](https://doi.org/10.1103/PhysRevB.84.144101) (cited on pages 38, 56).
- [121] Yoshiro Nohara, Susumu Yamamoto, and Takeo Fujiwara. 'Electronic structure of perovskite-type transition metal oxides LaMO<sub>3</sub> (M = Ti ~ Cu) by U + GW approximation'. In: *Phys. Rev. B* 79 (19 May 2009), p. 195110. doi: [10.1103/PhysRevB.79.195110](https://doi.org/10.1103/PhysRevB.79.195110) (cited on page 38).
- [122] Christoph Baeumer et al. 'Tuning electrochemically driven surface transformation in atomically flat LaNiO<sub>3</sub> thin films for enhanced water electrolysis'. In: *Nature Materials* 20.5 (2021), pp. 674–682. doi: [10.1038/s41563-020-00877-1](https://doi.org/10.1038/s41563-020-00877-1) (cited on page 38).
- [123] P. Lacorre et al. 'Synthesis, crystal structure, and properties of metallic PrNiO<sub>3</sub>: Comparison with metallic NdNiO<sub>3</sub> and semiconducting SmNiO<sub>3</sub>'. In: *Journal of Solid State Chemistry* 91.2 (1991), pp. 225–237. doi: [https://doi.org/10.1016/0022-4596\(91\)90077-U](https://doi.org/10.1016/0022-4596(91)90077-U) (cited on page 39).
- [124] Jinwoo Hwang et al. 'Nanoscale quantification of octahedral tilts in perovskite films'. In: *Applied Physics Letters* 100.19 (May 2012). doi: [10.1063/1.4714734](https://doi.org/10.1063/1.4714734) (cited on page 39).
- [125] E. O. Wollan and W. C. Koehler. 'Neutron Diffraction Study of the Magnetic Properties of the Series of Perovskite-Type Compounds [(1 - x)La, xCa]MnO<sub>3</sub>'. In: *Phys. Rev.* 100 (2 Oct. 1955), pp. 545–563. doi: [10.1103/PhysRev.100.545](https://doi.org/10.1103/PhysRev.100.545) (cited on page 40).

- [126] Xiwei Qi et al. 'Auto-combustion synthesis of nanocrystalline LaFeO<sub>3</sub>'. In: *Materials Chemistry and Physics - MATER CHEM PHYS* 78 (Feb. 2002), pp. 25–29. doi: [10.1016/S0254-0584\(02\)00341-3](https://doi.org/10.1016/S0254-0584(02)00341-3) (cited on page 40).
- [127] Roberto Köferstein, Lothar Jäger, and Stefan G. Ebbinghaus. 'Magnetic and optical investigations on LaFeO<sub>3</sub> powders with different particle sizes and corresponding ceramics'. In: *Solid State Ionics* 249-250 (2013), pp. 1–5. doi: <https://doi.org/10.1016/j.ssi.2013.07.001> (cited on pages 40, 49).
- [128] G.H. Jonker. 'Magnetic compounds with perovskite structure IV Conducting and non-conducting compounds'. In: *Physica* 22.6 (1956), pp. 707–722. doi: [https://doi.org/10.1016/S0031-8914\(56\)90023-4](https://doi.org/10.1016/S0031-8914(56)90023-4) (cited on page 40).
- [129] René Benoit. 'Étude paramagnétique des ferrites de terres rares.' In: *Comptes rendus hebdomadaires des séances de l'Académie des sciences* 240.2 (Apr. 1955), pp. 2389–2390 (cited on page 40).
- [130] Martin Etter et al. 'High-pressure phase transitions in the rare-earth orthoferrite LaFeO<sub>3</sub>'. In: *Structural Science* 70.3 (2014), pp. 452–458 (cited on page 40).
- [131] Mara Capone et al. 'Subtle Structural Changes in LaFeO<sub>3</sub> at High Pressure'. In: *physica status solidi (b)* 258.2 (2021), p. 2000413. doi: <https://doi.org/10.1002/pssb.202000413> (cited on page 40).
- [132] John B. Goodenough. 'An interpretation of the magnetic properties of the perovskite-type mixed crystals La<sub>1-x</sub>Sr<sub>x</sub>CoO<sub>3-δ</sub>'. In: *Journal of Physics and Chemistry of Solids* 6.2 (1958), pp. 287–297. doi: [https://doi.org/10.1016/0022-3697\(58\)90107-0](https://doi.org/10.1016/0022-3697(58)90107-0) (cited on page 42).
- [133] M. A. Señarís-Rodríguez and J. B. Goodenough. 'LaCoO<sub>3</sub> Revisited'. In: *Journal of Solid State Chemistry* 116.2 (1995), pp. 224–231. doi: <https://doi.org/10.1006/jssc.1995.1207> (cited on page 42).
- [134] Tetsurō Nakamura, G. Petzow, and L.J. Gauckler. 'Stability of the perovskite phase LaBO<sub>3</sub> (B = V, Cr, Mn, Fe, Co, Ni) in reducing atmosphere I. Experimental results'. In: *Materials Research Bulletin* 14.5 (1979), pp. 649–659. doi: [https://doi.org/10.1016/0025-5408\(79\)90048-5](https://doi.org/10.1016/0025-5408(79)90048-5) (cited on page 42).
- [135] N. Menyuk, K. Dwight, and P.M. Raccah. 'Low temperature crystallographic and magnetic study of LaCoO<sub>3</sub>'. In: *Journal of Physics and Chemistry of Solids* 28.4 (1967), pp. 549–556. doi: [https://doi.org/10.1016/0022-3697\(67\)90085-6](https://doi.org/10.1016/0022-3697(67)90085-6) (cited on page 42).
- [136] Yukito Tanabe and Satoru Sugano. 'On the Absorption Spectra of Complex Ions. I'. In: *Journal of the Physical Society of Japan* 9.5 (1954), pp. 753–766. doi: [10.1143/JPSJ.9.753](https://doi.org/10.1143/JPSJ.9.753) (cited on page 42).
- [137] C. S. Naiman et al. 'Interpretation of the Magnetic Properties of LaCoO<sub>3</sub>'. In: *Journal of Applied Physics* 36.3 (Mar. 1965), pp. 1044–1045. doi: [10.1063/1.1714092](https://doi.org/10.1063/1.1714092) (cited on page 42).
- [138] M. W. Haverkort et al. 'Spin State Transition in LaCoO<sub>3</sub> Studied Using Soft X-ray Absorption Spectroscopy and Magnetic Circular Dichroism'. In: *Phys. Rev. Lett.* 97 (17 Oct. 2006), p. 176405. doi: [10.1103/PhysRevLett.97.176405](https://doi.org/10.1103/PhysRevLett.97.176405) (cited on pages 42, 45).
- [139] G. Blasse. 'Magnetic Properties of Mixed Metal Oxides Containing Trivalent Cobalt'. In: *Journal of Applied Physics* 36.3 (Mar. 1965), pp. 879–883. doi: [10.1063/1.1714256](https://doi.org/10.1063/1.1714256) (cited on page 42).
- [140] D. Fuchs et al. 'Ferromagnetic order in epitaxially strained LaCoO<sub>3</sub> thin films'. In: *Phys. Rev. B* 75 (14 Apr. 2007), p. 144402. doi: [10.1103/PhysRevB.75.144402](https://doi.org/10.1103/PhysRevB.75.144402) (cited on page 42).
- [141] A. D. Rata et al. 'Lattice structure and magnetization of LaCoO<sub>3</sub> thin films'. In: *The European Physical Journal B* 76.2 (June 2010), pp. 215–219. doi: [10.1140/epjb/e2010-00203-6](https://doi.org/10.1140/epjb/e2010-00203-6) (cited on pages 42, 73).
- [142] Dechao Meng et al. 'Strain-induced high-temperature perovskite ferromagnetic insulator'. In: *Proceedings of the National Academy of Sciences* 115.12 (2018), pp. 2873–2877. doi: [10.1073/pnas.1707817115](https://doi.org/10.1073/pnas.1707817115) (cited on pages 42, 73).
- [143] A. Rambabu and A. Sundaresan. 'Magnetic and electrical properties of LaCoO<sub>3</sub> - LaNiO<sub>3</sub> epitaxial thin films on LaAlO<sub>3</sub> substrate'. In: *Materials Today: Proceedings* (Mar. 2023). doi: [10.1016/j.matpr.2023.02.275](https://doi.org/10.1016/j.matpr.2023.02.275) (cited on pages 42, 73).
- [144] Neven Biškup et al. 'Insulating Ferromagnetic LaCoO<sub>3-δ</sub> Films: A Phase Induced by Ordering of Oxygen Vacancies'. In: *Phys. Rev. Lett.* 112 (8 Feb. 2014), p. 087202. doi: [10.1103/PhysRevLett.112.087202](https://doi.org/10.1103/PhysRevLett.112.087202) (cited on page 42).

- [145] T. Saitoh et al. 'Electronic structure and temperature-induced paramagnetism in LaCoO<sub>3</sub>'. In: *Phys. Rev. B* 55 (7 Feb. 1997), pp. 4257–4266. doi: [10.1103/PhysRevB.55.4257](https://doi.org/10.1103/PhysRevB.55.4257) (cited on pages 42, 52).
- [146] M. Abbate et al. 'Band-structure and cluster-model calculations of LaCoO<sub>3</sub> in the low-spin phase'. In: *Phys. Rev. B* 49 (11 Mar. 1994), pp. 7210–7218. doi: [10.1103/PhysRevB.49.7210](https://doi.org/10.1103/PhysRevB.49.7210) (cited on page 42).
- [147] Ru-Pan Wang et al. 'Low-energy orbital excitations in strained LaCoO<sub>3</sub> films'. In: *Phys. Rev. B* 100 (16 Oct. 2019), p. 165148. doi: [10.1103/PhysRevB.100.165148](https://doi.org/10.1103/PhysRevB.100.165148) (cited on pages 44, 73).
- [148] M. Abbate et al. 'Electronic structure and spin-state transition of LaCoO<sub>3</sub>'. In: *Phys. Rev. B* 47 (24 June 1993), pp. 16124–16130. doi: [10.1103/PhysRevB.47.16124](https://doi.org/10.1103/PhysRevB.47.16124) (cited on pages 45, 51).
- [149] Despina Louca et al. 'Correlation of local Jahn-Teller distortions to the magnetic/conductive states of La<sub>1-x</sub>Sr<sub>x</sub>CoO<sub>3</sub>'. In: *Phys. Rev. B* 60 (14 Oct. 1999), pp. 10378–10382. doi: [10.1103/PhysRevB.60.10378](https://doi.org/10.1103/PhysRevB.60.10378) (cited on page 45).
- [150] V. K řápek et al. 'Spin state transition and covalent bonding in LaCoO<sub>3</sub>'. In: *Phys. Rev. B* 86 (19 Nov. 2012), p. 195104. doi: [10.1103/PhysRevB.86.195104](https://doi.org/10.1103/PhysRevB.86.195104) (cited on page 45).
- [151] M. Medarde et al. 'Low-temperature spin-state transition in LaCoO<sub>3</sub> investigated using resonant x-ray absorption at the Co K edge'. In: *Phys. Rev. B* 73 (5 Feb. 2006), p. 054424. doi: [10.1103/PhysRevB.73.054424](https://doi.org/10.1103/PhysRevB.73.054424) (cited on page 45).
- [152] Y. Kobayashi et al. 'Inelastic neutron scattering study of phonons and magnetic excitations in LaCoO<sub>3</sub>'. In: *Phys. Rev. B* 72 (17 Nov. 2005), p. 174405. doi: [10.1103/PhysRevB.72.174405](https://doi.org/10.1103/PhysRevB.72.174405) (cited on page 45).
- [153] R. F. Klie et al. 'Direct Measurement of the Low-Temperature Spin-State Transition in LaCoO<sub>3</sub>'. In: *Phys. Rev. Lett.* 99 (4 July 2007), p. 047203. doi: [10.1103/PhysRevLett.99.047203](https://doi.org/10.1103/PhysRevLett.99.047203) (cited on page 45).
- [154] M. Abbate et al. 'Electronic structure and metal-insulator transition in LaNiO<sub>3-δ</sub>'. In: *Phys. Rev. B* 65 (15 Mar. 2002), p. 155101. doi: [10.1103/PhysRevB.65.155101](https://doi.org/10.1103/PhysRevB.65.155101) (cited on page 46).
- [155] S. Mickevičius et al. 'Investigation of epitaxial LaNiO<sub>3-x</sub> thin films by high-energy XPS'. In: *Journal of Alloys and Compounds* 423.1-2 (2006), pp. 107–111. doi: [10.1016/j.jallcom.2005.12.038](https://doi.org/10.1016/j.jallcom.2005.12.038) (cited on page 46).
- [156] M. Medarde et al. 'RNiO<sub>3</sub> perovskites (R=Pr,Nd): Nickel valence and the metal-insulator transition investigated by x-ray-absorption spectroscopy'. In: *Phys. Rev. B* 46 (23 Dec. 1992), pp. 14975–14984. doi: [10.1103/PhysRevB.46.14975](https://doi.org/10.1103/PhysRevB.46.14975) (cited on page 46).
- [157] D. P. Chong, O. V. Gritsenko, and E. J. Baerends. 'Interpretation of the Kohn-Sham orbital energies as approximate vertical ionization potentials'. In: *The Journal of Chemical Physics* 116.5 (Feb. 2002), pp. 1760–1772. doi: [10.1063/1.1430255](https://doi.org/10.1063/1.1430255) (cited on page 48).
- [158] T. Körzdörfer et al. 'When to trust photoelectron spectra from Kohn-Sham eigenvalues: The case of organic semiconductors'. In: *Phys. Rev. B* 79 (20 May 2009), p. 201205. doi: [10.1103/PhysRevB.79.201205](https://doi.org/10.1103/PhysRevB.79.201205) (cited on page 48).
- [159] Thomas Christoph Koethe. 'Bulk sensitive Photoelectron Spectroscopy of strongly correlated transition metal oxides'. PhD thesis. Universität zu Köln, 2006 (cited on pages 48, 52, 53).
- [160] C.-O. Almbladh and U. von Barth. 'Exact results for the charge and spin densities, exchange-correlation potentials, and density-functional eigenvalues'. In: *Phys. Rev. B* 31 (6 Mar. 1985), pp. 3231–3244. doi: [10.1103/PhysRevB.31.3231](https://doi.org/10.1103/PhysRevB.31.3231) (cited on page 48).
- [161] T Koopmans. 'Über die Zuordnung von Wellenfunktionen und Eigenwerten zu den Einzelnen Elektronen Eines Atoms'. In: *Physica* 1.1 (1934), pp. 104–113. doi: [https://doi.org/10.1016/S0031-8914\(34\)90011-2](https://doi.org/10.1016/S0031-8914(34)90011-2) (cited on page 48).
- [162] T. Körzdörfer and S. Kümmel. 'Single-particle and quasiparticle interpretation of Kohn-Sham and generalized Kohn-Sham eigenvalues for hybrid functionals'. In: *Phys. Rev. B* 82 (15 Oct. 2010), p. 155206. doi: [10.1103/PhysRevB.82.155206](https://doi.org/10.1103/PhysRevB.82.155206) (cited on page 48).
- [163] T. Arima, Y. Tokura, and J. B. Torrance. 'Variation of optical gaps in perovskite-type 3d transition-metal oxides'. In: *Phys. Rev. B* 48 (23 Dec. 1993), pp. 17006–17009. doi: [10.1103/PhysRevB.48.17006](https://doi.org/10.1103/PhysRevB.48.17006) (cited on pages 49, 51).



- [164] Mark D Scafetta et al. 'Band structure and optical transitions in LaFeO<sub>3</sub>: theory and experiment'. In: *Journal of Physics: Condensed Matter* 26.50 (Nov. 2014), p. 505502. doi: [10.1088/0953-8984/26/50/505502](https://doi.org/10.1088/0953-8984/26/50/505502) (cited on page 49).
- [165] H. Wadati et al. 'Hole-doping-induced changes in the electronic structure of La<sub>1-x</sub>Sr<sub>x</sub>FeO<sub>3</sub>: Soft x-ray photoemission and absorption study of epitaxial thin films'. In: *Phys. Rev. B* 71 (3 Jan. 2005), p. 035108. doi: [10.1103/PhysRevB.71.035108](https://doi.org/10.1103/PhysRevB.71.035108) (cited on pages 49, 50).
- [166] Sergey Y. Smolin et al. 'Energy Level Alignment and Cation Charge States at the LaFeO<sub>3</sub>/LaMnO<sub>3</sub> (001) Heterointerface'. In: *Advanced Materials Interfaces* 4.14 (2017), p. 1700183. doi: <https://doi.org/10.1002/admi.201700183> (cited on pages 49, 50).
- [167] A. Chainani, M. Mathew, and D. D. Sarma. 'Electron-spectroscopy study of the semiconductor-metal transition in La<sub>1-x</sub>Sr<sub>x</sub>CoO<sub>3</sub>'. In: *Phys. Rev. B* 46 (16 Oct. 1992), pp. 9976–9983. doi: [10.1103/PhysRevB.46.9976](https://doi.org/10.1103/PhysRevB.46.9976) (cited on page 51).
- [168] L. Richter, S. D. Bader, and M. B. Brodsky. 'Ultraviolet, x-ray-photoelectron, and electron-energy-loss spectroscopy studies of LaCoO<sub>3</sub> and oxygen chemisorbed on LaCoO<sub>3</sub>'. In: *Phys. Rev. B* 22 (6 Sept. 1980), pp. 3059–3064. doi: [10.1103/PhysRevB.22.3059](https://doi.org/10.1103/PhysRevB.22.3059) (cited on page 52).
- [169] Xiaotian Wang et al. 'R $\bar{3}c$  type LnNiO<sub>3</sub> (Ln = La, Ce, Nd, Pm, Gd, Tb, Dy, Ho, Er, Lu) half-metals with multiple Dirac cones: a potential class of advanced spintronic materials'. In: *IUCrJ* 6.6 (Nov. 2019), pp. 990–995. doi: [10.1107/S2052252519012570](https://doi.org/10.1107/S2052252519012570) (cited on page 55).
- [170] E. J. Moon et al. 'Strain-controlled band engineering and self-doping in ultrathin LaNiO<sub>3</sub> films'. In: *Phys. Rev. B* 85 (12 Mar. 2012), p. 121106. doi: [10.1103/PhysRevB.85.121106](https://doi.org/10.1103/PhysRevB.85.121106) (cited on page 55).
- [171] S. R. Barman, A. Chainani, and D. D. Sarma. 'Covalency-driven unusual metal-insulator transition in nickelates'. In: *Phys. Rev. B* 49 (12 Mar. 1994), pp. 8475–8478. doi: [10.1103/PhysRevB.49.8475](https://doi.org/10.1103/PhysRevB.49.8475) (cited on pages 55, 57).
- [172] J.P. Kemp and P.A. Cox. 'LaNiO<sub>3</sub>: A study by electron spectroscopy'. In: *Solid State Communications* 75.9 (1990), pp. 731–735. doi: [https://doi.org/10.1016/0038-1098\(90\)90236-5](https://doi.org/10.1016/0038-1098(90)90236-5) (cited on page 55).
- [173] K. Horiba et al. 'Electronic structure of LaNiO<sub>3-x</sub>: An in situ soft x-ray photoemission and absorption study'. In: *Phys. Rev. B* 76 (15 Oct. 2007), p. 155104. doi: [10.1103/PhysRevB.76.155104](https://doi.org/10.1103/PhysRevB.76.155104) (cited on pages 55, 56).
- [174] E. Alves et al. 'Band structure and cluster model calculations of LaNiO<sub>3</sub> compared to photoemission, O 1s X-ray absorption, and optical absorption spectra'. In: *Physics Letters A* 383.24 (2019), pp. 2952–2956. doi: <https://doi.org/10.1016/j.physleta.2019.06.012> (cited on page 56).
- [175] E. B. Saloman, J. H. Hubbell, and J. H. Scofield. 'X-ray attenuation cross sections for energies 100 eV to 100 keV and elements Z = 1 to Z = 92'. In: *Atom. Data Nucl. Data Tabl.* 38 (1988), pp. 1–196. doi: [10.1016/0092-640X\(88\)90044-7](https://doi.org/10.1016/0092-640X(88)90044-7) (cited on page 56).
- [176] Ellen M. Kiens et al. 'Deeper mechanistic insights into epitaxial nickelate electrocatalysts for the oxygen evolution reaction'. In: *Chem. Commun.* 59 (31 2023), pp. 4562–4577. doi: [10.1039/D3CC00325F](https://doi.org/10.1039/D3CC00325F) (cited on page 71).
- [177] Y. Du et al. 'Optical properties of SrTiO<sub>3</sub> thin films by pulsed laser deposition'. In: *Applied Physics A* 76.7 (2003), pp. 1105–1108. doi: [10.1007/s00339-002-1998-z](https://doi.org/10.1007/s00339-002-1998-z) (cited on page 72).
- [178] James M. Rondinelli and Nicola A. Spaldin. 'Structure and Properties of Functional Oxide Thin Films: Insights From Electronic-Structure Calculations'. In: *Advanced Materials* 23.30 (2011), pp. 3363–3381. doi: <https://doi.org/10.1002/adma.201101152> (cited on page 72).
- [179] Patrick M. McBride et al. 'Effects of biaxial stress and layer thickness on octahedral tilts in LaNiO<sub>3</sub>'. In: *Applied Physics Letters* 107.26 (Dec. 2015), p. 261901. doi: [10.1063/1.4939002](https://doi.org/10.1063/1.4939002) (cited on page 72).
- [180] Jennifer Fowlie et al. 'Thickness-Dependent Perovskite Octahedral Distortions at Heterointerfaces'. In: *Nano Letters* 19.6 (2019). PMID: 31117765, pp. 4188–4194. doi: [10.1021/acs.nanolett.9b01772](https://doi.org/10.1021/acs.nanolett.9b01772) (cited on page 72).

- [181] J W Seo et al. 'Antiferromagnetic LaFeO<sub>3</sub> thin films and their effect on exchange bias'. In: *Journal of Physics: Condensed Matter* 20.26 (2008), p. 264014. doi: [10.1088/0953-8984/20/26/264014](https://doi.org/10.1088/0953-8984/20/26/264014) (cited on pages 73, 78).
- [182] I. S. Lyubutin, T. V. Dmitrieva, and A. S. Stepin. 'Dependence of exchange interactions on chemical bond angle in a structural series: Cubic perovskite-rhombic orthoferrite-rhombohedral hematite'. In: *Journal of Experimental and Theoretical Physics* 88.3 (1999), pp. 590–597. doi: [10.1134/1.558833](https://doi.org/10.1134/1.558833) (cited on page 73).
- [183] Menglin Zhu et al. *Emergent Ferromagnetism at LaFeO<sub>3</sub>/SrTiO<sub>3</sub> Interface Arising from Strain-induced Spin-State Transition*. 2024. URL: <https://arxiv.org/abs/2405.12950> (cited on page 73).
- [184] Rajendra Paudel et al. 'Band-engineered LaFeO<sub>3</sub>–LaNiO<sub>3</sub> thin film interfaces for electrocatalysis of water'. In: *Journal of Vacuum Science & Technology A* 41.6 (Oct. 2023), p. 063207. doi: [10.1116/6.0002987](https://doi.org/10.1116/6.0002987) (cited on page 73).
- [185] A. Posadas et al. 'Epitaxial integration of ferromagnetic correlated oxide LaCoO<sub>3</sub> with Si (100)'. In: *Applied Physics Letters* 98.5 (Feb. 2011), p. 053104. doi: [10.1063/1.3549301](https://doi.org/10.1063/1.3549301) (cited on page 73).
- [186] G. E. Sterbinsky et al. 'Local atomic and electronic structures of epitaxial strained LaCoO<sub>3</sub> thin films'. In: *Phys. Rev. B* 85 (2 Jan. 2012), p. 020403. doi: [10.1103/PhysRevB.85.020403](https://doi.org/10.1103/PhysRevB.85.020403) (cited on pages 73, 79).
- [187] D. Fuchs et al. 'Tuning the magnetic properties of LaCoO<sub>3</sub> thin films by epitaxial strain'. In: *Phys. Rev. B* 77 (1 Jan. 2008), p. 014434. doi: [10.1103/PhysRevB.77.014434](https://doi.org/10.1103/PhysRevB.77.014434) (cited on pages 73, 79).
- [188] A M Durand et al. 'The effects of Co<sub>3</sub>O<sub>4</sub> on the structure and unusual magnetism of LaCoO<sub>3</sub>'. In: *Journal of Physics: Condensed Matter* 27.12 (Mar. 2015), p. 126001. doi: [10.1088/0953-8984/27/12/126001](https://doi.org/10.1088/0953-8984/27/12/126001) (cited on page 73).
- [189] Vincenzo Fiorentini and M Methfessel. 'Extracting convergent surface energies from slab calculations'. In: *Journal of Physics: Condensed Matter* 8.36 (1996), p. 6525. doi: [10.1088/0953-8984/8/36/005](https://doi.org/10.1088/0953-8984/8/36/005) (cited on page 74).
- [190] Y. Tokura et al. 'Thermally induced insulator-metal transition in LaCoO<sub>3</sub>: A view based on the Mott transition'. In: *Phys. Rev. B* 58 (4 July 1998), R1699–R1702. doi: [10.1103/PhysRevB.58.R1699](https://doi.org/10.1103/PhysRevB.58.R1699) (cited on page 80).
- [191] György Vankó Jean-Pascal Rueff Aleksi Mattila Zoltán Németh and Abhay Shukla. 'Temperature- and pressure-induced spin-state transitions in LaCoO<sub>3</sub>'. In: *Phys. Rev. B* 73 (2 Jan. 2006), p. 024424. doi: [10.1103/PhysRevB.73.024424](https://doi.org/10.1103/PhysRevB.73.024424) (cited on page 80).
- [192] Changjiang Liu et al. 'Observation of an antiferromagnetic quantum critical point in high-purity LaNiO<sub>3</sub>'. In: *Nature Communications* 11.1 (2020), p. 1402. doi: [10.1038/s41467-020-15143-w](https://doi.org/10.1038/s41467-020-15143-w) (cited on page 80).
- [193] M. Nakamura et al. 'Spontaneous Polarization and Bulk Photovoltaic Effect Driven by Polar Discontinuity in LaFeO<sub>3</sub>/SrTiO<sub>3</sub> Heterojunctions'. In: *Phys. Rev. Lett.* 116 (15 Apr. 2016), p. 156801. doi: [10.1103/PhysRevLett.116.156801](https://doi.org/10.1103/PhysRevLett.116.156801) (cited on page 85).
- [194] Anubhav Jain et al. 'Commentary: The Materials Project: A materials genome approach to accelerating materials innovation'. In: *APL Materials* 1.1 (July 2013), p. 011002. doi: [10.1063/1.4812323](https://doi.org/10.1063/1.4812323) (cited on pages 91, 93).
- [195] Alex M. Ganose, Adam J. Jackson, and David O. Scanlon. 'sumo: Command-line tools for plotting and analysis of periodic \*ab initio\* calculations'. In: *Journal of Open Source Software* 3.28 (2018), p. 717. doi: [10.21105/joss.00717](https://doi.org/10.21105/joss.00717) (cited on page 92).
- [196] Wenhao Sun and Gerbrand Ceder. 'Efficient creation and convergence of surface slabs'. In: *Surface Science* 617 (2013), pp. 53–59. doi: <https://doi.org/10.1016/j.susc.2013.05.016> (cited on page 100).
- [197] Š. Masys and V. Jonauskas. 'Elastic properties of rhombohedral, cubic, and monoclinic phases of LaNiO<sub>3</sub> by first principles calculations'. In: *Computational Materials Science* 108 (2015), pp. 153–159. doi: <https://doi.org/10.1016/j.commatsci.2015.06.034> (cited on page 100).

- [198] Céline Lichtensteiger. 'InteractiveXRDFit: a new tool to simulate and fit X-ray diffractograms of oxide thin films and heterostructures'. In: *Journal of Applied Crystallography* 51.6 (Dec. 2018), 1745 to 1751. doi: [10.1107/S1600576718012840](https://doi.org/10.1107/S1600576718012840) (cited on page 101).
- [199] P. J. Brown et al. 'Intensity of diffracted intensities'. In: *International Tables for Crystallography, Online MRW*. John Wiley & Sons, Ltd, 2006. Chap. 6.1, pp. 554–595. doi: <https://doi.org/10.1107/97809553602060000600> (cited on page 101).
- [200] Park Systems Corp. *Amplitude Modulation Kelvin Probe Force Microscopy (AM-KPFM)*. May 2024 (cited on page 105).